Constitutively active RAS in *S. pombe* causes persistent Cdc42 signalling but only transient MAPK activation

Emma J. Kelsall[1,7], Ábel Vértesy[2,7], Kees Straatman[3], Mishal Tariq[1], Raquel Gadea[1,4], Chandni Parmar[1], Gabriele Schreiber[2], Shubhchintan Randhawa[1,6], Cyril Dominguez[1,5], Edda Klipp[2]* and Kayoko Tanaka[1]*

1 Department of Molecular and Cell Biology, University of Leicester

2 Theoretical Biophysics, Institute of Biology, Humboldt-Universität zu Berlin

3 Centre for Core Biotechnology Services, University of Leicester

4 Marco Formacion Profesional, Calle del Conde de Aranda 7-9, 50004 Zaragoza, Spain

5 Leicester Institute of Structural and Chemical Biology, University of Leicester

6 Present address: Sanjay Gandhi Post Graduate Institute of Medical Sciences, Department of Molecular Medicine & Biotechnology, Lucknow, India 226014

7 These authors contributed equally

*Correspondence: kt96@le.ac.uk (K.T.), edda.klipp@rz.hu-berlin.de (E.K.)

Highlights

(1) Constitutively active Ras1.GV prolongs Cdc42 activation in *S. pombe* pheromone signalling

(2) Ras1.GV results in an immediate but only transient $MAPK^{Spk1}$ activation

(3) The RAS effector pathways $MAPK^{Spk1}$ and Cdc42 compete with each other for active Ras1

(4) Predictive modelling explains $MAPK^{Spk1}$ activation dynamics in 24 signaling-mutants

eTOC Blurb

S. pombe Ras1 activates the $MAPK^{Spk1}$ and Cdc42 pathways. Kelsall et al. report that the constitutively active Ras1.G17V mutation, which causes morphological anomalies, induces prolonged Cdc42 activation but only a transient $MAPK^{Spk1}$ activation followed by attenuation. Mathematical modelling and biochemical data suggest a competition between the $MAPK^{Spk1}$ and Cdc42 pathways for active Ras1.

Summary

The small GTPase RAS is a signalling hub for many pathways and oncogenic human RAS mutations are assumed to over-activate all of its downstream pathways. We tested this assumption in fission yeast, where, RAS-mediated pheromone signalling (PS) activates the $MAPK^{Spk1}$ and Cdc42 pathways. Unexpectedly, we found that constitutively active Ras1.G17V induced immediate but only transient $MAPK^{Spk1}$ activation, whilst Cdc42 activation persisted. Immediate but transient $MAPK^{Spk1}$ activation was also seen in the deletion mutant of Cdc42-GEF^{Scd1}, a Cdc42 activator. We built a mathematical model using PS negative-feedback circuits and competition between the two Ras1 effectors, $MAPKKK^{Byr2}$ and Cdc42-GEF^{Scd1}. The model robustly predicted the $MAPK^{Spk1}$ activation dynamics of an additional 21 PS mutants. Supporting the model, we showed that a recombinant Cdc42-GEF^{Scd1} fragment competes with $MAPKKK^{Byr2}$ for Ras1 binding. Our study has established a concept that the constitutively active RAS propagates differently to downstream pathways where the system prevents MAPK overactivation.

Key words

Ras, MAPK, Cdc42/Rac, yeast pheromone signalling

Introduction

Proto-oncogene Ras GTPase family members are widely conserved and play pivotal roles in cell growth, differentiation and apoptosis (Cox and Der, 2010). The physiological impact of Ras mutations is highlighted in the resultant tumorigenesis and developmental disorders (Prior et al., 2012; Schubbert et al., 2007). More than 99% of identified oncogenic RAS mutations occur at codons 12, 13 and 61 of human Ras isoforms (Prior et al., 2012) and impair efficient GTP hydrolysis (Trahey and McCormick, 1987). This results in accumulation of GTP-bound Ras, which is generally considered to cause constitutive activation of the downstream effector pathways, such as ERK and PI3K signalling pathways (Lin et al., 1998; Zhu et al., 1998). Interestingly, however, mouse embryonic fibroblasts (MEFs) derived from the *K-ras*^{G12D} mouse model show neither an increased basal level of active ERK and Akt nor constitutive activation of ERK and Akt upon growth factor stimulation even though the *K-ras*^{G12D} MEFs showed enhanced proliferation and partial transformation (Tuveson et al., 2004). This observation indicates that not all effector pathways become constitutively activated by oncogenic Ras, presumably because of an efficient negative feedback loop. Meanwhile, it is reasonable to expect that oncogenic RAS over-activates some of its effector pathways to initiate tumorigenesis. Small GTPases, including Cdc42 and Rac, may be such effector pathways, as they are required in oncogenic-RAS-driven tumorigenesis (Malliri et al., 2002; Qiu et al., 1997; Stengel and Zheng, 2012).

We wished to understand how multiple Ras effector pathways respond to the Ras-triggered signals in a physiological setting. We employed the model organism fission yeast. In this organism, a unique Ras homologue, Ras1, plays a key role in pheromone signalling to cause mating of haploid cells and sporulation in diploid cells (Yamamoto, 1996)(Fig. 1A, B). Upon nutritional starvation, cells of opposite mating types (h^+ and h^-) exchange mating pheromones. Gpa1, the α-subunit of the pheromone receptor-coupled G-protein, relays the pheromone signal into the cell (Obara et al., 1991). Activated Gpa1 together with Ras1 then activate MAPK cascade consisting of Byr2 (MAPKKK), Byr1 (MAPKK) and Spk1 (MAPK) (Fukui et al., 1986; Masuda et al., 1995; Nadin-Davis and Nasim, 1988; Nadin-Davis et al., 1986a; Nadin-Davis et al., 1986b; Wang et al., 1991; Xu et al., 1994). An intriguing observation is that the *ras1.G17V* mutant, an equivalent of mammalian *ras.G12V* mutant prevalent in cancer, produces an excessively elongated shmoo, or a conjugation tube, upon exposure to the mating pheromone (Nadin-Davis et al., 1986a). This “elongated” *ras1.G17V* phenotype has been interpretted that Ras1 may be responsible for amplifying the pheromone signal (Yamamoto, 1996).

83 Ras1 also regulates cell morphology during vegetative growth; whilst deletion of either *gpa1*,
84 *MAPKKK*^{byr2}, *MAPKK*^{byr1} or *MAPK*^{spk1} does not result in any obvious phenotypes during vegetative
85 cell growth (Obara et al., 1991; Sipiczki, 1988; Toda et al., 1991), *ras1Δ* cells lose the typical rod-
86 shape morphology of fission yeast to become rounded (Fukui et al., 1989; Nadin-Davis et al.,
87 1986a). Studies based on recombinant protein assays and yeast-2-hybrid analysis demonstrated
88 that Ras1 interacts with both MAPKKK^{Byr2} and Scd1, a GDP-GTP exchange factor (GEF) for Cdc42,
89 which regulates the actin cytoskeleton and cell morphology (Chang et al., 1994; Gronwald et al.,
90 2001; Tu et al., 1997). These observations suggest that Ras1 simultaneously regulates both the
91 pheromone MAPK^{Spk1} and the Cdc42 pathways at the cell membrane (Weston et al., 2013).
92 Indeed, a dynamic "Cdc42 zone" at the cell cortex prior to mating has been observed (Merlini et
93 al., 2013) and Ras1 and MAPK^{Spk1} cascade components are found there and are involved in the
94 process (Dudin et al., 2016; Merlini et al., 2013; Merlini et al., 2016; Merlini et al., 2018; Weston
95 et al., 2013). However, it is not yet understood how Ras1 interplay between the two pathways.
96 By establishing conditions to induce highly synchronous mating of fission yeast cells, for the first
97 time we were able to follow MAPK^{Spk1} activation dynamics during the physiological mating
98 process in wildtype and in mutants showing various mating phenotypes. This comprehensive set
99 of quantitative measurements allowed us to build a mathematical model of the Ras-mediated
100 pheromone signalling. Our model serves as a prototype of a branched Ras-mediated signalling
101 pathway, demonstrating a competition of downstream pathways for a common upstream
102 activator, Ras1. The model also highlights the physiological importance of the bipartite
103 activation of MAPKKK^{Byr2}: a Ras1-dependent and a Ras1-independent mechanism, the latter of
104 which employs the adaptor protein Ste4 (Barr et al., 1996; Okazaki et al., 1991). The adaptor^{Ste4}
105 can be targeted to downregulate MAPK^{Spk1} even in the presence of *ras1.G17V* mutation. Finally,
106 our study reveals the crucial role played by Cdc42 in the *ras1.G17V* mutant causing the
107 *ras1.G17V* phenotype.
108

Results

(1) A highly synchronous mating assay allows the precise measurement of MAPK^{Spk1} activity

To directly measure fission yeast pheromone signalling, we quantitated MAPK^{Spk1} phosphorylation throughout the mating process (Supplementary Fig. S1, Fig. 1A and B). We established a protocol to induce highly synchronous mating and employed cells where the endogenous MAPK^{Spk1} is tagged with GFP-2xFLAG. Under these conditions, homothallic *h^{90}* cells started to mate 7-hours after induction of mating (Fig. 1C, grey line). Phosphorylated (active) MAPK^{Spk1} (**pp**MAPK^{Spk1}) levels were quantitated as described in Materials and Methods. The **pp**MAPK^{Spk1} signal was first detected three hours after induction of mating and reached its peak at about seven hours, when cell fusion was also initially observed (Fig. 1C, blue line. Original membrane images presented in Supplementary Fig. S3). The **pp**MAPK^{Spk1} then gradually decreased to a non-zero level as meiosis continued towards sporulation. The observation established that the MAPK^{Spk1}-GFP activation occurs as the mating process progresses and declines before sporulation, around 15 hours post induction. It was also noted that the total MAPK^{Spk1}-GFP was essentially not expressed during the vegetative cycle, but it was promptly induced by nitrogen starvation (Supplementary Fig. S2A and S2B). The *mapk^{spk1}* gene is a known target of the transcription factor Ste11 (Mata and Bahler, 2006), which itself is activated (phosphorylated) by MAPK^{Spk1} (Kjaerulff et al., 2005). This positive feedback loop likely facilitates a swift increase of MAPK^{Spk1} expression upon nitrogen starvation.

We found that MAPK^{Spk1}-GFP localised to both the cytosol and the nucleus, with some nuclear accumulation, before it gradually disappeared as the mating process came to the end (Fig. 1D). Interestingly, transient foci of GFP signals were also found at the cell cortex, as has been reported for MAPKK^{Byr1}, the activator of MAPK^{Spk1} (Dudin et al., 2016) (Fig. 1D, yellow arrows).

(2) Constitutively active MAPKK$^{Byr1.DD}$ mutant causes constitutive activation of MAPK^{Spk1}

Activation of MAPKK family kinases is mediated by dual phosphorylation of conserved Ser/Thr residues (Zheng and Guan, 1994). These correspond to serine 214 and threonine 218 of the MAPKK^{Byr1}. A MAPKK^{Byr1} mutant termed MAPKK$^{Byr1.DD}$, which carries aspartic acid substitution at these sites, was expected to act as a constitutively active MAPKK (Ozoe et al., 2002). We introduced the *MAPKK$^{byr1.DD}$* mutation at its chromosome locus and measured the activation profile of its target, MAPK^{Spk1} during the mating process. The increase of the **pp**MAPK^{Spk1} signal

141 in the *MAPKK*$^{byr1.DD}$ mutant strain was delayed compared to the wildtype strain and the
142 **pp**MAPK^{Spk1} accumulated at a slower rate (Fig. 1E, light green line, original membrane images in
143 Fig. S3). However, the level of **pp**MAPK^{Spk1} remained high after reaching its highest intensity at
144 around 16 hours after induction, resulting in a constitutive phosphorylation of MAPK^{Spk1} (Fig. 1E
145 and Supplementary Fig. S2C and S2D). This result highlights that the suggested de-
146 phosphorylation of **pp**MAPK^{Spk1} by phosphatases Pmp1 and Pyp1 (Didmon et al., 2002) is not
147 efficient in downregulating the pheromone signalling in the presence of MAPKK$^{Byr1.DD}$. The
148 MAPKK$^{Byr1.DD}$ strain is also less competent in finding the partner mating cell than cells with
149 wildtype MAPKK^{Byr1}. We also confirmed the intriguing *"fus"* (fusion deficient) phenotype of cells
150 expressing MAPKK$^{Byr1.DD}$ from its native promoter (Fig.1F) (Dudin et al., 2016; Ozoe et al., 2002).
151 These cells find their partners and pair up successfully but fail to fuse with each other, resulting
152 in *fus* phenotype. Consistent with the observed slower increase in **pp**MAPK^{Spk1} (Fig.1E) the
153 nuclear localisation of MAPK^{Spk1} was also delayed compared to Wildtype cells (Fig 1F). A strong
154 MAPK^{Spk1}-GFP signal was then observed in the nuclei of the paired *fus* cells and the nuclear
155 MAPK^{Spk1}-GFP signal persists even 24 hours after the induction of mating (Fig. 1F). Interestingly,
156 the projection tips of the paring cells often show increased MAPK^{Spk1}-GFP signal (Fig. 1F, yellow
157 arrows). These results conclude that MAPK^{Spk1} activation is highly influenced by the MAPKK^{Byr1}
158 status and phosphatases directly regulating MAPK^{Spk1} cannot counteract MAPKK$^{Byr1.DD}$.
159
160 **(3) The *ras1.G17V* mutation causes immediate but transient MAPK^{Spk1} activation**
161 The fission yeast equivalent of human oncogenic *ras.G12V* is *ras1.G17V,* which induces an
162 excessively elongated shmoo, and the cells fail to recognize a partner and become sterile (Fukui
163 et al., 1986; Nadin-Davis et al., 1986a). The "elongated shmoo" phenotype was interpreted as
164 an excess activation of the downstream pathway(s) of Ras1, leading to a prediction that the
165 *ras1.G17V* causes over-activation of MAPK^{Spk1} (Weston et al., 2013; Yamamoto, 1996). However,
166 no direct evidence has been provided.
167 Quantitation of the **pp**MAPK^{Spk1}-GFP in the *ras1.G17V* mutant showed an immediate increase of
168 the **pp**MAPK^{Spk1}-GFP upon induction of mating (Fig. 1G, Green line, original membrane images in
169 Fig. S3). However, the signal intensity declined gradually and by 16 hours after induction the
170 level was comparable to wildtype cells, indicating that down-regulation of **pp**MAPK$^{Spk1\text{-}GFP}$ is
171 effective, unlike in *MAPKK*$^{byr1.DD}$ mutant. Correspondingly, the cellular MAPK^{Spk1}-GFP signal also
172 declined 24 hours after induction of mating (Fig. 1H). Collectively, these observations indicate

173 that the down-regulation mechanism for **pp**MAPK^{Spk1} is robust and resistant to Ras1.G17V. It
174 was also noted that the peak intensity of the **pp**MAPK^{Spk1} was somewhat lower and the rate of
175 signal reduction was slightly decreased compared to wildtype cells (Fig. 1G).
176
177 **(4) The elongated *ras1.G17V* shmoos develop with a minimum level of MAPK^{Spk1}: neither**
178 **amplitude nor duration of ppMAPK^{Spk1} signal influences the *ras1.G17V* phenotype**
179 Having observed that *MAPKK$^{byr1.DD}$* and *ras1.G17V* show different MAPK^{Spk1} activation profiles
180 (sustained vs transient) and different morphological phenotypes ("*fus*" vs elongated), we
181 examined a link between the MAPK^{Spk1} activation profiles and the cell morphology. The
182 MAPK^{Spk1} phosphorylation profile of the cells harbouring both *ras1.G17V* and *MAPKK$^{byr1.DD}$*
183 mutations (*ras1.G17V MAPKK$^{byr1.DD}$* double mutant) was comparable to the cells harbouring
184 *MAPKK$^{byr1.DD}$* mutation only; it showed a slow increase of the **pp**MAPK^{Spk1}-GFP level, which
185 reached the plateau at about 16 hours after induction of mating (Fig. 2A, red line, original
186 membrane images in Fig. S3). The nuclear **pp**MAPK^{Spk1}-GFP signal in the *ras1.G17V MAPKK$^{byr1.DD}$*
187 double mutant was also present 24 hours after induction of mating, unlike the *ras1.G17V* single
188 mutant cells, confirming that the *ras1.G17V MAPKK$^{byr1.DD}$* double mutant cells retained a high
189 **pp**MAPK^{Spk1} level. Thus, in terms of the activation status of MAPK^{Spk1}, *MAPKK$^{byr1.DD}$* is epistatic to
190 *ras1.G17V*.
191 In terms of cell morphology, the *ras1.G17V MAPKK$^{byr1.DD}$* double mutant cells showed the
192 "elongated" *ras1.G17V* phenotype (Fig. 2B), but not the "paired" *MAPKK$^{byr1.DD}$* phenotype.
193 Therefore, *ras1.G17V* was epistatic to *MAPKK$^{byr1.DD}$* in terms of the elongated shmoo
194 morphology.
195 Interestingly, obvious shmoo formation in the *ras1.G17V MAPKK$^{byr1.DD}$* double mutant was first
196 noticed 16 hours after induction of mating, much later than the *ras1.G17V* single mutant, but as
197 a similar timing as the *MAPKK$^{byr1.DD}$* single mutant (Fig. 2B). Given the slow increase of the
198 **pp**MAPK^{Spk1} signal in mutants harbouring the *MAPKK$^{byr1.DD}$* mutation, we predicted that the
199 delayed appearance of the *ras1.G17V* shmoo meant that the *ras1.G17V* shmoo formation still
200 requires a certain level of MAPK^{Spk1} activity. Indeed, when *MAPKK^{byr1}* was deleted in the
201 *ras1.G17V* mutant, not only was the MAPK^{Spk1} activation and nuclear MAPK^{Spk1}-GFP signal
202 abolished (Fig. S1F), but also shmoo formation was abrogated as in the *MAPKK$^{byr1}\Delta$* single
203 mutant (Fig. 2C). Based on these observations, we concluded that the cell morphology is
204 determined by the molecular status of Ras1, and not by the MAPK^{Spk1} activation profile. Yet, the

205 *ras1.G17V* phenotype still requires MAPK^{Spk1} activity, which determines the timing of shmoo
206 formation.
207
208 **(5) Cdc42 is required for the shmoo formation but not for the MAPK^{Spk1} activation**
209 During the vegetative cycle, *ras1Δ* cells show spherical cell morphology (Fukui et al., 1986;
210 Nadin-Davis et al., 1986a) and polarised localisation of active Cdc42 is compromised (Kelly and
211 Nurse, 2011), (Fig. 4C, D), indicating that Ras1 is involved in Cdc42 activation. The GTP-loaded
212 Cdc42 is then predicted to activate the downstream Ste20-like kinase, Pak1/Shk1 (Endo et al.,
213 2003; Marcus et al., 1995; Ottilie et al., 1995; Verde et al., 1995), resulting in actin
214 reorganisation and shmoo formation under mating conditions (Bendezu and Martin, 2013;
215 Merlini et al., 2016).
216 To confirm that Cdc42 acts downstream of Ras1, we generated a double mutant strain
217 harbouring *ras1.G17V* and deletion of *scd1*, encoding a GDP-GTP exchanging factor for Cdc42
218 (Cdc42-GEF^{Scd1}). The *ras1.G17V* elongated shmoo phenotype was lost in the double mutant and
219 instead, the cells showed a mating-deficient phenotype similar to the *cdc42-GEF^{scd1}Δ* single
220 mutant (Fig 3A). The result supports the model that Cdc42 acts downstream of Ras1 to cause
221 morphological changes.
222 Intriguingly, in the strains harbouring the *cdc42-GEF^{scd1}Δ* mutation, a nuclear MAPK^{Spk1}-GFP
223 signal appeared (Fig. 3A), indicating that activation of MAPK^{Spk1} may not be impaired by lack of
224 active Cdc42. This was unexpected because in a previous study, it was predicted that activation
225 of Cdc42 contributes to activation of MAPKKK^{Byr2} (Tu et al., 1997). To clarify this issue, we
226 measured **pp**MAPK^{Spk1} in the *cdc42-GEF^{scd1}Δ* mutant. Strikingly, in these cells MAPK^{Spk1}
227 activation occurred with a reproducible advancement of the initial activation timing compared
228 to the wildtype cells (Fig. 3B, original membrane images in Fig. S3). The result shows that
229 MAPK^{Spk1} activation does not require Cdc42 activity. Additionally, the faster activation of
230 MAPK^{Spk1} raises the interesting possibility that two Ras1 effectors, MAPKKK^{Byr2} and Cdc42-
231 GEF^{Scd1}, are competing with each other for activated Ras1, thus, lack of Cdc42-GEF^{Scd1} results in
232 an advanced MAPK^{Spk1} activation (modelled in Fig. 7A).
233 Substantial MAPK^{Spk1} activation in the *cdc42-GEF^{scd1}Δ* mutant means that the mating deficiency
234 of this mutant is unlikely to be the result of the lack of MAPK^{Spk1} activation. Indeed, introduction
235 of *MAPKK$^{byr1.DD}$* to the *cdc42-GEF^{scd1}Δ* mutant did not restore the mating deficient phenotype,
236 even though nuclear MAPK^{Spk1}-GFP highly accumulated (Fig. 3C). The result shows that active

237 Cdc42 function is absolutely required for the mating process regardless of the MAPK^{Spk1}
238 activation status. Taken together with the essential role of MAPK^{Spk1}, we concluded that the
239 mating pheromone signalling feeds into at least two pathways, MAPK^{Spk1} and Cdc42.
240
241 **(6) Ras1 activates two effector pathways, MAPK^{Spk1} and Cdc42.**
242 In order to further clarify the role of Ras1 we examined the MAPK^{Spk1} activation status and cell
243 morphology in the following four strains: *ras1Δ* mutant, *ras1Δ MAPKK$^{byr1.DD}$* double mutant,
244 *MAPKKK^{byr2}Δ* mutant and *MAPKKK^{byr2}Δ MAPKK$^{byr1.DD}$* double mutant. As mentioned earlier,
245 deletion of *ras1* causes cells to show a round morphology (Fig. 3F), with reduced cortical signal
246 of CRIB-GFP, an indicator of the active GTP-bound form of Cdc42, showing that Cdc42 activation
247 is compromised (Fig.4C, D). *ras1* deletion also causes substantial reduction, but not complete
248 elimination, of the **pp**MAPK^{Spk1} (Fig. 3D, red line, and Supplementary Fig. S4A); thus, Ras1 plays
249 an important role in activating both Cdc42 and MAPK^{Spk1} pathways. Introduction of the
250 *MAPKK$^{byr1.DD}$* mutation into the *ras1Δ* mutant cells induces the constitutive **pp**MAPK^{Spk1} (Fig. 3D,
251 green line and Supplementary Fig. S4A) but does not affect the round cell morphology and cells
252 remain sterile (Fig. 3F, the 2nd left panel. Note the accumulating MAPK^{Spk1}-GFP at 16 hours after
253 induction of mating), as was the case for the *Cdc42-GEF^{Scd1}Δ MAPKK$^{byr1.DD}$* double mutant (Fig.
254 3C).
255 In a striking contrast, the sterile phenotype of the *MAPKKK^{byr2}Δ*, associated with complete lack
256 of shmoo formation (Fig. 3F, the 2nd right panel), was converted to the "*fus*" phenotype, when
257 combined with the *MAPKK$^{byr1.DD}$* mutation (Fig. 3F, the far right panel). As expected, the
258 *MAPKKK^{byr2}Δ MAPKK$^{byr1.DD}$* double mutant shows MAPK^{Spk1} constitutive activation (Fig. 3E and
259 Supplementary Fig. S4B). Thus, unlike the cases of *scd1Δ* or *ras1*Δ, lack of *MAPKKK^{byr2}* can be
260 bypassed by constitutive activation of MAPK^{Spk1}, indicating that the sole role of MAPKKK^{Byr2} is to
261 activate the MAPK^{Spk1} unlike its upstream activator, Ras1, which also activates Cdc42 pathway (a
262 model presented in Fig. 7A).
263
264 **(7) Ras1.G17V causes accumulation of Cdc42-GTP at the cell cortex.**
265 Having observed a relatively mild influence of Ras1.G17V towards the MAPK^{Spk1} activation, we
266 next examined whether the Cdc42 pathway was affected by the *ras1.G17V* mutation. We
267 visualized the active GTP-bound form of Cdc42 (Cdc42^{GTP}) using CRIB-GFP that specifically binds
268 to Cdc42^{GTP} (Tatebe et al., 2008). As previously observed, dynamic foci of CRIB-GFP appeared on

269 the cell cortex upon induction of mating (Bendezu and Martin, 2013)(Fig. 4A and B). In our
270 experimental condition, more than 80% of wildtype cells showed the cortical CRIB-GFP signal at
271 4.5 hours after induction of mating (Fig. 4B). The cortical CRIB-GFP foci became concentrated at
272 the site of mating and quickly disappeared once cells fused successfully to form zygotes (Fig. 4A
273 and B). In striking contrast, in the *ras1.G17V* mutant cells, the cortical CRIB-GFP signal persisted,
274 often at the elongated tip end of the cells, even 12.5 hours after induction of mating (Fig. 4A
275 and B). The signal could still be seen in about 40% of the cells 22.5 hours after induction of
276 mating (Fig. 4A and B). The result shows that the Cdc42 pathway is excessively activated in the
277 *ras1.G17V* mutant and the localisation pattern of $Cdc42^{GTP}$ indicates that the signature
278 "elongated" *ras1.G17V* morphological phenotype is caused by deregulation of the Cdc42
279 pathway.
280 Ras1-mediated Cdc42 pathway activation has been also indicated during the vegetative growth
281 where the *ras1Δ* mutant shows a round cell morphology (Chang et al., 1994; Kelly and Nurse,
282 2011). However, unlike during the mating process, the *ras1.G17V* mutation does not cause an
283 obvious morphological phenotype during the vegetative growth. We predicted that, during the
284 vegetative growth, rigorous negative regulation occurs for Cdc42 by GTPase activation
285 protein(s) (GAPs), such as Rga4 (Das et al., 2007; Kelly and Nurse, 2011; Tatebe et al., 2008) to
286 counteract the effect of *ras1.G17V*. To examine this possibility, we compared Cdc42 activation
287 status of vegetatively growing wildtype, *ras1*Δ, *ras1.G17V*, *rga4Δ*, and *rga4Δ ras1.G17V* double
288 mutant cells (Fig. 4C and D). As previously described, CRIB-GFP showed a clearly polarized signal
289 at the growing cell tips in the wildtype strain (Tatebe et al., 2008)(Fig. 4C and D). In the *ras1*Δ
290 mutant, the cells were round and CRIB-GFP signal on the cell cortex had largely disappeared as
291 was seen in the *cdc42-GEF*^{scd1}Δ mutant (Kelly and Nurse, 2011). In contrast, the cortical CRIB-
292 GFP signal was clearly increased in the *ras1.G17V* single mutant although the cell morphology
293 appeared largely similar to the wildtype cells (Fig. 4C, D). These results indicate a direct
294 involvement of Ras1 in activating Cdc42. Meanwhile, the *rga4Δ* mutant cells showed slight
295 alterations to the cell morphology, accompanied with less polarized distribution of cortical CRIB-
296 GFP signal, as has been reported (Fig. 4C and D) (Das et al., 2007; Kelly and Nurse, 2011; Tatebe
297 et al., 2008). Strikingly, the *rga4Δ ras1.G17V* double mutant showed a clear morphological
298 alteration (big round cells) and the strongest cortical CRIB-GFP signal among all the mutants
299 examined (Fig. 4C and D). The result fits well with our hypothesis that Ras1.G17V is activating

300 Cdc42 even during vegetative growth, but the overall effect of Ras1.G17V is counteracted by the
301 Cdc42-GAP, Rga4.
302
303 **(8) Ras1 and an adaptor protein Ste4 are both necessary to fully activate MAPKKK^{Byr2}**
304
305 Although Ras1 clearly plays the major role to activate MAPK^{Spk1}, a marginal, but detectable level
306 of **pp**MAPK^{Spk1} was still induced in the *ras1Δ* mutant (Fig. 3D and Supplementary Fig. S4A),
307 indicating that there is a Ras1-independent mechanism to activate MAPK^{Spk1}. Previous studies
308 proposed an adaptor protein, Ste4, to be involved in the activation of MAPKKK^{Byr2}(Barr et al.,
309 1996; Okazaki et al., 1991; Ramachander et al., 2002; Tu et al., 1997). We therefore examined
310 whether Ste4 is required for MAPK^{Spk1} activation.
311 In constrast to the *ras1Δ* mutant, we detected virtually no MAPK^{Spk1} phosphorylation in the
312 *ste4Δ* mutant (Fig. 5A and Supplementary Figure S4C), indicating that the adaptor^{Ste4} is a
313 prerequisite for the MAPK^{Spk1} activation and the **pp**MAPK^{Spk1} signal observed in the *ras1Δ*
314 mutant is dependent on Ste4 function. Introduction of *ras1.G17V* mutation neither restored the
315 MAPK^{Spk1} activation nor mating (Fig. 5A, B), thus, activation of Ras1 cannot take over Ste4
316 function. In a striking contrast, the *ste4Δ MAPKK$^{byr1.DD}$* double mutant showed the *"fus"*
317 phenotype as the *MAPKK$^{byr1.DD}$* single mutant cells and induced constitutive MAPK^{Spk1} activation,
318 indicating that Ste4 is solely required for MAPK^{Spk1} activation (Fig. 5A, B).
319 Taken together, MAPKKK^{Byr2} is activated through a mechanism involving both Ras1 and Ste4, but
320 Ste4 only conveys the signal towards the MAPK^{Spk1}, while Ras1 also activates Cdc42.
321
322 **(9) Ste6, a Ras1 GTP-GDP exchange factor, contributes to both the MAPK^{Spk1} and the Cdc42**
323 **pathway activation**
324 There are two GDP-GTP exchange factors (GEFs) identified for Ras1: Ste6 and Efc25 (Hughes et
325 al., 1990; Tratner et al., 1997). As to the functional differences, Ste6 is essential for mating but is
326 dispensable during the vegetative cycle whilst Efc25 is dispensable for mating but is required to
327 maintain the cell morphology during the vegetative growth (Hughes et al., 1990; Tratner et al.,
328 1997). There has been an interesting proposition that Ste6 may specifically help Ras1 to activate
329 the MAPK^{Spk1} pathway, but not the Cdc42 pathway, whilst Efc25 specifically facilitates Ras1 to
330 activate the Cdc42 pathway (Papadaki et al., 2002). We examined this hypothesis by monitoring

331 the MAPK^{Spk1} activation status and conducting genetic epistasis analysis of *ras1.G17V* and
332 *MAPKK$^{byr1.DD}$* in the *ste6Δ* mutant.
333 In *ste6Δ* cells, MAPK^{Spk1} phosphorylation was found somewhat reduced but occurred at a clearly
334 detectable level. The signal increased when the *ras1.G17V* mutation was introduced (Fig. 5C and
335 Supplementary Figure S4D). When *ste6Δ and MAPKK$^{byr1.DD}$* were combined, MAPK^{Spk1} signalling
336 recapitulated the *MAPKK$^{byr1.DD}$* activation profile (Fig. 5C and Supplementary Figure S4D).
337 Nonetheless, the "pheromone-insensitive sterile" morphology of *ste6Δ* was only rescued by
338 *ras1.G17V*, as previously reported, exhibiting the "elongated" phenotype (Hughes et al., 1990),
339 but not by MAPKK$^{byr1.DD}$ (Fig. 5D). The result indicates that, unlike *ste4Δ* mutant, the mating
340 deficiency of *ste6Δ* is not caused by mere lack of MAPK^{Spk1} activation but by lack of Ras1
341 activation. We concluded that Ste6 functions to activate Ras1, which then activates *both* the
342 MAPK and Cdc42 pathways in response to pheromone signalling.
343
344 **(10) Activation mutant of Gpa1 mimics the full pheromone signalling**
345 In order to generate an integrated prototype Ras signalling model, we further investigated the
346 upstream signal input machinery. Previous studies showed that Gpa1 plays the primary role in
347 pheromone signalling (Obara et al., 1991). In agreement, in the *gpa1Δ* mutant we detected no
348 MAPK^{Spk1} activation nor nuclear accumulation of MAPK^{Spk1}-GFP (Fig. 6A, B and Supplementary
349 Fig. S5A). Introducing the *ras1.G17V* to the *gpa1Δ* strain did not rescue the complete lack of
350 *MAPK^{Spk1}* activation nor did it induce a shmoo-like morphological change (Fig. 6A, B and
351 Supplementary Fig. S5A), supporting our earlier observation that a Ras1-independent
352 mechanism, involving Ste4 is essential for MAPK^{Spk1} activation. Meanwhile, introducing the
353 *MAPKK$^{byr1.DD}$* mutation caused the constitutive activation of MAPK^{Spk1} (Fig. 6A and
354 Supplementary Fig. S5A), but cells showed no morphological change (Fig. 6B). When both
355 *ras1.G17V* and *MAPKK$^{byr1.DD}$* mutations were introduced into the *gpa1Δ* strain, MAPK^{Spk1} was
356 activated and a shmoo-like morphological change occurred (Fig. 6A, B and Supplementary Fig.
357 S5A). Therefore, activation of both of these two molecules is required and sufficient to mimic
358 the pheromone signalling.
359 To further confirm that the Gpa1 is a central component of pheromone signalling, we looked
360 into the MAPK^{Spk1} activation status in the constitutively active *gpa1.QL* mutant, which exhibits a
361 "shmoo-like" morphological change in the heterothallic *h$^-$* strain without the mating partner
362 (Obara et al., 1991).

363 Upon nitrogen starvation, the *h⁻ gpa1.QL* mutant strain showed morphological changes and a
364 strong MAPK^{Spk1} activation (Fig. 6C red line, Fig. 6D and Supplementary Fig. S5B). This response
365 was largely dependent on the Ras1 function as the *h⁻ gpa1.QL ras1Δ* double mutant exhibited a
366 significantly reduced level of **pp**MAPK^{Spk1} and a round cell morphology, two typical features of
367 *ras1Δ* cells (Fig. 6C, D and Supplementary Fig. S5B). On the other hand, the *h⁻ ras1.G17V* single
368 mutant showed a very low level of MAPK^{Spk1} activation, comparable to the one observed in the
369 *h⁻* wildtype strain, with no apparent morphological alternation, confirming that sole activation
370 of Ras1 does not substitute the pheromone signalling.
371 The *h⁻ MAPKK$^{byr1.DD}$* mutant induced a strong constitutive MAPK^{Spk1} activation, confirming that
372 the MAPKK$^{Byr1.DD}$ molecule can activate MAPK^{Spk1} regardless of the pheromone signal input (Fig.
373 6C, light-blue line and Supplementary Fig. S5B). However, cell morphology was unchanged (Fig.
374 6D). Collectively, these results support the model where Gpa1 acts as the central transducer of
375 the pheromone signalling, which can be mimicked only if both MAPK^{Spk1} and Ras1 are activated.
376
377 **(11) A holistic modelling framwork of MAPK^{Spk1} activation**
378 Based on quantitative **pp**MAPK^{Spk1} measurements in wildtype and various mutant strains (Fig.
379 1C, E, G, and Fig. 3B), we constructed a mathematical model of the MAPK^{Spk1} signalling
380 dynamics. The aim of the model is to test whether a simple competition of the MAPK and the
381 Cdc42 pathways for a shared pool of active Ras^{GTP}, can explain why the *scd1Δ* strain shows the
382 similar **pp**MAPK^{Spk1} activation profile as the *ras1.G17V* strain.
383 We designed a reductionist model of 6 ordinary differential equations to represent key steps of
384 pheromone signalling (Fig. 7A, Supplementary Fig. S6 and materials and methods). Model
385 simulations and parameter estimations were performed in COPASI (Hoops et al., 2006) and
386 details of the modelling process are described in Materials and Methods. Each biochemical
387 process is referred as [L1]-[L10] as depicted in Fig. 7A. All the signalling components were set to
388 be in close proximity, based on our own observation (Fig. 1 and Fig. 4) and recent series of
389 localization studies (Dudin et al., 2016; Merlini et al., 2016; Merlini et al., 2018). This allowed the
390 model to predict some signaling to involve protein-protein interactions.
391 The framework of the modelling process is as follows: Genes encoding pheromones, receptors,
392 Gpa1, Ste4 and Ste6 are all known to be under regulation of Ste11, the master transcriptional
393 regulator for meiotic genes (Hughes et al., 1994; Mata and Bahler, 2006; Mata et al., 2002; Mata
394 et al., 2007; Sugimoto et al., 1991) and these components are grouped into the Pheromone

395 Sensing (PS) unit. During the vegetative growth, the PS unit is set to zero. Nitrogen starvation
396 activates Ste11 (Kjaerulff et al., 2007; Sugimoto et al., 1991), which induces the PS unit [L1]. The
397 PS unit activates MAPKKK^{Byr2} in a twofold manner: Directly by Ste4 [L3] and through Ras1
398 [L4](Fig. 7A). Activated MAPKKK^{Byr2} then triggers activation of MAPKK^{Byr1} [L5] that activates
399 MAPK^{Spk1} [L6]. Since activated MAPK^{Spk1} further activates Ste11 (Kjaerulff et al., 2005), MAPK^{Spk1}
400 has a positive feedback loop on its own expression via Ste11 [L2,L7] (Fig. 7A).
401 As the pheromone signalling was found to induce a transient **pp**MAPK^{Spk1} peak (Fig. 1C),
402 **pp**MAPK^{Spk1} activity is ought to be regulated by a delayed downregulation. Because the
403 *MAPKK$^{byr1.DD}$* mutant completely lacks downregulation (Fig. 1E), downregulation occurring
404 downstream of MAPKK^{byr1} (e.g.: Pyp1 and Pmp1) were considered physiologically insignificant.
405 Meanwhile, Sxa2 (a serine carboxypeptidase against a mating pheromone P-factor) and Rgs1 (a
406 regulator of Gpa1), both of which are induced upon successful pheromone signalling (Imai and
407 Yamamoto, 1992; Mata and Bahler, 2006; Pereira and Jones, 2001; Watson et al., 1999),
408 receptor internalization (Hirota et al., 2001) and regulation of the *mapk^{spk1}* transcript or other
409 components by antisense RNA (Bitton et al., 2011) fit well to the criteria for the negative
410 feedback. We represented all these potential negative feedbacks collectively as a single circuit,
411 [L8]. Importantly, this downregulation [L8] works unperturbed in the presence of Ras1.G17V, by
412 acting through the Ste4-dependent MAPKKK^{Byr2} activation process (Fig. 1G, Fig. 7A).
413 Ras1-GTP activates both the MAPKKK^{Byr2} and the Cdc42 pathways [L9] (Chang et al., 1994). As
414 opposed to previous expectations that active Cdc42^{GTP} is required to activate MAPKKK^{Byr2} (Tu et
415 al., 1997), deletion of Cdc42-GEF^{Scd1} does not compromise MAPK^{Spk1} activation (Fig. 3B) and
416 rather, it makes **pp**MAPK^{Spk1} dynamics remarkably similar to that of the Ras1.G17V strain (Fig.
417 3B and Fig. 1G, plotted together in Fig. 7B): in both cases, **pp**MAPK^{Spk1} peaks earlier than the
418 wildtype case. At a molecular level, reactions depleting the Ras1^{GTP} pool are compromised in
419 both strains. Therefore, to explain these observations, we hypothesized that MAPK^{Spk1} and
420 Cdc42 pathways are competing for the common Ras1^{GTP} pool. In this manner, one of the
421 pathways can modulate the other by changing the amount of unbound (available) Ras1^{GTP}.
422 In support of this prediction, we showed that binding of recombinant Ras1.G17V^{GTP} to a
423 MAPKKK^{Byr2} fragment was reduced by the presence of a Cdc42-GEF^{Scd1} fragment *in vitro* (Fig. 7C,
424 D). In this assay, bacterially expressed GST tagged fragments of both MAPKKK^{Byr2} (65-180) and
425 Cdc42-GEF^{Scd1} (760-872) showed a specific binding towards the GTP-loaded Ras1.G17V (1-172)
426 (Fig. 7C). However, the binding of Ras1.G17V^{GTP} to MAPKKK^{Byr2} was substantially decreased

427 when the Cdc42-GEF^{Scd1} fragment was added (Fig. 7D). The result likely refects the intrinsic
428 biochemical competitive nature of MAPKKK^{Byr2} and Cdc42-GEF^{Scd1} for Ras1 binding. As we show
429 below, this simple hypothesis successfully describes pheromone signalling mutants tested in this
430 study, suggesting that no unproven cross links are necessary to reproduce the *in vivo*
431 observations.
432 An intriguing common feature observed in both Cdc42-GEF^{scd1}Δ and *ras1.G17V* mutants is that
433 **pp**MAPK^{Spk1} peaks not only at an earlier time point, but also with a *lower amplitude* as
434 compared to the wildtype. If increased Ras1^{GTP} levels simply accelerate MAPK^{Spk1} activation, as
435 has been conventionally assumed, **pp**MAPK^{Spk1} production should peak earlier *and higher*
436 (Supplementary Fig S7B, best fit out of 1000 global fits), and the addition of Ras1^{GTP} only should
437 increase the amplitude, but not affect timing (Supplementary Fig S7C). We confirmed these
438 results in the best models from 1000 global fits (Materials and Methods). The comparison
439 between our experimental results and the *in silico* predictions suggests that the role of Ras1^{GTP}
440 is more complex than previously thought.
441 Strikingly, if we hypothesize that Ras1^{GTP} also contributes to the negative feedback [L10] (Fig.
442 7A), we recapitulate the "*earlier and lower*" peak of **pp**MAPK^{Spk1} in both the *ras1.G17V* and the
443 Cdc42-GEF^{scd1}Δ mutants (Fig. 7B). We currently do not have a direct experimental evidence to
444 support [L10]. However, considering the fact that Ras1^{GTP} likely acts as a physical signalling hub
445 at the cell cortex, mediating MAPKKK^{Byr2} recruitment and activation, which leads to recruitment
446 of MAPKK^{Byr1} and MAPK^{Spk1}, Ras1^{GTP} may work as a two-way amplifier, both assisting localized
447 MAPK^{Spk1} activation at the shmoo site, as well as helping the negative feedback by concentrating
448 the affected molecules.
449 The model successfully recapitulated the experimental results for wildtype, *ras1.G17V*,
450 MAPKK$^{Byr1.DD}$ and *cdc42-GEF^{scd1}Δ* mutants (Fig. 7B). To test the predictive capacity of the model,
451 we next performed an *in silico* experiment where we titrated increasing amounts of Ras1^{GTP} in
452 the wildtype condition before nitorgen removal. In agreement with our hypothesis, we obtained
453 a *ras1.G17V*-like **pp**MAPK^{Spk1} activation profile with increasing amount of Ras1^{GTP}, i.e., the
454 **pp**MAPK^{Spk1} peaks earlier with a lower peak intensity (Fig. 7E). The result further supported that
455 Ras1^{GTP} availability alone is sufficient to explain both the *ras1.G17V* and *Cdc42-GEF^{scd1}Δ*
456 phenotypes.
457 To further test the predictive value of the model, we asked whether it could predict **pp**MAPK^{Spk1}
458 dynamics in the 21 other strains, which were measured (Fig. 2-6), but not used for fitting the

459 model. We implemented each mutation in the wildtype model (Supplementary Table S2) and
460 the model accurately predicted relative **pp**MAPK^{Spk1} dynamics in 17 cases, or showed
461 predicitons in close proximity to the observed **pp**MAPK^{Spk1} dynamics in the 4 remaining cases
462 (Fig. 7F). Concluding from these results, our model likely represents the physiological framework
463 of fission yeast RAS-MAPK signalling.
464

465 **Discussion**

466

467 By quantitating the MAPK^{Spk1} and Cdc42 activation status during the mating process and
468 conducting epistasis analysis between numerous signalling mutants, we showed that Ras1
469 coordinates activation of both the MAPK^{Spk1} cascade and the Cdc42 pathway. Furthermore, we
470 revealed that the *ras1.G17V* mutant phenotype is caused by deregulation of Cdc42, rather than
471 altered activation of MAPK^{Spk1} in physiological setting. Based on the experimental data, we built
472 a mathematical model, incorporating an assumption that two Ras1 effectors, Cdc42-GEF^{Scd1} and
473 MAPKKK^{Byr2}, are competing for active Ras1. This is the first simulation of a physiological Ras
474 signalling network in a whole organism. The model faithfully recapitulates MAPK^{Spk1} activation
475 profiles in the wildtype and all mutant strains examined in this study. The model implies that
476 targeting one of the RAS effector pathways can potentially result in a complex outcome, rather
477 than simply shutting down the targeted effector pathway. We concluded that fission yeast
478 pheromone Ras signalling is not only defined by compartmentalisation (Onken et al., 2006) but
479 rather a coordination of events involving both the MAPK^{Spk1} and Cdc42 pathways.
480 Coordinated activation of MAPK and Cdc42 pathways upon pheromone stimulation is a
481 common feature shared by budding yeast pheromone signalling. In budding yeast, however, Ras
482 homologues are not involved in the process. β and γ subunits of the receptor-coupled trimeric
483 G-protein act as the hub to activate both pathways ((Hegemann et al., 2015; McClure et al.,
484 2015), reviewed in (Atay and Skotheim, 2017)). It is intriguing that the key hub moleucules are
485 evolutionary diverged in these yeast species whilst the effector pathways are conserved to bring
486 comparable biological outcomes.
487 In this study, we confirmed that Gpa1, the α subunit of the receptor-coupled trimeric G-protein,
488 is the central player of the pheromone signalling. It is likely that Gpa1 is the most downstream
489 molecule conveying the complete pheromone signal. Considering that all the pheromone
490 signalling components examined so far have been found at the shmoo site (Dudin et al., 2016;

491 Merlini et al., 2016; Merlini et al., 2018)(this study), an attractive hypothesis is as follows: firstly,
492 the activated pheromone receptor Map3/Mam2 locally activates Gpa1, which activates Ras1
493 and MAPK^{Spk1}. This then leads to a localised activation of the Cdc42, causing shmoo formation in
494 the direction of a mating partner (Fig. 8A).
495 The *ras1.G17V* mutation led to an immediate activation of MAPK^{Spk1} compared with the
496 wildtype cells. The G17V mutation of Ras1 is equivalent of G12V mutation of mammalian RAS,
497 which results in a substantial reduction of both intrinsic and GAP-mediated GTPase activities
498 (Trahey and McCormick, 1987). Therefore a larger fraction of Ras1 is expected to be in the
499 active GTP-bound form in the *ras1.G17V* mutant cells. By mathematical modelling, we showed
500 that the increased Ras1^{GTP} pool can explain a faster activation of MAPK^{Spk1}.
501 To our surprise, the constitutive Ras1.G17V mutation did not induce over-activation of
502 MAPK^{Spk1}. The attenuated MAPK^{Spk1} activation in the presence of Ras1.G17V indicated that an
503 efficient feedback mechanism is in place to counteract the effect of Ras1.G17V. Strikingly, the
504 same trend has been reported in the mouse model of the *K-ras^{G12D}* mutation integrated at the
505 endogenous chromosome locus (Tuveson et al., 2004). Therefore it is highly likely that the
506 MAPK cascade is generally robust against upstream oncogenic constitutive stimulation.
507 Based on our observation that the MAPK^{Spk1} is constitutively activated in the *MAPKK$^{byr1.DD}$*
508 mutant, we predict that the negative regulation occurs upstream of, or at the same level as,
509 MAPKK^{Byr1}, rather than phosphatases that directly regulate MAPK^{Spk1}. In humans, ERK is shown
510 to phosphorylate RAF proteins, the prototype MAPKKKs, to contribute to ERK signal attenuation
511 (Brummer et al., 2003; Dougherty et al., 2005; Ritt et al., 2010). In future studies it will be
512 important to determine whether MAPK^{Spk1} can directly downregulate MAPKKK^{Byr2} in a
513 physiological setting.
514 Our results also show that an adaptor^{Ste4} plays a crucial role in activating MAPKKK^{Byr2}, abolishing
515 **pp**MAPK^{Spk1} production even in the presence of *ras1.G17V* mutation. This suggests that the
516 adaptor^{Ste4} fits well to be one of the major targets by the negative feedback loop against
517 **pp**MAPK^{Spk1}. This mechanism is shared by budding yeast, where an adaptor protein, Ste50,
518 modulates MAPKKK^{Ste11} (Ramezani-Rad, 2003). In humans, although such an adaptor protein for
519 RAF proteins has yet to be identified, multiple RAF-interacting proteins, including 14-3-3
520 proteins, as well as formation of heterodimers between BRAF and CRAF, have been studied for
521 their Ras-independent mechanism to activate RAF proteins (Lavoie and Therrien, 2015).

522 Collectively, MAPK cascades seem to retain a general resistance to oncogenic RAS mutations in
523 physiological settings (Fig. 8B).
524 Whilst lack of Cdc42 activation does not impair MAPK^{Spk1} activation, we found that MAPK^{Spk1}
525 activity is required for shmoo formation even in the presence of Ras1.G17V (Fig. 2C). Therefore,
526 the two Ras1 effectors, Cdc42 and MAPK^{Spk1} pathways, are not completely separable. The
527 situation is reminiscent of the *K-ras^{G12D}* MEFs (Tuveson et al., 2004). In this system, the *K-ras^{G12D}*
528 MEFs showed morphological anomalies. As both ERK and AKT phosphorylation levels in the *K-*
529 *ras^{G12D}* MEFs resembled wildtype, these pathways unlikely caused the morphological
530 phenotype. Nonetheless, inhibitors against MAPK and PI3K pathways reverted the *K-ras^{G12D}*–
531 induced abnormal morphology back to the one similar to wildtype. The observation suggests
532 that MAPK and PI3K pathways somehow contribute to the *K-ras^{G12D}* morphological phenotype;
533 for example, a basal level of MAPK and PI3K pathway activation may be a prerequisite for the *K-*
534 *ras^{G12D}*–induced morphological anomalies.
535 The molecular mechanism of how MAPK^{Spk1} contributes to Cdc42 activation will require further
536 studies. Key components in pheromone signalling are transcriptionally up-regulated upon
537 pheromone signalling (Xue-Franzen et al., 2006). This is driven by MAPK^{Spk1}, which activates the
538 master transcriptional regulator Ste11 (Kjaerulff et al., 2005; Mata and Bahler, 2006; Xue-
539 Franzen et al., 2006). Therefore, the contribution of MAPK^{Spk1} to Cdc42 activation is expected to
540 occur, at least partly, through transcriptional activation.
541 In addition, localisation of signalling components may be regulated by MAPK^{Spk1}. In budding
542 yeast, MAPK^{Fus3} brings Cdc24, the GEF for Cdc42, to the shmoo site by phosphorylating an
543 adaptor protein Far1 (Hegemann et al., 2015), which otherwise sequesters Cdc24 into the
544 nucleus (Nern and Arkowitz, 2000; Shimada et al., 2000). Fission yeast does not have an obvious
545 Far1 homologue but MAPK^{Spk1} may also directly phosphorylate and activate Cdc42 and/or its
546 regulatory proteins such as Cdc42-GEF^{Scd1}, Scd2 or GAP-Cdc42^{Rga4}, all of which function at the
547 shmoo site during the mating (Bendezu and Martin, 2013; Dudin et al., 2016)(Fig.4 A and B). In
548 agreement with this hypothesis, a transient MAPK^{Spk1} and MAPKK^{Byr1} signal on the cell cortex
549 was observed during the mating process (Fig. 1)(Dudin et al., 2016). Localisation of MAPK at the
550 growing cell tips was also observed in other fungi including *S. cerevisiae* and *N. crassa* (Chen et
551 al., 2010; Fleissner et al., 2009; Maeder et al., 2007; van Drogen et al., 2001). In budding yeast,
552 MAPK^{Fus3} can directly phosphorylates Bni1, a formin that organises actin filaments, to facilitate

553 shmoo formation (Matheos et al., 2004). It will be important to determine whether this is also
554 the case in fission yeast.
555 Interestingly, during the vegetative growth when expression of $MAPK^{Spk1}$ is repressed,
556 Ras1.G17V is still capable of activating Cdc42 (Fig. 4C and D). Whether other MAPKs, such as
557 Sty1 or Pmk1, contribute to Cdc42 activation during the vegetative cell cycle will be an
558 important question to answer. Intriguingly, recent studies show that Sty1 inhibits, rather than
559 assists, establishment of the Cdc42 polarity module (Mutavchiev et al., 2016). Collectively, it is
560 likely that the Cdc42 polarity module is regulated in a context dependent manner by multiple
561 MAPKs in a range of ways.
562 In this study we revealed the vital contribution of Cdc42 to induce the *ras1.G17V* phenotype in
563 fission yeast pheromone signalling (Fig. 8B). In mouse models, small GTPases, Cdc42 and Rac,
564 are required for *H-ras*^{G12V} induced transformation (Malliri et al., 2002; Stengel and Zheng, 2012).
565 Therefore, oncogenic RAS-induced Cdc42/Rac misregulation may be a common basis of
566 oncogenicity of mutated-RAS-induced signalling. Specifically targeting this process may
567 therefore be an effective strategy against oncogenic RAS-driven tumourigenesis.
568
569

570 ## Materials and methods

571 ### Yeast strains and media

572 Genotypes of the *Schizosaccharomyces pombe* strains used are listed in the supplementary Table
573 S1. Gene disruption and 2xFLAG-GFP-tagging of genes were performed using the direct
574 chromosomal integration method described previously (Bahler et al., 1998; Funaya et al., 2012;
575 Wach, 1996). Fission yeast media (YE, MM-N and SPA) and basic genetic manipulations are
576 described in (Moreno et al., 1991).

577 ### Plate mating assay for synchronous mating

578 In order to induce synchronous mating, we established the "Plate mating assay" system as
579 follows: Cells were grown in YE supplemented with adenine (0.2g/L) until the cell density reaches
580 8-10 x 10^6 cells/ml. Cells were then washed with MM-N (1% glucose, supplemented with Leucine
581 40mg/L) using a filtration unit. These cells were resuspended to a cell density of 0.8-1x10^7cells/ml
582 in MM-N. In the timecourse experiments, this moment was considered time 0. 8x10^7cells were
583 re-filtered onto a PDVF membrane of 47 mm diameter (Millipore DVPP04700) in order to evenly
584 place the cells across the defined area. The filters bearing the cells over their surface were
585 carefully transferred onto sporulation agar plates (SPA+Leucine 40mg /L, 50ml SPA agar / 14cm
586 diameter for 6 membranes), cell side up, and incubated at 30°C. During the time course
587 experiments, at each time-point one membrane, which initially had 8x10^7cells at time 0, was
588 removed from the SPA plate and placed into 5 ml of ice-cold 20% trichloroacetic acid (TCA) in a
589 50 ml falcon tube. The tube was shaken vigorously to remove cells from the membrane. The tube
590 was briefly centrifuged and the membrane removed from the tube. The tube was then
591 centrifuged for 1 minute at 2000rpm to pellet cells. Supernatant was discarded, cells were
592 resuspended in 1 ml 20% TCA and transferred to a tube capable of storage at -80˚C. The cells were
593 pelleted again using a bench top centrifuge, supernatant discarded, and the pellet snap frozen in
594 liquid nitrogen. Tubes were stored at -80˚C ready for protein extraction.

595 ### Preparation of whole cell extracts

596 This method is based on that described by Keogh lab Protocols
597 (https://sites.google.com/site/mckeogh2/protocols). All steps were performed on ice unless
598 otherwise stated. Cell pellets were thawed on ice and resuspended in 250 µl 20% TCA. 250 µl of
599 acid washed glass beads (SIGMA) were added and sampled chilled on ice for 5 minutes. Cells
600 were broken in a FastPrep24 cell beater (MP Biomedicals, speed 6.5 x 1 minute x 3 with 1

601 minute intervals). Cell extracts were collected by piercing the bottom of tubes with a needle and
602 placing them into collection tubes and centrifuged at 2000 rpm for 1 minute. Beads were
603 washed with 300 µl of 5% TCA and centrifuged at 2000 rpm for 1 minute, this was repeated
604 twice. The contents of the collection tube were transferred to a 1.5 ml tube and centrifuged at
605 14K rpm for 10 minutes at 4°C. The liquid was discarded and the cell pellet washed with 750 µl
606 of 100% ethanol. Tubes were centrifuged briefly (~1min 14000rpm) again. Ethanol was
607 completely removed with a pipette and the pellet resuspended in 100 µl 1M Tris pH8.0 and 100
608 µl 3x protein loading buffer (Laemmli, 1970). Cell extracts were then heated for 5 minutes at
609 95˚C, centrifuged for 5 minutes at 14K rpm and the supernatant transferred to a fresh 1.5 ml
610 tube. Samples were stores at -20˚C.

611 **Western Blotting**

612 Protein extracts were subject to SDS-PAGE and were transferred to Immobilon-FL PVDF
613 membrane (Millipore). Membranes were blocked for a minimum of 1-hour in Odyssey Blocking
614 Buffer (OBB) (Li-cor) diluted 1:1 in PBS. Primary antibody incubation was carried out overnight
615 in OBB 1:1 in PBS with the anti phospho-p44/42 MAPK (Erk1/2) (Thr202/Tyr204) rabbit
616 monoclonal antibody (#4370 Cell Signaling technology. Used at 1:2000 dilution), the monoclonal
617 anti GFP antibody ((0.4mg/ml), Roche Cat No 11814460001. Used at a 1:2000 dilution) and the
618 anti α-tubulin antibody, TAT1 (generous gift from Keith Gull, 1:3000). Membranes were washed
619 3x10 minutes with 20 ml TBST (50 mM Tris, pH 7.4 – 150 mM NaCl – 0.1% Tween 20) whilst
620 gently shaking followed by secondary antibody incubation (IRDye 680LT goat anti-mouse
621 antibody, Li-cor 926-32211(1.0 mg/ml), 1:16,000 dilution and IRDye 800CW goat anti-rabbit
622 secondary antibody Li-cor 926-68020 (1.0 mg/ml), 1:16000 dilution in 0.01% SDS, 0.1% Tween
623 20 in OBB 1:1 PBS) for 1 hour in the dark to prevent fluorophore bleaching. This was followed by
624 2x 10 minute TBST washes and a 1x 10 minute TBS (50 mM Tris, pH 7.4 – 150 mM NaCl) wash
625 before scanning on the Odyssey CLx infrared Imaging System (Li-cor). Protein quantitation using
626 the Image Studio V2.1 software supplied with the Odyssey CLx scanner. The background method
627 used was median with a border of 3 pixels to the left and right of quantitation boxes.

628 **Quantitation of MAPK^{Spk1} phosphorylation**

629 To detect the activated MAPK^{Spk1}, whole cell extracts were prepared and Western blotting
630 analysis was carried out using the anti-phospho ERK antibody (#4370 Cell Signalling Technology)
631 that recognises the dual phosphorylation at the conserved TEY motif. Specificity of the antibody

632 against the phosphorylated MAPK^{Spk1} (**pp**MAPK^{Spk1}) in the fission yeast cell extracts was
633 confirmed before proceeding with further experiments as shown in Supplementary Fig. S1. As
634 described above in the "**Plate mating assay for synchronous mating**", during the time course
635 experiments, at each time-point, one membrane, which initially had 8x10^{7}cells at time 0, was
636 used to prepare the whole cell extracts. Then an equal volume of each sample was loaded to the
637 Western blotting. In this manner, we observed that the change of the protein level throughout
638 the mating process per a defined starting material. We noticed that the level of α-tubulin during
639 the wildtype mating process is relatively constant; less than 25% fluctuation throughout the
640 timecourse for all three biological replicates (an example shown in Fig. S2B). Based on these
641 observations, we chose to use α-tubulin as an internal control to quantitate the **pp**MAPK^{Spk1}
642 signal.
643 In order to quantitate **pp**MAPK^{Spk1} levels in wildtype, *byr1.DD*, *ras1.G17V* and *scd1Δ* mutants,
644 Western blotting of three biological replicates of time-course experiments was conducted
645 (original membranes presented in Fig. S3). Because the SDS-PAGE gels we used had only 25
646 wells, only two out of three biological replicates could be run simultaneously on the same gel.
647 The third replicate was run separately on a different gel as shown in Fig. S3 (A). Definite
648 measurement values of the third replicate were multiplied by a constant to bring the values
649 closest to the rest of the two replicates. In order to directly compare results of wildtype,
650 *byr1.DD*, *ras1.G17V* and *scd1Δ* mutants, technical replicates of Western blotting were generated
651 by directly comparing one of the biological replicates of each strain as follows: the third
652 replicate of the wildtype and *byr1.DD* samples (WT-3 and *byr1.DD*-3) (Fig. S3A), the second
653 replicate of the wildtype and *ras1.G17V* samples (WT-2 and *ras1.G17V* -2) and the second
654 replicate of the wildtype and *scd1Δ* samples (WT-2 and *scd1Δ* -2) (Fig. 3B).
655
656 **Cell Imaging for bright field and Spk1-GFP signals**

657 A Nikon Eclipse Ti-E microscope equipped with CoolLED PrecisExcite High Power LED
658 Fluorescent Excitation System, an Andor iXon EM-DU897 camera and aCFI Plan Apo VC
659 100x/1.4 objective was used for cell imaging to capture the morphology of cells and the
660 localisation of the GFP-tagged MAPK^{Spk1} during mating time-courses. For cell images presented
661 in Figure 4, a 2D array scanning laser confocal microscope (Infinity 3, VisiTech) was used (see
662 below). Each time point comprises 15-25 serial images with 0.4 µm intervals along the Z axis
663 taken to span the full thickness of the cell. All of the Spk1-GFP images were deconvolved using

664 the Huygens Essential Deconvolution software (Scientific Volume Imaging). Deconvolved images
665 were Z-projected (maximum intensity), cropped and combined using Fiji (Schindelin et al.,
666 2012).

667 **Imaging and quantitation of CRIB-GFP signal**

668 A 2D array scanning laser confocal microscope (Infinity 3, VisiTech) on a NikonTi-E microscope
669 stand equipped with a Hamamatsu Flash 4.0V2 sCMOS camera and a Plan Apo 100x/1.45
670 objective was used to capture CRIB-GFP signal to examine activation status of Cdc42. For images
671 presented in Fig. 4A, 25 serial Z images with step size of 0.25 µm were taken. Images were
672 deconvolved using Huygens Essential (Scientific Volume Imaging) and maximum intensity
673 projections are presented.

674 For images presented in Fig. 4C, for each image, 30-45 serial images with 0.2 µm interval along
675 the Z axis were taken to span the full thickness of the cell. Using FIJI software maximum
676 intensity Z-projections were created and used for quantitation. Intensity of GFP signal on the
677 cell cortex was measured using FIJI along one of the cell tips that shows stronger GFP signal as
678 indicated in an example image in Fig. 4D. 40 cells without septum were measured for each
679 strain. Quantified CRIB-GFP intensity traces were analysed in R (R Core Team http://www.R-
680 project.org/). First, rolling averages over +/-5 measurement points were calculated. Next, the X-
681 coordinates of these traces were aligned by their peak intensity. Finally, the average curve from
682 all aligned traces per strain was calculated, and displayed in Fig 4.D with respective standard
683 error of the mean curves (dashed lines). Analysis script will be accessible on the GiHub
684 repository upon publication (see availability section 1.1.16).

685 **Glutathione-S-transferase (GST) tag pull-down assays**

686 Fission yeast cDNA fragments encoding Ras1.G17V (1-172), Byr2 (65-180) and Scd1 (760-872)
687 were cloned in the pLEICS1 (Ras1.G17V) and pLEICS4 (Byr2 and Scd1) vectors (Protex [Protein
688 Expression Laboratory], University of Leicester) to produce N-terminally His6-tagged Ras1.G17V
689 (1-172), N-terminally GST-tagged Byr2 (65-180) and N-terminally GST-tagged Scd1 (760-872).
690 Constructs were expressed in *E.coli* BL21 Rosetta cells in LB. All bacteria cell lysates were
691 prepared in phosphate-buffered saline (PBS), pH 7.4.

692 His6-Ras1.G17V (1-172) was purified using Ni Sepharose 6 Fast Flow (GE Healthcare) and
693 dialysed into buffer A (20 mM Tris-Cl (pH 7.5), 100 mM NaCl, 5mM MgCl2, 1mM β-
694 mercaptoethanol). For GTP loading, buffer A of the Ras1.G17V (1-172) preparation was firstly

695 replaced by Exchange buffer (20 mM Tris-Cl (pH 7.5), 1mM EDTA, 1mM β-mercaptoethanol)
696 using a filtration unit (Amicon Ultra Centrifugal Filter Unit, 10K cut off, Millipore). GDP-GTP
697 exchange reaction was carried out by adding GTP and EDTA to a final concentration of 8 mM
698 and 12 mM respectively and incubating the sample at 37°C for 10 min. The exchange reaction
699 was terminated by adding MgCl2 to a final concentration of 20.5 mM. The resultant GTP-loaded
700 Ras1.G17V (1-172) was washed with buffer A using the filtration unit and immediately used for
701 the GST pull-down assays.

702 GST-Byr2 (65-180) and GST-Scd1 (760-872) were purified using glutathione sepharose 4B (GE
703 Healthcare). The proteins bound on the glutathione beads were washed with buffer A and used
704 for the GST pull-down assays together with the Ras1.G17V (1-172) preparation. For the
705 competition assays shown in Fig. 7D, Scd1 (760-872) fragment was prepared by cleaving it out
706 from the N-terminal GST, which was bound to the glutathione beads, using TEV protease.

707 GST pull-down assays were carried out by incubating Ras1.G17V (1-172) (GDP bound or GTP
708 bound) and GST-Byr2 (65-180) or GST-Scd1 (760-872) with or without Scd1 (760-872) fragment
709 at 4 ^{o}C for 30 min. Supernatant of the reaction was saved and mixed with the same volume of
710 the 3x loading buffer (Laemmli, 1970) to generate the "unbound" fraction. The remaining beads
711 were washed twice, resuspended in buffer A of the original volume and mixed with the same
712 volume of the 3x loading buffer to generate the "bound" fraction. Protein samples were run on
713 a SDS-PAGE gel and proteins were visualised by InstantBlue protein stain (Expedeon).
714 Quantitation of the intensities of Ras1.G17V (1-172) bands in Fig. 7D was carried out using Fiji
715 software.

716 **Mathematical Modelling**

717 We built a mathematical model in form of a system of ordinary differential equations (ODE) for
718 the dynamics of the signaling pathway downstream of the pheromone receptor. The model
719 consists of 6 ordinary differential equations representing 9 chemical reactions connecting 6
720 variables (1.1.14).

721 We focused on the competition between the MAPK^{Spk1} and Cdc42 pathways for active Ras1^{GTP}
722 molecules, but no other pathway "cross-talks" were instigated. We estimated the model
723 parameters from the measured time courses of **pp**MAPK^{Spk1} in wild type and the three key
724 mutant strains (*ras1.G17V*, *MAPKK$^{byr1.DD}$* and *Cdc42-GEF^{scd1}Δ*) examined in this study.

725 Time courses in these strains are precisely reproduced by the model, thereby we have made it
726 plausible that the competition between MAPK^{Spk1} and Cdc42 pathways is sufficient to cause the
727 **pp**MAPK^{Spk1} early activation phenotype observed in the *ras1.G17V* and *Cdc42-GEF^{scd1}Δ* mutants.

728 The model also successfully predicted the **pp**MAPK^{Spk1} temporal dynamics in the 21 other
729 mutant strains examined in this study (Fig.7D). We therefore concluded that the model may
730 serve as a general framework for pheromone signalling in *S. pombe* and can be used for further
731 *in silico* experimental design.

732 1.1.1 Pathway components

733 Previous studies showed that more than 20 proteins, more than 20 biochemical and at least 10
734 relevant genetic interactions are involved in the fission yeast pheromone pathway (Mata and
735 Bahler, 2006; Mata et al., 2002; Otsubo and Yamamoto, 2012; Xue-Franzen et al., 2006). Given
736 the complexity of the pathway, and in order to attain the simplest model fulfilling our criteria,
737 several pathway components and steps were simplified in the presented model as detailed
738 below.

739 1.1.2 Nitrogen withdrawal, and subsequent pathway activation

740 Nitrogen starvation induces the expression of the meiotic transcriptional regulator Ste11, which
741 then induces expression of the key components of the pheromone pathway (Egel, 2004).
742 Experimentally, this initial process occurs as a step-like nitrogen removal from the media, which
743 is implemented as a change of starvation signal *S* from 0 →1, i.e. activator step-function in the
744 model.

745 The response to starvation is two fold. First of all, various signaling components under the
746 regulation of Ste11 are induced: the pheromone (M- or P-factor), the pheromone receptors
747 (Map3 or Mam2), the receptor-coupled G-protein (Gpa1), a GDP-GTP exchange factor (GEF) for
748 Ras1 (Ste6) and an adaptor Ste4. For simplicity, the pheromone sensing and upstream signal
749 transduction machinery is modelled by one variable, called here the Pheromone Sensing (PS)
750 unit (Fig. 7A). The PS unit is sometimes also referred to as the "upstream pheromone pathway".
751 Induction of the PS unit by Ste11 as well as pheromone binding, subsequent Gpa1 activation
752 and consequential activation of Ste4 and Ste6 are all encompassed in the process [L1] in Fig. 7A.
753 As Ste11 is induced by starvation, PS is also created proportionally to starvation sensing (***S,*** Eq.
754 1). Since downregulation of PS occurs in form of a long negative feedback loop, the term
755 $v_{downregulation}(PS)$ depends on **pp**MAPK^{Spk1} (Eq. 2); and it is explained in a later section.

Eq. 1

$$\frac{d(PS)}{dt} = S \cdot k_0 - v_{downregulation}(PS)$$

Eq. 2

$$v_{downregulation}(PS) = k_8 \cdot \mathbf{pp}\mathrm{MAPK}^{\mathrm{Spk1}} \cdot PS$$

The second response to starvation is the activation of a basal $MAPK^{Spk1}$ transcription through Ste11. $MAPK^{Spk1}$ is then activated by phosphorylation to $ppMAPK^{Spk1}$, if (active) $ppMAPKK^{Byr1}$ is present. This basal activation (F1) is also proportional to starvation sensing (Eq. 3), also see (*Eq. 7*) and section (1.1.6) for details.

Eq. 3

$$F_1 = S \cdot k_1 \cdot \boldsymbol{pp}\mathrm{MAPKK}^{\mathrm{Byr1}} activity$$

1.1.3 The upstream pheromone pathway (PS)

The PS unit activates the downstream MAPK cascade in two ways:

1. PS activates $Ras1^{GDP}$ (process [L4] in Fig. 7A), which in turn activates $MAPKKK^{Byr2}$, and
2. Ste4, a PS unit component, directly activates $MAPKKK^{Byr2}$ independently of Ras1 (process [L3] in Fig. 7A).

Both of these steps are necessary to functionally activate $MAPKKK^{Byr2}$ (Eq. 6).

Finally, the upstream pheromone pathway is downregulated in a negative feedback loop as discussed in a later section (1.1.7).

1.1.4 Ras1

In the *S. pombe* pheromone response, Ras1 is a central component as it both activates the transcriptional response via $MAPKKK^{Byr2}$, and the morphological response via Cdc42-GEF^{Scd1}. Both molecules form protein complexes that anchor pools of $Ras1^{GTP}$ (Chang et al., 1994; Tu et

783 al., 1997; Weston et al., 2013), thus we hypothesised that the two pathway branches might
784 affect each other by changing the amount of available, unbound $Ras1^{GTP}$. In other words,
785 $MAPK^{Spk1}$ and Cdc42 pathways compete with each other for unbound $Ras1^{GTP}$. As the model
786 focuses on the **pp**$MAPK^{Spk1}$ levels, but not on $Cdc42^{GTP}$ production / localisation, the Cdc42
787 branch (the process [L9]) is simply represented as a change in available $Ras1^{GTP}$ for $MAPKKK^{Byr2}$
788 in the model. This is further discussed in the section on the *Cdc42-GEF* ^{scd1}*Δ* mutant strain
789 (1.1.11).

790 In the wildtype model, $Ras1^{GDP}$ is activated by the PS unit and deactivated by a Ras-GAP. Both
791 reactions are described by mass action kinetics in (Eq. 4 and Eq. 5). For simplification of
792 parameters, see section (1.1.8).

793

794 *Eq. 4*

795 $$\frac{d(Ras1^{GTP})}{dt} = k_2 \cdot PS \cdot Ras1^{GDP} - k_2 \cdot Ras1^{GTP}$$

796 *Eq. 5*

797 $$Ras1^{GTP} + Ras1^{GDP} = \text{constant}$$

798

799 1.1.5 $MAPKKK^{Byr2}$ and $MAPKK^{Byr1}$

800 Following the PS unit and $Ras1^{GDP}$ activation, $MAPKKK^{Byr2}$ is activated by a twofold mechanism
801 involving Ste4 (a component in the PS unit) and $Ras1^{GTP}$. Note, that $MAPK^{Spk1}$ is the only
802 member of the kinase cascade whose transcription is regulated by Ste11 (the process [L2])
803 (Mata and Bahler, 2006). Therefore, accordingly, the expression levels of $MAPKKK^{Byr2}$ and
804 $MAPKK^{Byr1}$ were not subject to Ste11 activity in our model. Compared to the 24hrs time scale of
805 pheromone signaling, the $MAPKKK^{Byr2}$ -> $MAPKK^{Byr1}$ activation likely happens on a much faster
806 time scale. Therefore, and for simplicity, we grouped $MAPKKK^{Byr2}$ and $MAPKK^{Byr1}$ into one unit
807 (Fig. 7A). Thus, $MAPKK^{Byr1}$ activation (phosphorylation) (the process [L5]) is given as in (Eq. 6 and
808 *Eq. 7*) and both activation and deactivation follows mass action kinetics. For simplification of
809 parameters, see section (1.1.8).

Eq. 6

$$\frac{d(pp\mathrm{MAPKK}^{\mathrm{Byr1}})}{dt} = (k_4 \cdot \mathrm{MAPKK}^{\mathrm{Byr1}} \cdot Ras1^{GTP} \cdot PS) - k_4 \cdot pp\mathrm{MAPKK}^{\mathrm{Byr1}}$$

Eq. 7

$$\boldsymbol{pp}\mathrm{MAPKK}^{\mathrm{Byr1}} activity = \boldsymbol{pp}\mathrm{MAPKK}^{\mathrm{Byr1}} \cdot k_6$$

Eq. 8

$$MAPKK^{\mathrm{Byr1}} + \boldsymbol{pp}MAPKK^{\mathrm{Byr1}} = \mathrm{constant}$$

1.1.6 MAPK^{Spk1}

In the cells, MAPK^{Spk1} protein expression is induced upon nitrogen removal (the process [L2] in Fig. 7A). MAPK^{Spk1} is then phosphorylated and activated to **pp**MAPK^{Spk1} by **pp**MAPKK^{Byr1} (the process [L6]). Experimentally we observed very similar dynamics for MAPK^{Spk1} and **pp**MAPK^{Spk1}. Therefore, we assumed that MAPK^{Spk1} ~ **pp**MAPK^{Spk1} system is in equilibrium, so creation and destruction reactions for each state can be disregarded. Thus, for simplicity, MAPK^{Spk1} is only present in its phosphorylated form (**pp**MAPK^{Spk1}) in the model.

Despite the simplification, the model represents the three main processes contributing to **pp**MAPK^{Spk1} levels: it is created proportionally to starvation and to MAPKK^{Byr1} activity (F_1, *Eq. 3*); it is also self-induced (which is again proportional to MAPKK^{Byr1} activity (F_6, *Eq. 7-Eq. 9*); and it is degraded by mass action kinetics (*Eq. 11*).

1.1.6.1 Positive Feedback

Previous studies have shown that **pp**MAPK^{Spk1} activates Ste11 (Kjaerulff et al., 2005), which in turn transcribes more *mapk^{spk1}*. This forms a positive feedback loop (the process [L7]) if **pp**MAPKK^{Byr1} is present to phosphorylate MAPK^{Spk1}. A simplest form of an abstract positive feedback is given as the self-dependence term $\mathbf{pp}\mathrm{MAPK}^{\mathrm{Spk1}^{k_9}}$ in Eq. 9.

836 *Eq. 9*

837 $$F_6 = \boldsymbol{pp}\mathrm{MAPKK}^{\mathrm{Byr1}} activity \cdot S \cdot \mathbf{pp}\mathrm{MAPK}^{\mathrm{Spk1}^{k_9}}; k_9 \geq 0$$

838

839 *Eq. 10*

840 $$v_{creation}\left(\mathbf{pp}\mathrm{MAPK}^{\mathrm{Spk1}}\right) = F_1 + F_6$$

841 F1 is described in (*Eq. 3*).

842

843 Finally, MAPK^{Spk1} is set to be degraded following simple mass action kinetic, thus the final
844 equation for ppMAPK^{Spk1} kinetics in wild type yeast is given as (Eq. 11).

845 *Eq. 11*

846 $$\frac{d(\mathbf{pp}\mathrm{MAPK}^{\mathrm{Spk1}})}{dt} = v_{creation}\left(\mathbf{pp}\mathrm{MAPK}^{\mathrm{Spk1}}\right) - \mathbf{pp}\mathrm{MAPK}^{\mathrm{Spk1}} \cdot k_7$$

847

848 1.1.7 Down regulation of the pathway by a negative feedback loop

849 Transient MAPK^{Spk1} activation in the wildtype cells (Fig.1C) suggests that there is a delayed
850 negative feedback to downregulate the **pp**MAPK^{Spk1} in the pathway, which leaves only a certain
851 time-window for activity. As this downregulation was found abolished in the constitutively
852 active *MAPKK$^{byr1.DD}$* mutant (Fig. 1E), the target(s) of the negative feedback must be MAPKK^{Byr1}
853 or upstream components. Hence, potential negative regulators, such as phosphatases Pyp1 and
854 Pmp1 that are proposed to directly deactivate ppMAPK^{Spk1} (Didmon et al., 2002), were excluded
855 from our model. Meanwhile, the negative regulators Sxa2 (encoding a serine carboxypeptidase
856 against a mating pheromone P-factor) and Rgs1 (encoding a regulator of Gpa1), both of which
857 are transcriptionally induced upon pheromone signalling, fit well to the criteria of a negative
858 feedback component (Imai and Yamamoto, 1992; Mata and Bahler, 2006; Pereira and Jones,
859 2001; Watson et al., 1999). Receptor internalization is also expected to be a part of the negative
860 feedback (Hirota et al., 2001) and regulation by antisense RNA for the *mapk^{spk1}* transcript as well
861 as other signalling components may also play a role (Bitton et al., 2011). As relative
862 contributions of each remain to be quantified, we represented all these potential negative
863 feedbacks collectively as a single circuit in our model that inactivates the PS unit (the process

[L8]) (Fig 7A). The chemical equation is therefore given as: $Ras1^{GTP} + ppMAPK^{Spk1} + PS \rightarrow Ras1^{GTP} + ppMAPK^{Spk1}$, which gives rise to the negative term in Eq. 12.

Eq. 12

$$\frac{d(PS)}{dt} = S \cdot k_0 - (k_8 \cdot \mathbf{pp}\mathrm{MAPK}^{\mathrm{Spk1}} \cdot PS \cdot Ras1^{GTP})$$

1.1.7.1 Ras1^{GTP} contribution to the negative feedback

Transient, peaking ppMAPK^{Spk1} activation in wildtype solely requires a delayed negative feedback. However, as described in the main text, a more complex regulation is necessary to describe the both earlier and lower peak in *ras1.G17V* and *cdc42-GEF$^{Scd1}\Delta$* mutants. By incorporating Ras1^{GTP} in this feedback (the process [L10], see: Eq. 12), we could precisely recapitulate both phenotypes.

1.1.7.2 The "simple-activator-Ras" model variant

We wanted to show the behaviour of the model if Ras1^{GTP} would only act as an activator. From the wild type model presented in Fig.7 we removed Ras1^{GTP} from the downregulation resulting in (Eq. 13).

Eq. 13

$$\frac{d(PS)}{dt} = S \cdot k_0 - (k_8 \cdot \mathbf{pp}\mathrm{MAPK}^{\mathrm{Spk1}} \cdot PS)$$

We fitted this model variant to the data sets as before, using Hooke–Jeeves (Hooke and Jeeves, 1961) and particle swarm optimisation methods (Kennedy and Eberhart, 1995). The objective value for the best fit was ~3 higher for this model variant than for the original model. Although it recapitulated the main features (Fig.S7B), it could not describe the observed “earlier and lower” signalling phenotype observed in the *ras1.G17V* and *cdc42-GEF$^{Scd1}\Delta$* strains. Finally, we also show that the addition of Ras1^{GTP} to this model only leads to increased amplitude, not to earlier timing (Fig.S7C).

890

891 1.1.8 Model simplification

892 After extensive parameter estimations, we found that the model can be simplified in the
893 number of individual parameters for forward and reverse reaction of the same species without
894 compromising the quality of fit. For the $Ras1^{GDP}$ ←→ $Ras1^{GTP}$ and $MAPKK^{Byr1}$ ←→$ppMAPKK^{Byr1}$
895 reactions we could set the forward and reverse parameters to the same value, and achieve
896 virtually identical quality fits, while reducing the number of free dimensions in the parameter
897 space by two. With this simplification the remaining model parameters became uniquely
898 identifiable, with the exception of k1 (Fig.S6). We also fitted the models with these as free
899 parameters and achieved very similar fit qualities, but most parameters became unidentifiable,
900 therefore, we decided for the simpler model.

901

902 **Mutant strains**

903 1.1.9 $MAPKK^{byr1.DD}$

904 $MAPKK^{Byr1.DD}$ harbors two phosphomimetic point mutations, which keep $MAPKK^{Byr1.DD}$ active
905 even in the absence of its activator $MAPKKK^{Byr2}$ (Fig. 3). Therefore, this mutation effectively
906 uncouples $MAPK^{Spk1}$ from the upstream part of the pathway, as represented in Fig. 7A,
907 *$MAPK^{byr1.DD}$* panel. In this mutant, $MAPK^{Spk1}$ (its substrate) also becomes constitutively
908 phosphorylated and activated (Fig. 1E).

909 It is known that the phosphomimetic substitution of the amino acids often does not fully
910 "mimic" the phosphorylated status and often fails to bring a full activation of the modified
911 kinase. This is likely happening to the $MAPKK^{Byr1.DD}$ mutant molecule: the initial production of
912 **pp**$MAPK^{Spk1}$ upon nitrogen starvation was much slower in the *$MAPKK^{byr1.DD}$* mutant than in
913 wildtype (Fig. 1E). This effect is represented by the f_{Byr1DD} <1 fitted parameter in the $MAPK^{Byr1.DD}$
914 model variant (see: Eq. 14).

915 *Eq. 14*

916 $$\boldsymbol{pp}\mathrm{MAPKK}^{\mathrm{Byr1}}activity = \boldsymbol{pp}\mathrm{MAPKK}^{\mathrm{Byr1}} \cdot k_6 \cdot f_{Byr1DD}$$

917

As MAPK^{Byr1} is not induced upon starvation (Nadin-Davis and Nasim, 1990), in the mutant strain, we could implement the mutation by setting initial concentrations $[Byr1]_0 = 0$ and $[Byr1^{PP}]_0 = 1$; and setting the respective activation and inactivation reactions to zero.

1.1.10 ras1.G17V

The *ras1.G17V* strain contains a point mutation, equivalent to human Ras G12V oncogenic mutation, which impairs the GTPase activity of the molecule (Trahey and McCormick, 1987). This results in being most of the molecules to stay in the Ras1^{GTP} form.

In the model, the following changes are implemented to represent the mutation: The initial concentration of $[Ras1^{GTP}]_0$ is set to 1, while that of $[Ras1^{GDP}]_0$ is set to 0, which is the opposite of the wildtype initial state. Also, the deactivation and activation reactions are set to zero.

1.1.11 Cdc42-GEF^{scd1}Δ

Ras1^{GTP} is proposed to interact with and activate Cdc42-GEF^{Scd1}, which then activates Cdc42 by acting as a GDP-GTP exchange factor (GEF) (Chang et al., 1994). Because Cdc42-GEF^{Scd1} binds Ras1, the loss of it leads to an increased pool of unbound Ras1^{GTP}. In our model this mutation is implemented as additional, unbound Ras1^{GTP} added to the wildtype system. In this setting the amount of Ras1^{GTP} available for MAPKKK^{Byr2} determines the **pp**MAPK^{Spk1} dynamics. Since it is unknown, how much Ras1^{GTP} is bound by Cdc42-GEF^{Scd1}, we fit the $[Ras1^{GTP}]_0$ as a free parameter in the otherwise intact, wild type model.

1.1.12 Implementation and availability

The **pp**MAPK^{Spk1} temporal dynamics in the four strains, wildtype, *MAPKK$^{byr1.DD}$*, *ras1.G17V* and *cdc42-GEF^{Scd1}Δ*, were described by 6 ODEs and 8 parameters shared across all species (List of Differential Equations, Supplementary Table S2). *MAPK$^{byr1.DD}$* has an additional parameter, f_{Byr1DD}, while $[Ras1^{GTP}]_0$ is fitted the *Cdc42-GEF^{scd1}Δ* strain as described above. The model represents relative concentrations of proteins on an absolute time scale. Initial concentrations of components are therefore either set to 1, if the component is present prior to starvation, or 0, if the component is not present, and it is induced or activated during starvation or

948 pheromone response. To show that the model is at steady state before nitrogen removal, it was
949 simulated for 100 hours prior to starvation in every case. All variables remained constant during
950 this time. All other plots start from T=t-100 as origin, when nitrogen is removed.

951 Model simulation and parameter estimation (model fitting) was performed in COPASI 4.20
952 (Hoops et al., 2006). Visualisation and data analysis was done in python v2.7 and R v3.2. Plotting
953 was performed by base R graphics and by the MarkdownReports v2.9.5 (Vertesy, 2017),
954 pheatmap (Kolde, 2013) and plotly v4.7.1 (Sievert et al., 2017) packages.

955

956 1.1.13 Parameter Estimation

957 Parameter estimation consisted in fitting of 8 rate constants (parameters) and one additional
958 parameter per mutant strain. We used the gradient-free Hooke–Jeeves (Hooke and Jeeves,
959 1961) and particle swarm optimisation methods (Kennedy and Eberhart, 1995) implemented in
960 COPASI.

961 We found that the algorithm converges better to the optimal solution, if key time points in the
962 dataset are counted with different weights for optimisation. Therefore, data points 102 (early
963 activation), 108 and 109 (peak) were passed on with triple weight to the optimisation function.

964

965 *1.1.13.1 Parameter identifiability, multiplex parameter estimation and ensemble*
966 *modelling*

967 To investigate parameter identifiability, we performed multiplexed parameter estimation by
968 5000 parallelised particle swarm optimisation. In each of the estimation rounds, the model was
969 fitted to the data, starting from randomised parameters. Parameters were sampled uniformly
970 +/- 4 orders of magnitudes around the previously achieved best fit, except the exponent (N).
971 This is the exponent of the positive feedback loop, is therefore an 'explosive' parameter, and
972 there is no reason to assume a stronger dependence than 4-th order (x^4) for **pp**MAPK^{Spk1} in the
973 positive feedback. The range for this parameter was therefore set to [1e-5, 4].

974 We repeated the estimations with +/- 5 magnitudes (5000 times), but we achieved no better fit,
975 while the convergence of optimisation dramatically decreased (i.e. >90% of the optimisations
976 did not get close to the optimal fit).

977 We found that with increasing fit quality (lower objective value) all parameters except k_1
978 converge to a single value, or a very limited range (Fig.S6D, top row, objective value <5).

979 In Fig.S7A, we further show the convergence on linear scale for an extended number of
980 simulations (objective value <8). The convergence of parameters is even more pronounced. In
981 suboptimal fits (O.V. >>3.6) $[Ras1^{GTP}]_0$ in the *scd1Δ* strain frequently hits the upper boundary,
982 which marks a 10-fold increase in available $Ras1^{GTP}$. Although the boundary is arbitrary, it is
983 unreasonable to think that there will be a bigger increase to the available $Ras1^{GTP}$ pool by the
984 knockout of *scd1*.

985 Multiplexed parameter estimation for the simple-Ras model performed in the same manner as
986 for the wildtype, 1000 fits with particle swarm optimisation from randomly sampled starting
987 points from a parameter space +/- 4 magnitudes around the best previous fit.

988

989 *1.1.13.2 Ensemble modelling*

990 To show the reliability of the model dynamics in spite of the un-identifiability of certain
991 parameters, we applied ensemble modelling (Brannmark et al., 2010). In this approach, we
992 analysed the predicted time courses of the 100 best fitting models to show that regardless of
993 the residual parameter uncertainty, the simulated variables' dynamics are robustly predicted
994 (Fig. S8). To show the variation of the individual simulation, ten thousand randomly sampled
995 simulation points are displayed behind the running average.

996

997 1.1.14 List of Differential Equations

998 As introduced above, here listed and separately defined for all species. Equations 4b and 6b are
999 only listed here, and provided for completeness: they are simply the reverse reactions for 4 and
1000 6 respectively, thus not discussed in the section above.

1001

1002 *Eq. 1*

1003 $$\frac{d(PS)}{dt} = S \cdot k_0 - v_{downregulation}(PS)$$

1004 *Eq. 4*

$$\frac{d(Ras1^{GTP})}{dt} = k_2 \cdot PS \cdot Ras1^{GDP} - k_2 \cdot Ras1^{GTP}$$

Eq. 4b

$$\frac{d(Ras1^{GDP})}{dt} = k_2 \cdot Ras1^{GTP} - k_2 \cdot PS \cdot Ras1^{GDP}$$

Eq. 6

$$\frac{d(pp\mathrm{MAPKK}^{\mathrm{Byr1}})}{dt} = (k_4 \cdot \mathrm{MAPKK}^{\mathrm{Byr1}} \cdot Ras1^{GTP} \cdot PS) - k_4 \cdot pp\mathrm{MAPKK}^{\mathrm{Byr1}}$$

Eq. 6b

$$\frac{d(\mathrm{MAPKK}^{\mathrm{Byr1}})}{dt} = k_4 \cdot pp\mathrm{MAPKK}^{\mathrm{Byr1}} - (k_4 \cdot \mathrm{MAPKK}^{\mathrm{Byr1}} \cdot Ras1^{GTP} \cdot PS)$$

Eq. 11

$$\frac{d(\mathbf{pp}\mathrm{MAPK}^{\mathrm{Spk1}})}{dt} = v_{creation}\left(\mathbf{pp}\mathrm{MAPK}^{\mathrm{Spk1}}\right) - \mathbf{pp}\mathrm{MAPK}^{\mathrm{Spk1}} \cdot k_7$$

1.1.15 List of Algebraic Equations

(All introduced above)

Eq. 7

$$\boldsymbol{pp}\mathrm{MAPKK}^{\mathrm{Byr1}}activity = \boldsymbol{pp}\mathrm{MAPKK}^{\mathrm{Byr1}} \cdot k_6$$

Eq. 3

$$F_1 = S \cdot k_1 \cdot \boldsymbol{pp}\mathrm{MAPKK}^{\mathrm{Byr1}}activity$$

Eq. 9

$$F_6 = \boldsymbol{pp}\mathrm{MAPKK}^{\mathrm{Byr1}}activity \cdot S \cdot \mathbf{pp}\mathrm{MAPK}^{\mathrm{Spk1}^{k_9}}; k_9 \geq 0$$

Eq. 10

$$\boldsymbol{v_{creation}}\left(\boldsymbol{ppMAPK^{Spk1}}\right) = \boldsymbol{F_1} + \boldsymbol{F_6}$$

Eq. 2

$$v_{downregulation}(PS) = k_8 \cdot \mathbf{pp}\mathrm{MAPK}^{\mathrm{Spk1}} \cdot PS$$

1028 *Eq. 5*

1029 $$Ras1^{GTP} + Ras1^{GDP} = 1$$

1030

1031 *Eq. 8*

1032 $$MAPKK^{\mathrm{Byr1}} + \boldsymbol{pp}MAPKK^{\mathrm{Byr1}} = 1$$

1033

1034 1.1.16 Availability

1035 Upon acceptance, the source code for analysis is available "as-is" under GNU GPLv3 at
1036 https://github.com/vertesy/Competition.Model.of.Ras.in.Pombe.Pheromone.Response. The
1037 model file will be provided at https://www.ebi.ac.uk/biomodels-main/ in SBML "Level 3: Version
1038 1" format exported from COPASI. The recommended COPASI format model file will be available
1039 at the GitHub repository.

1040

1041 **Acknowledgment**

1042 The authors thank Tatsuya Maeda, Thibault Mayor, Janni Petersen, Louise Fairall, John Schwabe,
1043 David Critchley, Andrey Reviyakin, Gary Willars and Mohan Harihar for helpful suggestions,
1044 stimulating discussions and critical reading of the manuscript. We thank PROTEX and PNACL at
1045 University of Leicester for their technical assistance. We are grateful to Kazu Shiozaki, Keith Gull
1046 and Yeast Genetic Resource Center for providing strains and antibodies. This work was funded
1047 by the Wellcome Trust Institutional Strategic Support Fund WT097828/Z/11/Z,
1048 WT097828/Z/11/B and the Deutsche Forschungsgemeinschaft (DFG) EXC 81. A.V. was supported
1049 by German Academic Exchange Service (DAAD) A0981674.

1050

1051 **Author Contributions**

1052 E.J.K., S.R. and K.T. generated yeast strains. E.J.K., G.S. and K.T. monitored activation status of
1053 $MAPK^{Spk1}$ and Cdc42. A.V. and E.K. conducted mathematical modelling. E.J.K., K.S. and K.T.
1054 conducted image analysis. M.T., R.G., C.P. and C.D. conducted biochemical analysis of Ras1, Byr2
1055 and Scd1. E.J.K., A.V., E.K. and K.T. designed the experiments and interpreted the data.

1056

1057 **Declaration of Interests**

1058 The authors declare no competing interests.

1059

1060 **References**

1061 Atay, O., and Skotheim, J.M. (2017). Spatial and temporal signal processing and decision making
1062 by MAPK pathways. J Cell Biol *216*, 317-330.
1063 Bahler, J., Wu, J.Q., Longtine, M.S., Shah, N.G., McKenzie, A., 3rd, Steever, A.B., Wach, A.,
1064 Philippsen, P., and Pringle, J.R. (1998). Heterologous modules for efficient and versatile PCR-
1065 based gene targeting in Schizosaccharomyces pombe. Yeast *14*, 943-951.
1066 Barr, M.M., Tu, H., Van Aelst, L., and Wigler, M. (1996). Identification of Ste4 as a potential
1067 regulator of Byr2 in the sexual response pathway of Schizosaccharomyces pombe. Mol Cell Biol
1068 *16*, 5597-5603.
1069 Bendezu, F.O., and Martin, S.G. (2013). Cdc42 explores the cell periphery for mate selection in
1070 fission yeast. Current biology : CB *23*, 42-47.
1071 Bitton, D.A., Grallert, A., Scutt, P.J., Yates, T., Li, Y., Bradford, J.R., Hey, Y., Pepper, S.D., Hagan,
1072 I.M., and Miller, C.J. (2011). Programmed fluctuations in sense/antisense transcript ratios drive
1073 sexual differentiation in S. pombe. Mol Syst Biol *7*, 559.
1074 Brannmark, C., Palmer, R., Glad, S.T., Cedersund, G., and Stralfors, P. (2010). Mass and
1075 information feedbacks through receptor endocytosis govern insulin signaling as revealed using a
1076 parameter-free modeling framework. J Biol Chem *285*, 20171-20179.
1077 Brummer, T., Naegele, H., Reth, M., and Misawa, Y. (2003). Identification of novel ERK-mediated
1078 feedback phosphorylation sites at the C-terminus of B-Raf. Oncogene *22*, 8823-8834.
1079 Chang, E.C., Barr, M., Wang, Y., Jung, V., Xu, H.P., and Wigler, M.H. (1994). Cooperative
1080 interaction of S. pombe proteins required for mating and morphogenesis. Cell *79*, 131-141.
1081 Chen, R.E., Patterson, J.C., Goupil, L.S., and Thorner, J. (2010). Dynamic localization of Fus3
1082 mitogen-activated protein kinase is necessary to evoke appropriate responses and avoid
1083 cytotoxic effects. Mol Cell Biol *30*, 4293-4307.
1084 Cox, A.D., and Der, C.J. (2010). Ras history: The saga continues. Small GTPases *1*, 2-27.
1085 Das, M., Wiley, D.J., Medina, S., Vincent, H.A., Larrea, M., Oriolo, A., and Verde, F. (2007).
1086 Regulation of cell diameter, For3p localization, and cell symmetry by fission yeast Rho-GAP
1087 Rga4p. Molecular biology of the cell *18*, 2090-2101.
1088 Didmon, M., Davis, K., Watson, P., Ladds, G., Broad, P., and Davey, J. (2002). Identifying
1089 regulators of pheromone signalling in the fission yeast Schizosaccharomyces pombe. Current
1090 genetics *41*, 241-253.
1091 Dougherty, M.K., Muller, J., Ritt, D.A., Zhou, M., Zhou, X.Z., Copeland, T.D., Conrads, T.P.,
1092 Veenstra, T.D., Lu, K.P., and Morrison, D.K. (2005). Regulation of Raf-1 by direct feedback
1093 phosphorylation. Mol Cell *17*, 215-224.
1094 Dudin, O., Merlini, L., and Martin, S.G. (2016). Spatial focalization of pheromone/MAPK signaling
1095 triggers commitment to cell-cell fusion. Genes Dev *30*, 2226-2239.
1096 Egel, R., ed. (2004). The Molecular Biology of Schizosaccharomyces pombe (Berlin Springer-
1097 Verlag).
1098 Endo, M., Shirouzu, M., and Yokoyama, S. (2003). The Cdc42 binding and scaffolding activities of
1099 the fission yeast adaptor protein Scd2. J Biol Chem *278*, 843-852.
1100 Fleissner, A., Leeder, A.C., Roca, M.G., Read, N.D., and Glass, N.L. (2009). Oscillatory recruitment
1101 of signaling proteins to cell tips promotes coordinated behavior during cell fusion. Proceedings
1102 of the National Academy of Sciences of the United States of America *106*, 19387-19392.
1103 Fukui, Y., Kozasa, T., Kaziro, Y., Takeda, T., and Yamamoto, M. (1986). Role of a ras homolog in
1104 the life cycle of Schizosaccharomyces pombe. Cell *44*, 329-336.

1105 Fukui, Y., Miyake, S., Satoh, M., and Yamamoto, M. (1989). Characterization of the
1106 Schizosaccharomyces pombe ral2 gene implicated in activation of the ras1 gene product. Mol
1107 Cell Biol *9*, 5617-5622.
1108 Funaya, C., Samarasinghe, S., Pruggnaller, S., Ohta, M., Connolly, Y., Muller, J., Murakami, H.,
1109 Grallert, A., Yamamoto, M., Smith, D.*, et al.* (2012). Transient structure associated with the
1110 spindle pole body directs meiotic microtubule reorganization in S. pombe. Current biology : CB
1111 *22*, 562-574.
1112 Gronwald, W., Huber, F., Grunewald, P., Sporner, M., Wohlgemuth, S., Herrmann, C., and
1113 Kalbitzer, H.R. (2001). Solution structure of the Ras binding domain of the protein kinase Byr2
1114 from Schizosaccharomyces pombe. Structure *9*, 1029-1041.
1115 Hegemann, B., Unger, M., Lee, S.S., Stoffel-Studer, I., van den Heuvel, J., Pelet, S., Koeppl, H.,
1116 and Peter, M. (2015). A Cellular System for Spatial Signal Decoding in Chemical Gradients. Dev
1117 Cell *35*, 458-470.
1118 Hirota, K., Tanaka, K., Watanabe, Y., and Yamamoto, M. (2001). Functional analysis of the C-
1119 terminal cytoplasmic region of the M-factor receptor in fission yeast. Genes Cells *6*, 201-214.
1120 Hooke, R., and Jeeves, T.A. (1961). 'Direct Search' Solution of Numerical and Statistical
1121 Problems. J ACM *8*, 212-229.
1122 Hoops, S., Sahle, S., Gauges, R., Lee, C., Pahle, J., Simus, N., Singhal, M., Xu, L., Mendes, P., and
1123 Kummer, U. (2006). COPASI--a COmplex PAthway SImulator. Bioinformatics *22*, 3067-3074.
1124 Hughes, D.A., Fukui, Y., and Yamamoto, M. (1990). Homologous activators of ras in fission and
1125 budding yeast. Nature *344*, 355-357.
1126 Hughes, D.A., Yabana, N., and Yamamoto, M. (1994). Transcriptional regulation of a Ras
1127 nucleotide-exchange factor gene by extracellular signals in fission yeast. J Cell Sci *107 (Pt 12)*,
1128 3635-3642.
1129 Imai, Y., and Yamamoto, M. (1992). Schizosaccharomyces pombe sxa1+ and sxa2+ encode
1130 putative proteases involved in the mating response. Mol Cell Biol *12*, 1827-1834.
1131 Kelly, F.D., and Nurse, P. (2011). Spatial control of Cdc42 activation determines cell width in
1132 fission yeast. Molecular biology of the cell *22*, 3801-3811.
1133 Kennedy, J., and Eberhart, R. (1995). Particle swarm optimization. 1995 Ieee International
1134 Conference on Neural Networks Proceedings, Vols 1-6, 1942-1948.
1135 Kjaerulff, S., Andersen, N.R., Borup, M.T., and Nielsen, O. (2007). Cdk phosphorylation of the
1136 Ste11 transcription factor constrains differentiation-specific transcription to G1. Genes Dev *21*,
1137 347-359.
1138 Kjaerulff, S., Lautrup-Larsen, I., Truelsen, S., Pedersen, M., and Nielsen, O. (2005). Constitutive
1139 activation of the fission yeast pheromone-responsive pathway induces ectopic meiosis and
1140 reveals ste11 as a mitogen-activated protein kinase target. Mol Cell Biol *25*, 2045-2059.
1141 Kolde, R. (2013). Pheatmap: Pretty Heatmaps. http://cranr-projectorg/package=pheatmap.
1142 Laemmli, U.K. (1970). Cleavage of structural proteins during the assembly of the head of
1143 bacteriophage T4. Nature *227*, 680-685.
1144 Lavoie, H., and Therrien, M. (2015). Regulation of RAF protein kinases in ERK signalling. Nat Rev
1145 Mol Cell Biol *16*, 281-298.
1146 Lin, A.W., Barradas, M., Stone, J.C., van Aelst, L., Serrano, M., and Lowe, S.W. (1998). Premature
1147 senescence involving p53 and p16 is activated in response to constitutive MEK/MAPK mitogenic
1148 signaling. Genes Dev *12*, 3008-3019.
1149 Maeder, C.I., Hink, M.A., Kinkhabwala, A., Mayr, R., Bastiaens, P.I., and Knop, M. (2007). Spatial
1150 regulation of Fus3 MAP kinase activity through a reaction-diffusion mechanism in yeast
1151 pheromone signalling. Nat Cell Biol *9*, 1319-1326.

1152 Malliri, A., van der Kammen, R.A., Clark, K., van der Valk, M., Michiels, F., and Collard, J.G.
1153 (2002). Mice deficient in the Rac activator Tiam1 are resistant to Ras-induced skin tumours.
1154 Nature *417*, 867-871.
1155 Marcus, S., Polverino, A., Chang, E., Robbins, D., Cobb, M.H., and Wigler, M.H. (1995). Shk1, a
1156 homolog of the Saccharomyces cerevisiae Ste20 and mammalian p65PAK protein kinases, is a
1157 component of a Ras/Cdc42 signaling module in the fission yeast Schizosaccharomyces pombe.
1158 Proceedings of the National Academy of Sciences of the United States of America *92*, 6180-
1159 6184.
1160 Masuda, T., Kariya, K., Shinkai, M., Okada, T., and Kataoka, T. (1995). Protein kinase Byr2 is a
1161 target of Ras1 in the fission yeast Schizosaccharomyces pombe. J Biol Chem *270*, 1979-1982.
1162 Mata, J., and Bahler, J. (2006). Global roles of Ste11p, cell type, and pheromone in the control of
1163 gene expression during early sexual differentiation in fission yeast. Proceedings of the National
1164 Academy of Sciences of the United States of America *103*, 15517-15522.
1165 Mata, J., Lyne, R., Burns, G., and Bahler, J. (2002). The transcriptional program of meiosis and
1166 sporulation in fission yeast. Nature genetics *32*, 143-147.
1167 Mata, J., Wilbrey, A., and Bahler, J. (2007). Transcriptional regulatory network for sexual
1168 differentiation in fission yeast. Genome biology *8*, R217.
1169 Matheos, D., Metodiev, M., Muller, E., Stone, D., and Rose, M.D. (2004). Pheromone-induced
1170 polarization is dependent on the Fus3p MAPK acting through the formin Bni1p. J Cell Biol *165*,
1171 99-109.
1172 McClure, A.W., Minakova, M., Dyer, J.M., Zyla, T.R., Elston, T.C., and Lew, D.J. (2015). Role of
1173 Polarized G Protein Signaling in Tracking Pheromone Gradients. Dev Cell *35*, 471-482.
1174 Merlini, L., Dudin, O., and Martin, S.G. (2013). Mate and fuse: how yeast cells do it. Open Biol *3*,
1175 130008.
1176 Merlini, L., Khalili, B., Bendezu, F.O., Hurwitz, D., Vincenzetti, V., Vavylonis, D., and Martin, S.G.
1177 (2016). Local Pheromone Release from Dynamic Polarity Sites Underlies Cell-Cell Pairing during
1178 Yeast Mating. Current biology : CB *26*, 1117-1125.
1179 Merlini, L., Khalili, B., Dudin, O., Michon, L., Vincenzetti, V., and Martin, S.G. (2018). Inhibition of
1180 Ras activity coordinates cell fusion with cell-cell contact during yeast mating. J Cell Biol *217*,
1181 1467-1483.
1182 Moreno, S., Klar, A., and Nurse, P. (1991). Molecular genetic analysis of fission yeast
1183 Schizosaccharomyces pombe. Methods Enzymol *194*, 795-823.
1184 Mutavchiev, D.R., Leda, M., and Sawin, K.E. (2016). Remodeling of the Fission Yeast Cdc42 Cell-
1185 Polarity Module via the Sty1 p38 Stress-Activated Protein Kinase Pathway. Current biology : CB
1186 *26*, 2921-2928.
1187 Nadin-Davis, S.A., and Nasim, A. (1988). A gene which encodes a predicted protein kinase can
1188 restore some functions of the ras gene in fission yeast. EMBO J *7*, 985-993.
1189 Nadin-Davis, S.A., and Nasim, A. (1990). Schizosaccharomyces pombe ras1 and byr1 are
1190 functionally related genes of the ste family that affect starvation-induced transcription of
1191 mating-type genes. Mol Cell Biol *10*, 549-560.
1192 Nadin-Davis, S.A., Nasim, A., and Beach, D. (1986a). Involvement of ras in sexual differentiation
1193 but not in growth control in fission yeast. EMBO J *5*, 2963-2971.
1194 Nadin-Davis, S.A., Yang, R.C., Narang, S.A., and Nasim, A. (1986b). The cloning and
1195 characterization of a RAS gene from Schizosaccharomyces pombe. J Mol Evol *23*, 41-51.
1196 Nern, A., and Arkowitz, R.A. (2000). Nucleocytoplasmic shuttling of the Cdc42p exchange factor
1197 Cdc24p. J Cell Biol *148*, 1115-1122.
1198 Obara, T., Nakafuku, M., Yamamoto, M., and Kaziro, Y. (1991). Isolation and characterization of
1199 a gene encoding a G-protein alpha subunit from Schizosaccharomyces pombe: involvement in

1200 mating and sporulation pathways. Proceedings of the National Academy of Sciences of the
1201 United States of America *88*, 5877-5881.
1202 Okazaki, N., Okazaki, K., Tanaka, K., and Okayama, H. (1991). The ste4+ gene, essential for sexual
1203 differentiation of Schizosaccharomyces pombe, encodes a protein with a leucine zipper motif.
1204 Nucleic acids research *19*, 7043-7047.
1205 Onken, B., Wiener, H., Philips, M.R., and Chang, E.C. (2006). Compartmentalized signaling of Ras
1206 in fission yeast. Proceedings of the National Academy of Sciences of the United States of
1207 America *103*, 9045-9050.
1208 Otsubo, Y., and Yamamoto, M. (2012). Signaling pathways for fission yeast sexual differentiation
1209 at a glance. J Cell Sci *125*, 2789-2793.
1210 Ottilie, S., Miller, P.J., Johnson, D.I., Creasy, C.L., Sells, M.A., Bagrodia, S., Forsburg, S.L., and
1211 Chernoff, J. (1995). Fission yeast pak1+ encodes a protein kinase that interacts with Cdc42p and
1212 is involved in the control of cell polarity and mating. EMBO J *14*, 5908-5919.
1213 Ozoe, F., Kurokawa, R., Kobayashi, Y., Jeong, H.T., Tanaka, K., Sen, K., Nakagawa, T., Matsuda, H.,
1214 and Kawamukai, M. (2002). The 14-3-3 proteins Rad24 and Rad25 negatively regulate Byr2 by
1215 affecting its localization in Schizosaccharomyces pombe. Mol Cell Biol *22*, 7105-7119.
1216 Papadaki, P., Pizon, V., Onken, B., and Chang, E.C. (2002). Two ras pathways in fission yeast are
1217 differentially regulated by two ras guanine nucleotide exchange factors. Mol Cell Biol *22*, 4598-
1218 4606.
1219 Pereira, P.S., and Jones, N.C. (2001). The RGS domain-containing fission yeast protein, Rgs1p,
1220 regulates pheromone signalling and is required for mating. Genes Cells *6*, 789-802.
1221 Prior, I.A., Lewis, P.D., and Mattos, C. (2012). A comprehensive survey of Ras mutations in
1222 cancer. Cancer Res *72*, 2457-2467.
1223 Qiu, R.G., Abo, A., McCormick, F., and Symons, M. (1997). Cdc42 regulates anchorage-
1224 independent growth and is necessary for Ras transformation. Mol Cell Biol *17*, 3449-3458.
1225 Ramachander, R., Kim, C.A., Phillips, M.L., Mackereth, C.D., Thanos, C.D., McIntosh, L.P., and
1226 Bowie, J.U. (2002). Oligomerization-dependent association of the SAM domains from
1227 Schizosaccharomyces pombe Byr2 and Ste4. J Biol Chem *277*, 39585-39593.
1228 Ramezani-Rad, M. (2003). The role of adaptor protein Ste50-dependent regulation of the
1229 MAPKKK Ste11 in multiple signalling pathways of yeast. Current genetics *43*, 161-170.
1230 Ritt, D.A., Monson, D.M., Specht, S.I., and Morrison, D.K. (2010). Impact of feedback
1231 phosphorylation and Raf heterodimerization on normal and mutant B-Raf signaling. Mol Cell
1232 Biol *30*, 806-819.
1233 Schindelin, J., Arganda-Carreras, I., Frise, E., Kaynig, V., Longair, M., Pietzsch, T., Preibisch, S.,
1234 Rueden, C., Saalfeld, S., Schmid, B.*, et al.* (2012). Fiji: an open-source platform for biological-
1235 image analysis. Nat Methods *9*, 676-682.
1236 Schubbert, S., Bollag, G., and Shannon, K. (2007). Deregulated Ras signaling in developmental
1237 disorders: new tricks for an old dog. Curr Opin Genet Dev *17*, 15-22.
1238 Shimada, Y., Gulli, M.-P., and Peter, M. (2000). Nuclear sequestration of the exchange factor
1239 Cdc24 by Far1 regulates cell polarity during yeast mating. Nature Cell Biology *2*, 117.
1240 Sievert, C., Parmer, C., Hocking, T., Chamberlain, S., Ram, K., Corvellec, M., Despouy, P., and Inc.,
1241 P.T. (2017). plotly: Create Interactive Web Graphics via 'plotly.js'. .
1242 Sipiczki, M. (1988). The role of sterility genes (ste and aff) in the initiation of sexual development
1243 in Schizosaccharomyces pombe. Molecular & general genetics : MGG *213*, 529-534.
1244 Stengel, K.R., and Zheng, Y. (2012). Essential role of Cdc42 in Ras-induced transformation
1245 revealed by gene targeting. PLoS One *7*, e37317.

1246 Sugimoto, A., Iino, Y., Maeda, T., Watanabe, Y., and Yamamoto, M. (1991). Schizosaccharomyces
1247 pombe ste11+ encodes a transcription factor with an HMG motif that is a critical regulator of
1248 sexual development. Genes Dev *5*, 1990-1999.
1249 Tatebe, H., Nakano, K., Maximo, R., and Shiozaki, K. (2008). Pom1 DYRK regulates localization of
1250 the Rga4 GAP to ensure bipolar activation of Cdc42 in fission yeast. Current biology : CB *18*, 322-
1251 330.
1252 Toda, T., Shimanuki, M., and Yanagida, M. (1991). Fission yeast genes that confer resistance to
1253 staurosporine encode an AP-1-like transcription factor and a protein kinase related to the
1254 mammalian ERK1/MAP2 and budding yeast FUS3 and KSS1 kinases. Genes Dev *5*, 60-73.
1255 Trahey, M., and McCormick, F. (1987). A cytoplasmic protein stimulates normal N-ras p21
1256 GTPase, but does not affect oncogenic mutants. Science *238*, 542-545.
1257 Tratner, I., FourticqEsqueoute, A., Tillit, J., and Baldacci, G. (1997). Cloning and characterization
1258 of the S-pombe gene efc25(+), a new putative guanine nucleotide exchange factor. Gene *193*,
1259 203-210.
1260 Tu, H., Barr, M., Dong, D.L., and Wigler, M. (1997). Multiple regulatory domains on the Byr2
1261 protein kinase. Mol Cell Biol *17*, 5876-5887.
1262 Tuveson, D.A., Shaw, A.T., Willis, N.A., Silver, D.P., Jackson, E.L., Chang, S., Mercer, K.L.,
1263 Grochow, R., Hock, H., Crowley, D.*, et al.* (2004). Endogenous oncogenic K-ras(G12D) stimulates
1264 proliferation and widespread neoplastic and developmental defects. Cancer Cell *5*, 375-387.
1265 van Drogen, F., Stucke, V.M., Jorritsma, G., and Peter, M. (2001). MAP kinase dynamics in
1266 response to pheromones in budding yeast. Nat Cell Biol *3*, 1051-1059.
1267 Verde, F., Mata, J., and Nurse, P. (1995). Fission yeast cell morphogenesis: identification of new
1268 genes and analysis of their role during the cell cycle. J Cell Biol *131*, 1529-1538.
1269 Vertesy, A. (2017). An R function library to create scientific figures and markdown reports easily.
1270 (Update v2.9.5.).
1271 Wach, A. (1996). PCR-synthesis of marker cassettes with long flanking homology regions for
1272 gene disruptions in S. cerevisiae. Yeast *12*, 259-265.
1273 Wang, Y., Xu, H.P., Riggs, M., Rodgers, L., and Wigler, M. (1991). byr2, a Schizosaccharomyces
1274 pombe gene encoding a protein kinase capable of partial suppression of the ras1 mutant
1275 phenotype. Mol Cell Biol *11*, 3554-3563.
1276 Watson, P., Davis, K., Didmon, M., Broad, P., and Davey, J. (1999). An RGS protein regulates the
1277 pheromone response in the fission yeast Schizosaccharomyces pombe. Mol Microbiol *33*, 623-
1278 634.
1279 Weston, C., Bond, M., Croft, W., and Ladds, G. (2013). The coordination of cell growth during
1280 fission yeast mating requires Ras1-GTP hydrolysis. PLoS One *8*, e77487.
1281 Xu, H.P., White, M., Marcus, S., and Wigler, M. (1994). Concerted action of RAS and G proteins
1282 in the sexual response pathways of Schizosaccharomyces pombe. Mol Cell Biol *14*, 50-58.
1283 Xue-Franzen, Y., Kjaerulff, S., Holmberg, C., Wright, A., and Nielsen, O. (2006). Genomewide
1284 identification of pheromone-targeted transcription in fission yeast. BMC Genomics *7*, 303.
1285 Yamamoto, M. (1996). The molecular control mechanisms of meiosis in fission yeast. Trends
1286 Biochem Sci *21*, 18-22.
1287 Zheng, C.F., and Guan, K.L. (1994). Activation of MEK family kinases requires phosphorylation of
1288 two conserved Ser/Thr residues. EMBO J *13*, 1123-1131.
1289 Zhu, J., Woods, D., McMahon, M., and Bishop, J.M. (1998). Senescence of human fibroblasts
1290 induced by oncogenic Raf. Genes Dev *12*, 2997-3007.
1291

1292

1293 ## Figure legends

1294 **Figure 1. Distinct modes of MAPK^{Spk1} temporal phosphorylation profile and morphological**
1295 **changes during sexual differentiation in wildtype, *MAPKK$^{byr1.DD}$* and *ras1.G17V* mutants.**

1296 (A) A pictorial representation of wildtype fission yeast sexual differentiation. (B) A list of key
1297 signalling components of the fission yeast pheromone signalling pathway. The diagram reflects
1298 the prediction that Gpa1 and Ras1 separately contribute to activation of MAPKKK^{Byr2} activation
1299 although the precise mechanism is unknown (Xu et al., 1994). At the same time, Ras1 activation
1300 is expected to be at least partly under influence of active Gpa1 because the *ste6* gene, encoding
1301 a Ras1 activator, is strongly induced upon successful pheromone signaling (Hughes et al., 1994).
1302 (C)-(H) Cells were induced for sexual differentiation by the plate mating assay system as
1303 described in the materials and methods. (C), (E) and (G) Quantified **pp**MAPK^{Spk1} signal from
1304 western blots of wildtype (KT3082) (C), *MAPKK$^{byr1.DD}$* (KT3435) (E) and *ras1.G17V* (KT3084) (G)
1305 cells. Three biological replicates were used for quantitation (error bars are ±SEM). α-tubulin was
1306 used as a loading control and quantitation was carried out using the Image Studio ver2.1
1307 software (Licor Odyssey CLx Scanner). For the wildtype samples in (C), the % of cells mating is
1308 also indicated (n=400, three biological replicates). The wildtype **pp**MAPK^{Spk1} result (C) is also
1309 presented in (E) and (G) as a reference. (D), (F) and (H) Cellular morphology (brightfield) and
1310 localization of MAPK^{Spk1}-GFP over a 24 hour time-course in wildtype (D), *MAPKK$^{byr1.DD}$* (F) and
1311 *ras1.G17V* (H) cells. Time after induction of mating in hours is indicated on the left. At each time
1312 point, a bright-field image and a GFP signal image were taken and processed as described in
1313 materials and methods. Green asterisks in the time 24 h in the *ras1.G17V* cell image (H) indicate
1314 auto-fluorescence signal from inviable cell debris, which were produced through cytokinesis
1315 failure or cell lysis. Yellow arrows in panels (D) and (F) indicate transient accumulation of
1316 MAPK^{Spk1}-GFP at the shmoo tips. Scale bars represent 10µm.

1317

1318 **Figure 2. In the *ras1.G17V MAPKK$^{byr1.DD}$* double mutant, the MAPK^{Spk1} phosphorylation profile**
1319 **follows *MAPKK$^{byr1.DD}$* single mutant phenotype whilst cell morphology mimics the *ras1.G17V***
1320 **single mutant phenotype.**

1321 (A) MAPK^{Spk1} phosphorylation status in the *ras1.G17V MAPKK$^{byr1.DD}$* double mutant cells
1322 (KT3439). Cells were induced for mating by the plate mating assay system as described in the
1323 materials and methods. Quantitated **pp**MAPK^{Spk1} signal (arbitrary unit) from western blots is

1324 presented. Results of two biological replicates (each derived from three technical replicates,
1325 error bars are ±SEM) are presented in red. (B) The terminal mating phenotype of *ras1.G17V*
1326 *MAPKK*$^{byr1.DD}$ double mutant is a phenocopy of *ras1.G17V* single mutant which shows the
1327 "elongated" morphology. Images were taken of *ras1.G17V MAPKK*$^{byr1.DD}$ double mutant
1328 (KT3439) in the same way as in Fig. 1. Time after induction of mating in hours is indicated on the
1329 left. (C) There is no morphological change in the absence of MAPK^{Spk1} signalling. Cell images of
1330 *MAPKK*^{byr1}*Δ* (KT4700) and *ras1.G17V MAPKK*^{byr1}*Δ* (KT5030) strains are shown. Images were
1331 taken in the same way as in Fig. 1. Time after induction of mating in hours is indicated on the
1332 left of each series. Scale bars represent 10µm.

1333

1334 **Figure 3. Ras1 activates both MAPK^{Spk1} and Cdc42 pathways during pheromone signalling.**

1335 (A) *scd1Δ* morphology and MAPK^{Spk1}-GFP signal. Images of WT (KT3082), *scd1Δ* (KT4061) and
1336 *scd1Δ ras1.G17V* double mutant (KT4056) were taken in the same way as in Fig.1. Numbers on
1337 the left represents hours after induction of mating. (B) MAPK^{Spk1} phosphorylation state in *scd1Δ*
1338 (KT4061) cells after mating induction. Results of three biological replicates (error bars are ±SEM)
1339 are presented. The wildtype **pp**MAPK^{Spk1} result presented in Fig.1 (C) is also shown in blue as a
1340 reference. (C) Cell images of *scd1Δ MAPKK*$^{byr1.DD}$ double mutant (KT4047) were taken in the
1341 same way as in Fig.1. Numbers on the left represents hours after induction of mating. (D)
1342 MAPK^{Spk1} phosphorylation state in *ras1Δ* (KT4323), *MAPKK*$^{byr1.DD}$ (KT3435) and *ras1Δ*
1343 *MAPKK*$^{byr1.DD}$ (KT4359) cell extracts. Original Western blotting data is presented in Fig. S4A. (E)
1344 MAPK^{Spk1} phosphorylation state in *mapkkk*^{byr2}*Δ* (KT3763), *MAPKK*$^{byr1.DD}$ (KT3435) and
1345 *mapkkk*^{byr2}*Δ MAPKK*$^{byr1.DD}$ (KT4010) cell extracts. Original Western blotting data is presented in
1346 Fig. S4B. For (D) and (E), quantification was carried out using the Image Studio ver2.1 (Li-cor). (F)
1347 Cell images of the strains mentioned in (D) and (E) were taken in the same way as in Fig.1.
1348 Numbers on the left represents hours after induction of mating. For all the images presented in
1349 (A), (C) and (F), scale bars represent 10µm.

1350

1351 **Figure 4. Ras1.G17V induces cortical Cdc42^{GTP} accumulation**

1352 (A) Cell morphology and localisation of Cdc42^{GTP}, indicated by CRIB-GFP signal, during the sexual
1353 differentiation process. Wildtype (KT5077) and *ras1.G17V* (KT5082) mutant cells were induced
1354 for mating/sexual differentiation by the plate mating assay condition (Materials and Methods)

1355 and live cell images were taken at the indicated time after induction of mating/sexual
1356 differentiation. Representative CRIB-GFP signal images are presented. Cells with cortical CRIB-
1357 GFP foci are indicated by orange stars. Rapidly-disappearing CRIB-GFP signals at the fusion site
1358 of wildtype mating cells are indicated by green arrows at time 8.5h image. Scale bar: 10 µm. (B)
1359 Quantitation of the results presented in (A). At each time point (4.5h, 6.5h, 10.5h, 12.5h and
1360 22.5h after induction of mating/sexual differentiation), 150 cells were examined whether they
1361 have cortical CRIB-GFP foci. % cells with cortical CRIB-GFP foci is presented. The experiment was
1362 repeated for three times and the mean values and SDs are plotted in the graph. (C) Cell
1363 morphology and localisation of $Cdc42^{GTP}$, indicated by CRIB-GFP signal, during vegetative
1364 growth. Representative CRIB-GFP signal images of cells of wildtype (KT5077), *ras1Δ* (5107),
1365 *ras1.G17V* (KT5082), *rga4Δ* (5551) and *rga4Δ ras1.G17V* (KT5554) are presented. Scale bar: 10
1366 µm. (D) Quantitated CRIB-GFP signals on the cell cortex of cells presented in (C). Intensity of GFP
1367 signal on the cell cortex was measured along one of the cell tips as indicated as a magenta
1368 dotted line in the example image on the right (Scale bar: 10 µm) as stated in the Materials and
1369 Methods. 40 cells without septum were measured for each strain and the average curve from all
1370 aligned traces per strain was calculated, and displayed with respective standard error of the
1371 mean curves (dashed lines) as described in Materials and Methods.

1372

1373 **Fig. 5. Distinct contributions of Ste4 and Ste6 to $MAPK^{Spk1}$ phosphorylation.**

1374 (A) Ste4 is essential for $MAPK^{Spk1}$ activation. $MAPK^{Spk1}$ phosphorylation status in *ste4Δ* (KT4376),
1375 *ste4Δ ras1.G17V* (KT5143) and *ste4Δ* $MAPKK^{byr1.DD}$ (KT5136) at times-points 0, 8 ,16 and 24
1376 hours post mating induction are presented. Original Western blotting membranes are presented
1377 in Fig. S4C. (B) Incapability of *ste4Δ* to cause pheromone-induced morphological change is
1378 suppressed by $MAPKK^{byr1.DD}$ but not by *ras1.G17V*. Cell images of *ste4Δ* (KT4376), *ste4Δ*
1379 *ras1.G17V* (KT5143) and *ste4Δ* $MAPKK^{byr1.DD}$ (KT5136) strains were taken 24 hours after
1380 induction of mating. Scale bar: 10 µm. (C) Lack of Ste6 does not result in the complete loss of
1381 $MAPK^{Spk1}$ phosphorylation. $MAPK^{Spk1}$ phosphorylation status in *ste6Δ* (KT4333), *ste6Δ ras1.G17V*
1382 (KT4998) and *ste6Δ* $MAPKK^{byr1.DD}$ (KT5139) at times-points 0, 8 ,16 and 24 hours post mating
1383 induction are presented. Original Western blotting membranes are presented in Fig. S4D. (D)
1384 Incapability of *ste6Δ* to cause pheromone-induced morphological change is suppressed by
1385 *ras1.G17V* mutation but not by $MAPKK^{byr1.DD}$ mutation. Cell images of *ste6Δ* (KT4333), *ste6Δ*

1386 *ras1.G17V* (KT4998) and *ste6Δ MAPKK*$^{byr1.DD}$ (KT5139) strains were taken 24 hours after
1387 induction of mating. Scale bar: 10 µm.

1388

1389 **Fig. 6. Gpa1 transduces the pheromone signalling by activating MAPK^{Spk1} and Ras1 pathways**

1390 (A) MAPK^{Spk1} phosphorylation status in homothallic *gpa1Δ* (KT4335), *gpa1Δ ras1.G17V*
1391 (KT5023), *gpa1Δ MAPKK*$^{byr1.DD}$ (KT4353) and *gpa1Δ ras1.val17 MAPKK*$^{byr1.DD}$ (KT5035) at times-
1392 points 0, 8 ,12, 16 and 24 hours after mating induction. Original Western membrane is
1393 presented in Fig. S5A. (B) Cell images of the above mentioned strains at 16 hours after mating
1394 induction. All the cell images were taken and processed as in Figure 1. Scale bar is 10 µm. (C)
1395 MAPK^{Spk1} phosphorylation status in *h*$^{-}$ WT (KT4190), *h*$^{-}$ *gpa1.QL* (KT5059), *h*$^{-}$ *ras1.G17V* (KT4233),
1396 *h*$^{-}$ *gpa1.QL ras1Δ* (KT5070) and h^{-} *MAPKK*$^{byr1.DD}$ (KT4194) at times-points 0, 8 ,12 and 24 after
1397 mating induction. Note that while the activation induced in the *gpa1.QL* mutant was down-
1398 regulated, *MAPKK*$^{byr1.DD}$ induced a constitutive activation. Original Western membrane is
1399 presented in Fig. S5B. (D) Cell images of the above strains at 12 h after induction of mating. All
1400 the cell images were taken and processed as in Figure 1. Scale bar is 10 µm.

1401

1402 **Fig. 7. Mathematical modelling of the fission yeast pheromone pathway dynamics.**

1403 (A) Components and frameworks of the mathematical model in wildtype and signalling mutants:
1404 *ras1.G17V*, *Cdc42GEF*^{scd1}*Δ,* and *MAPKK*$^{byr1.DD}$. Changes corresponding to each mutant are
1405 indicated as follows: Grey: removed components or interactions, orange: increased level of
1406 activity. For the exact implementation of the mutants, see Materials and Method. The
1407 measured component, **pp**MAPK^{Spk1}, is highlighted in green. (B) Measured and simulated
1408 **pp**MAPK^{Spk1} activation profiles in wildtype, *ras1.G17V*, *Cdc42GEF*^{scd1}*Δ* and *MAPKK*$^{byr1.DD}$ mutants.
1409 Dashed lines: model simulations. Diamonds: experimental data presented in Fig. 1C, E, G, and
1410 Fig. 3B; error bars: SEM. (C) GTP-loaded Ras1.G17V (1-172) directly binds to Byr2 (65-180) and
1411 Scd1 (760-872). *In vitro* GST pull-down assays of bacterially expressed Ras1.G17V (1-172), GST-
1412 Byr2 (65-180) and GST-Scd1 (760-872) were conducted as described in materials and methods.
1413 GTP-loaded Ras1.G17V (1-172) was found to bind to both GST-Byr2 (65-180) and GST-Scd1 (760-
1414 872). (D) Two Ras1 effectors, Byr2 and Scd1, compete for GTP-loaded Ras1.G17V (1-172). In
1415 vitro GST pull-down assays of bacterially expressed Ras1.G17V (1-172) and GST-Byr2 (65-180)
1416 were conducted as in (A). Addition of Scd1 (760-872) fragment interfered with Ras1-Byr2

1417 binding (the 4th lane). Quantitated signal intensities of the Ras1.G17V (1-172) band in the gel are
1418 shown in the right panel. (E) Simulated ppMAPK^{Spk1} dynamics in the wildtype model at
1419 increasing concentrations of Ras1^{GTP} added *in silico* to the system. Increased Ras1^{GTP}
1420 concentration causes advanced and reduced **pp**MAPK^{Spk1} peak intensities. (F) The model fitted
1421 to the 4 strains (as above, in red) correctly predicts ppMAPK^{Spk1} dynamics in the additional 21
1422 signalling mutant strains (in light and dark green) measured in this study.

1423 **Fig. 8. Schematic diagram of the fission yeast pheromone signalling pathway**

1424 (A) Wildtype fission yeast pheromone signalling pathway, highlighting the branched pheromone
1425 sensing, and that both branches are necessary for mating. (B) Because of the robust regulatory
1426 mechanism implemented for the MAPK pathway and the competition between the effectors,
1427 the constitutively active Ras1.G17V mutation yields a biased overactivation of Cdc42.

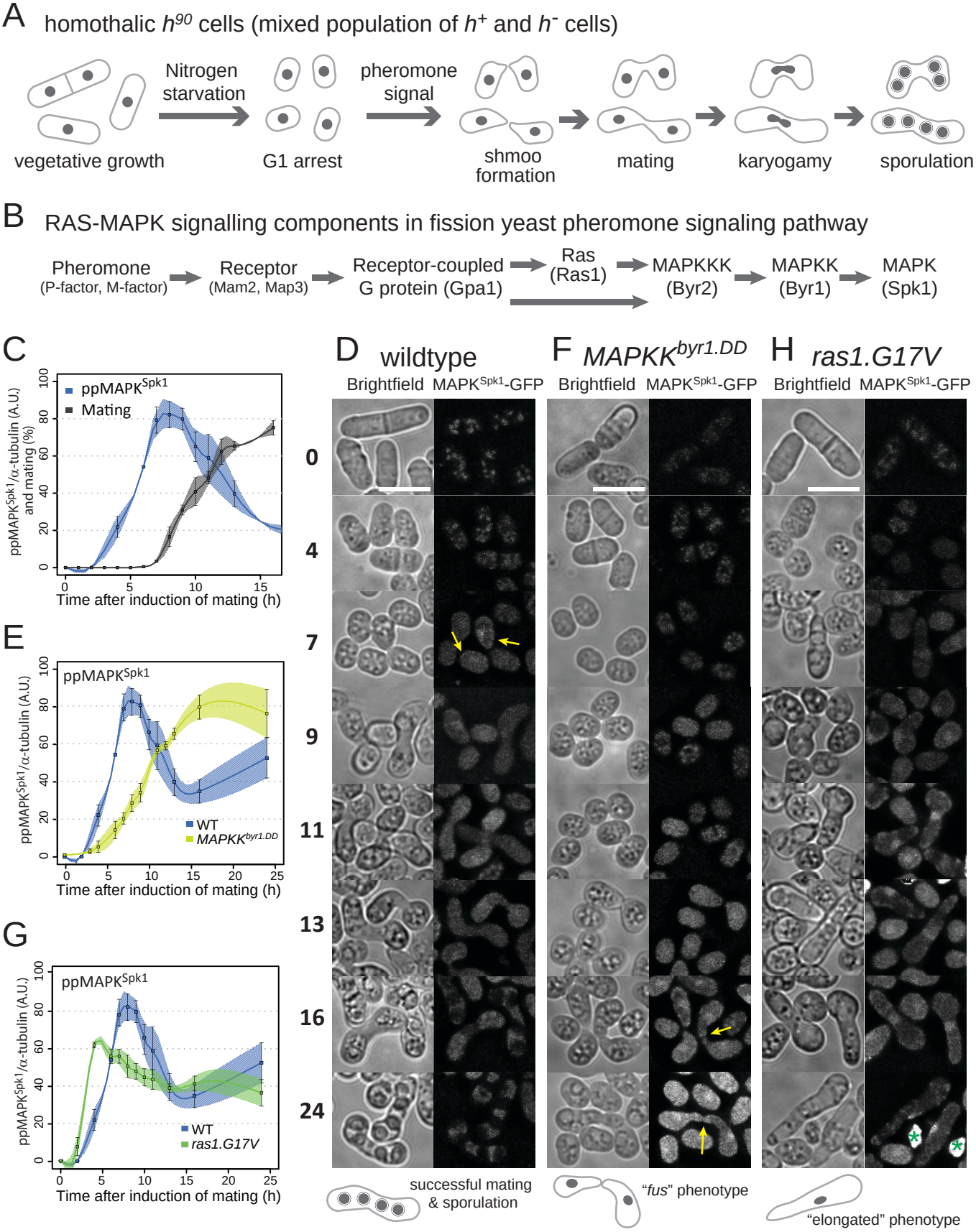

Figure 1. Distinct modes of MAPK^{Spk1} temporal phosphorylation profile and morphological changes during sexual differentiation in wildtype, *MAPKK$^{byr1.DD}$* and *ras1.G17V* mutants.

(A) A pictorial representation of wildtype fission yeast sexual differentiation. (B) A list of key signalling components of the fission yeast pheromone signalling pathway. The diagram reflects the prediction that Gpa1 and Ras1 separately contribute to activation of MAPKKK^{Byr2} activation although the precise mechanism is unknown (Xu et al., 1994). At the same time, Ras1 activation is expected to be at least partly under influence of active Gpa1 because the ste6 gene, encoding a Ras1 activator, is strongly induced upon successful pheromone signaling (Hughes et al., 1994). (C)-(H) Cells were induced for sexual differentiation by the plate mating assay system as described in the materials and methods. (C), (E) and (G) Quantified ppMAPK^{Spk1} signal from western blots of wildtype (KT3082) (C), *MAPKK$^{byr1.DD}$* (KT3435) (E) and *ras1.G17V* (KT3084) (G) cells. Three biological replicates were used for quantitation (error bars are ±SEM). α-tubulin was used as a loading control and quantitation was carried out using the Image Studio ver2.1 software (Licor Odyssey CLx Scanner). For the wildtype samples in (C), the % of cells mating is also indicated (n=400, three biological replicates). The wildtype ppMAPK^{Spk1} result (C) is also presented in (E) and (G) as a reference. (D), (F) and (H) Cellular morphology (brightfield) and localization of MAPK^{Spk1}-GFP over a 24 hour time-course in wildtype (D), *MAPKK$^{byr1.DD}$* (F) and *ras1.G17V* (H) cells. Time after induction of mating in hours is indicated on the left. At each time point, a bright-field image and a GFP signal image were taken and processed as described in materials and methods. Green asterisks in the time 24 h in the ras1.G17V cell image (H) indicate auto-fluorescence signal from inviable cell debris, which were produced through cytokinesis failure or cell lysis. Yellow arrows in panels (D) and (F) indicate transient accumulation of MAPK^{Spk1}-GFP at the shmoo tips. Scale bars represent 10μm.

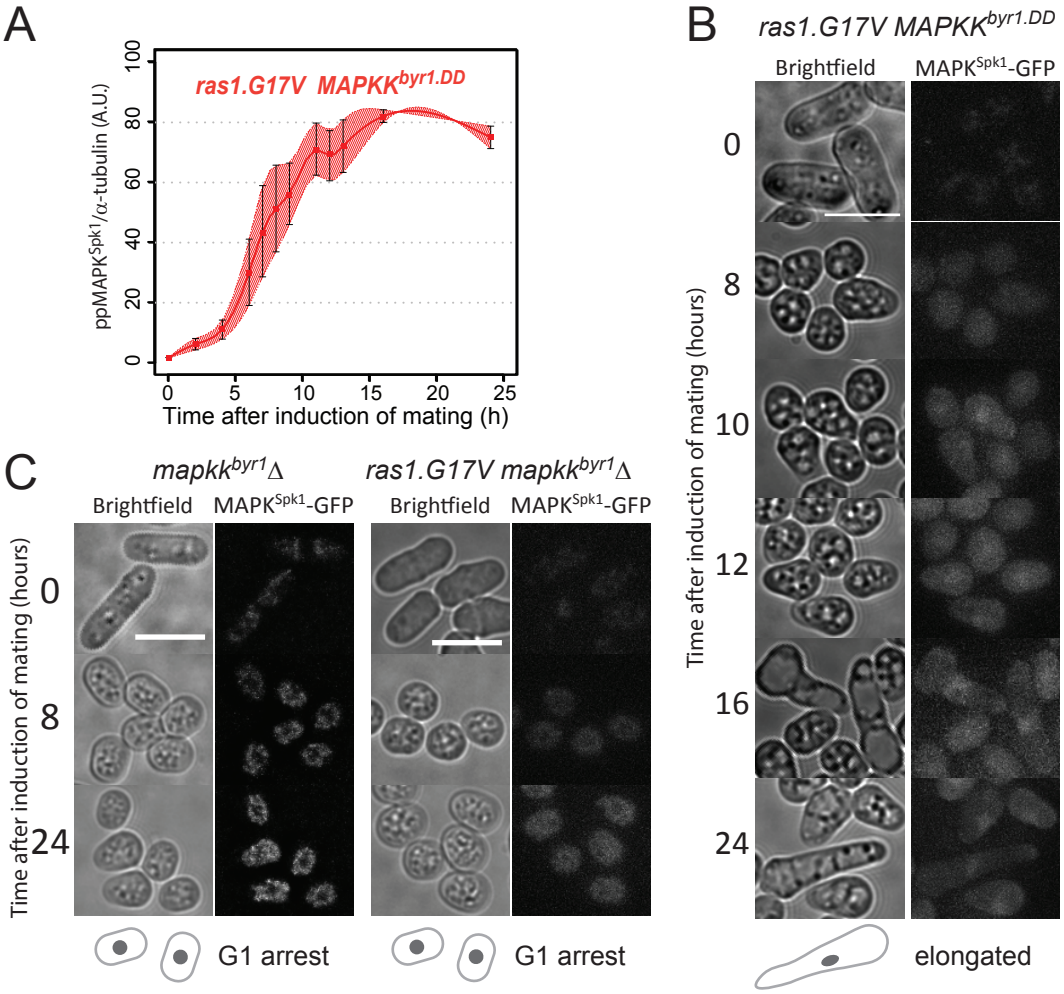

Figure 2. In the *ras1.G17V MAPKK*$^{byr1.DD}$ double mutant, the MAPK^{Spk1} phosphorylation profile follows *MAPKK*$^{byr1.DD}$ single mutant phenotype whilst cell morphology mimics the *ras1.G17V* single mutant phenotype.

(A) MAPK^{Spk1} phosphorylation status in the *ras1.G17V MAPKK*$^{byr1.DD}$ double mutant cells (KT3439). Cells were induced for mating by the plate mating assay system as described in the materials and methods. Quantitated **pp**MAPK^{Spk1} signal (arbitrary unit) from western blots is presented. Results of two biological replicates (each derived from three technical replicates, error bars are ±SEM) are presented in red. (B) The terminal mating phenotype of *ras1.G17V MAPKK*$^{byr1.DD}$ double mutant is a phenocopy of *ras1.G17V* single mutant which shows the "elongated" morphology. Images were taken of *ras1.G17V MAPKK*$^{byr1.DD}$ double mutant (KT3439) in the same way as in Fig. 1. Time after induction of mating in hours is indicated on the left. (C) There is no morphological change in the absence of MAPK^{Spk1} signalling. Cell images of *MAPKK*^{byr1}*Δ* (KT4700) and *ras1.G17V MAPKK*$^{byr1.DD}$ (KT5030) strains are shown. Images were taken in the same way as in Fig. 1. Time after induction of mating in hours is indicated on the left of each series. Scale bars represent 10μm.

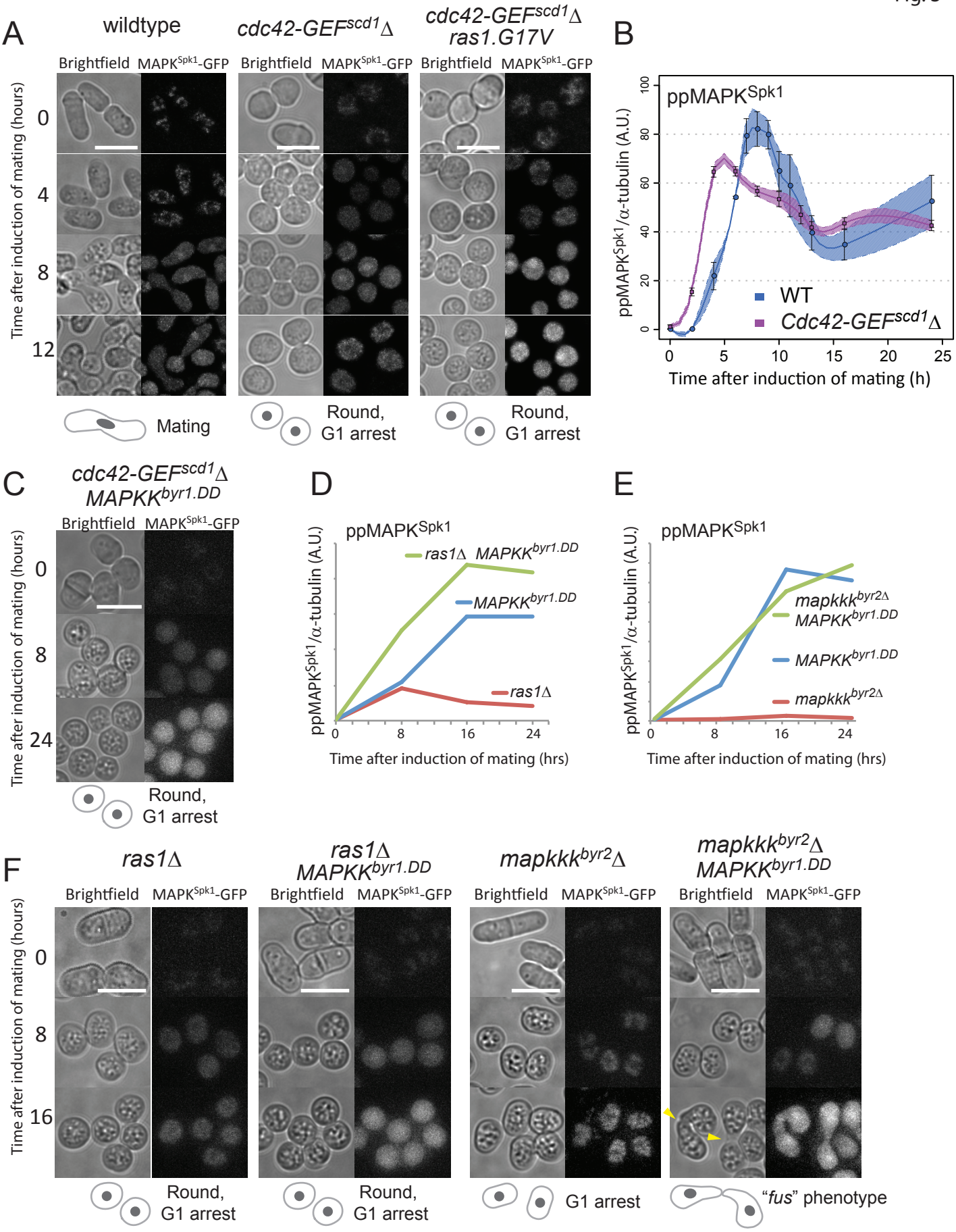

Figure 3. Ras1 activates both MAPK^{Spk1} and Cdc42 pathways during pheromone signalling.
(A) *scd1Δ* morphology and MAPK^{Spk1}-GFP signal. Images of WT (KT3082), *scd1Δ* (KT4061) and *scd1Δ ras1.G17V* double mutant (KT4056) were taken in the same way as in Fig.1. Numbers on the left represents hours after induction of mating. (B) MAPK^{Spk1} phosphorylation state in *scd1Δ* (KT4061) cells after mating induction. Results of three biological replicates (error bars are ±SEM) are presented. The wildtype result presented in Fig.1 (C) is also shown in blue as a reference. (C) Cell images of *scd1Δ MAPKK$^{byr1.DD}$* double mutant (KT4047) were taken in the same way as in Fig.1. Numbers on the left represents hours after induction of mating. (D) MAPK^{Spk1} phosphorylation state in *ras1Δ* (KT4323), *MAPKK$^{byr1.DD}$* (KT3435) and *scd1Δ MAPKK$^{byr1.DD}$* (KT4359) cell extracts. Original Western blotting data is presented in Fig. S3A. (E) MAPK^{Spk1} phosphorylation state in *mapkkk^{byr2}Δ* (KT3763), *MAPKK$^{byr1.DD}$* (KT3435) and *mapkkk^{byr2}Δ MAPKK$^{byr1.DD}$* (KT4010) cell extracts. Original Western blotting data is presented in Fig. S3B. For (D) and (E), quantification was carried out using the Image Studio ver2.1 (Li-cor). (F) Cell images of the strains mentioned in (D) and (E) were taken in the same way as in Fig.1. Numbers on the left represents hours after induction of mating. For all the images presented in (A), (C) and (F), scale bars represent 10μm.

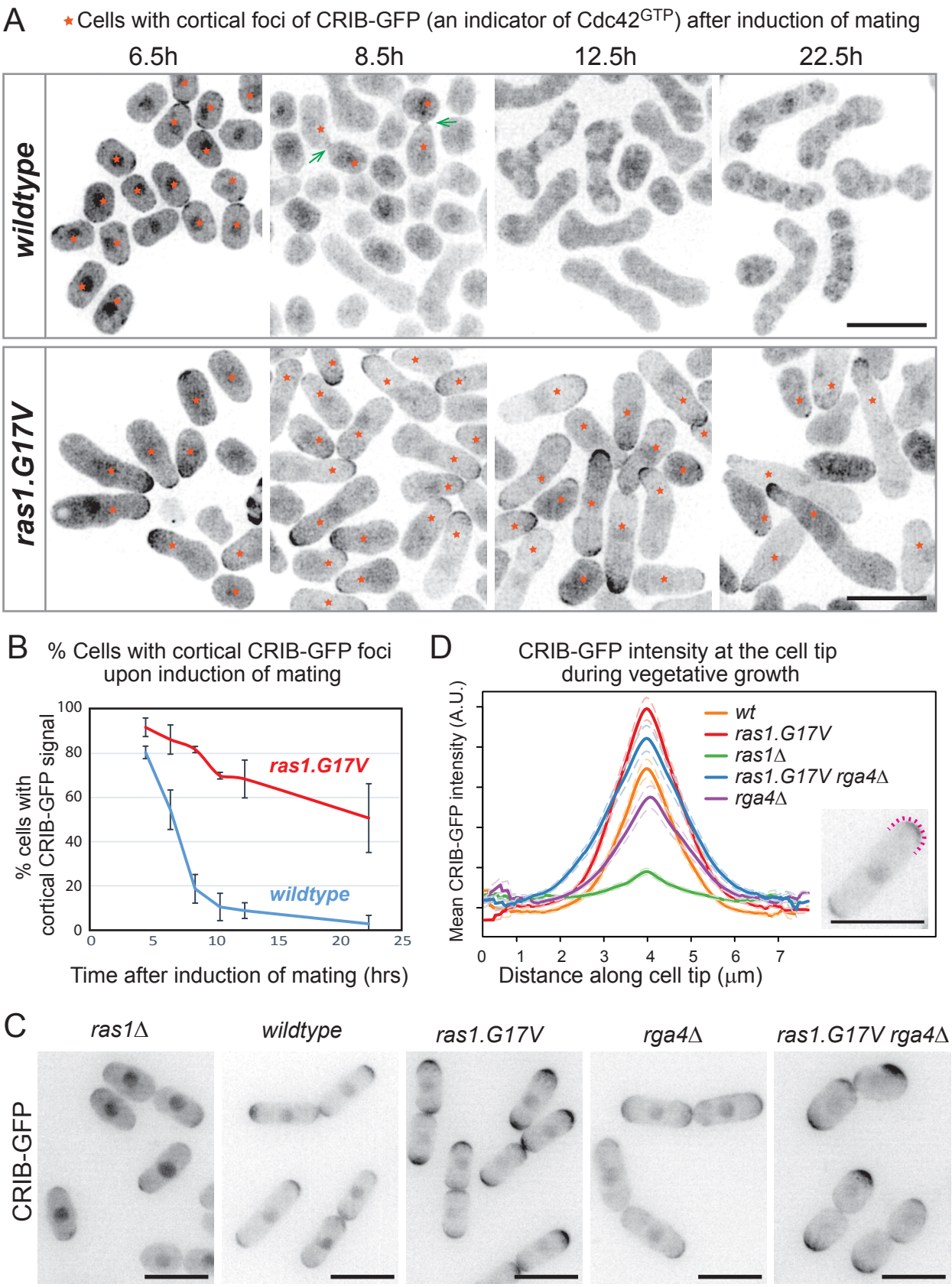

Figure 4. Ras1.G17V induces cortical Cdc42^{GTP} accumulation
(A) Cell morphology and localisation of Cdc42^{GTP}, indicated by CRIB-GFP signal, during the sexual differentiation process. Wildtype (KT5077) and *ras1.G17V* (KT5082) mutant cells were induced for sexual differentiation by the plate mating assay condition (Materials and Methods) and live cell images were taken at the indicated time after induction of mating/sexual differentiation. Representative CRIB-GFP signal images are presented. Cells with cortical CRIB-GFP foci are indicated by orange stars. Rapidly-disappearing CRIB-GFP signals at the fusion site of wildtype mating cells are indicated by green arrows at time 8.5h image. Scale bar: 10 μm. (B) Quantitation of the results presented in (A). At each time point (4.5h, 6.5h, 10.5h, 12.5h and 22.5h after induction of mating/sexual differentiation), 150 cells were examined whether they have cortical CRIB-GFP foci. % cells with cortical CRIB-GFP foci is presented. The experiment was repeated for three times and the mean values and SDs are plotted in the graph. (C) Cell morphology and localisation of Cdc42^{GTP}, indicated by CRIB-GFP signal, during vegetative growth. Representative CRIB-GFP signal images of cells of wildtype (KT5077), *ras1Δ* (5107), *ras1.G17V* (KT5082), *rga4Δ* (5551) and *rga4Δ ras1.G17V* (KT5554) are presented. Scale bar: 10 μm. (D) Quantitated CRIB-GFP signals on the cell cortex of cells presented in (C). Intensity of GFP signal on the cell cortex was measured along one of the cell tips as indicated as a magenta dotted line in the example image on the right (Scale bar: 10 μm) as stated in the Materials and Methods. 40 cells without septum were measured for each strain and the average curve from all aligned traces per strain was calculated, and displayed with respective standard error of the mean curves (dashed lines) as described in Materials and Methods.

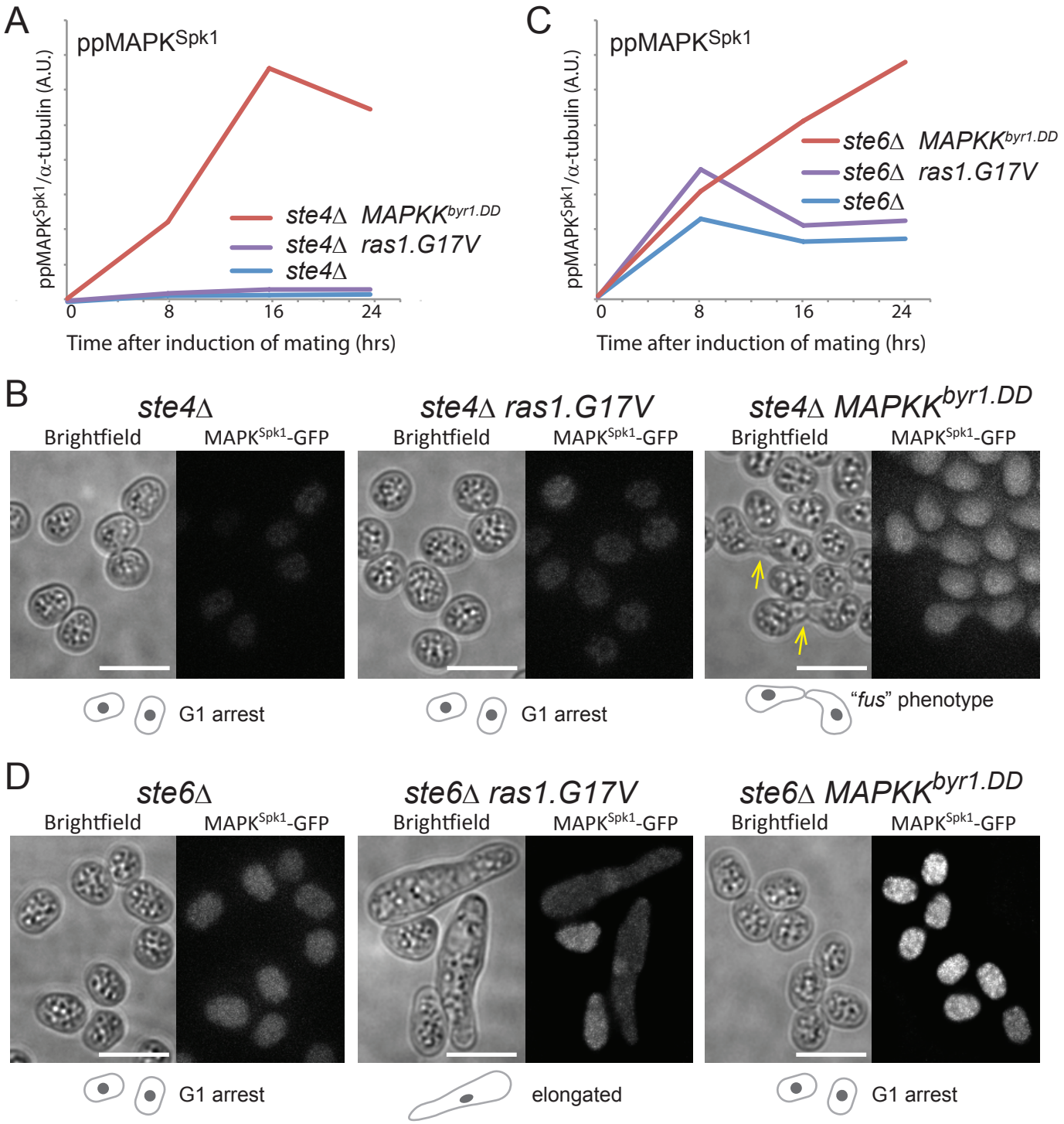

Fig. 5. Distinct contributions of Ste4 and Ste6 to MAPK^{Spk1} phosphorylation.
(A) Ste4 is essential for MAPK^{Spk1} activation. MAPK^{Spk1} phosphorylation status in *ste4Δ* (KT4376), *ste4Δ ras1.G17V* (KT5143) and *ste4Δ MAPKK$^{byr1.DD}$* (KT5136) at times-points 0, 8 ,16 and 24 hours post mating induction are presented. Original Western blotting membranes are presented in Fig. S3C. (B) Incapability of *ste4Δ* to cause pheromone-induced morphological change is suppressed by *MAPKK$^{byr1.DD}$* but not by *ras1.G17V*. Cell images of *ste4Δ* (KT4376), *ste4Δ ras1.G17V* (KT5143) and *ste4Δ MAPKK$^{byr1.DD}$* (KT5136) strains were taken 24 hours after induction of mating. Scale bar: 10 μm. (C) Lack of Ste6 does not result in the complete loss of MAPK^{Spk1} phosphorylation. MAPK^{Spk1} phosphorylation status in *ste6Δ* (KT4333), *ste6Δ ras1.G17V* (KT4998) and *ste6Δ MAPKK$^{byr1.DD}$* (KT5139) at times-points 0, 8 ,16 and 24 hours post mating induction are presented. Original Western blotting membranes are presented in Fig. S3D. (D) Incapability of *ste6Δ* to cause pheromone-induced morphological change is suppressed by *ras1.G17V* mutation but not by *MAPKK$^{byr1.DD}$* mutation. Cell images of *ste6Δ* (KT4333), *ste6Δ ras1.G17V* (KT4998) and *ste6Δ MAPKK$^{byr1.DD}$* (KT5139) strains were taken 24 hours after induction of mating. Scale bar: 10 μm.

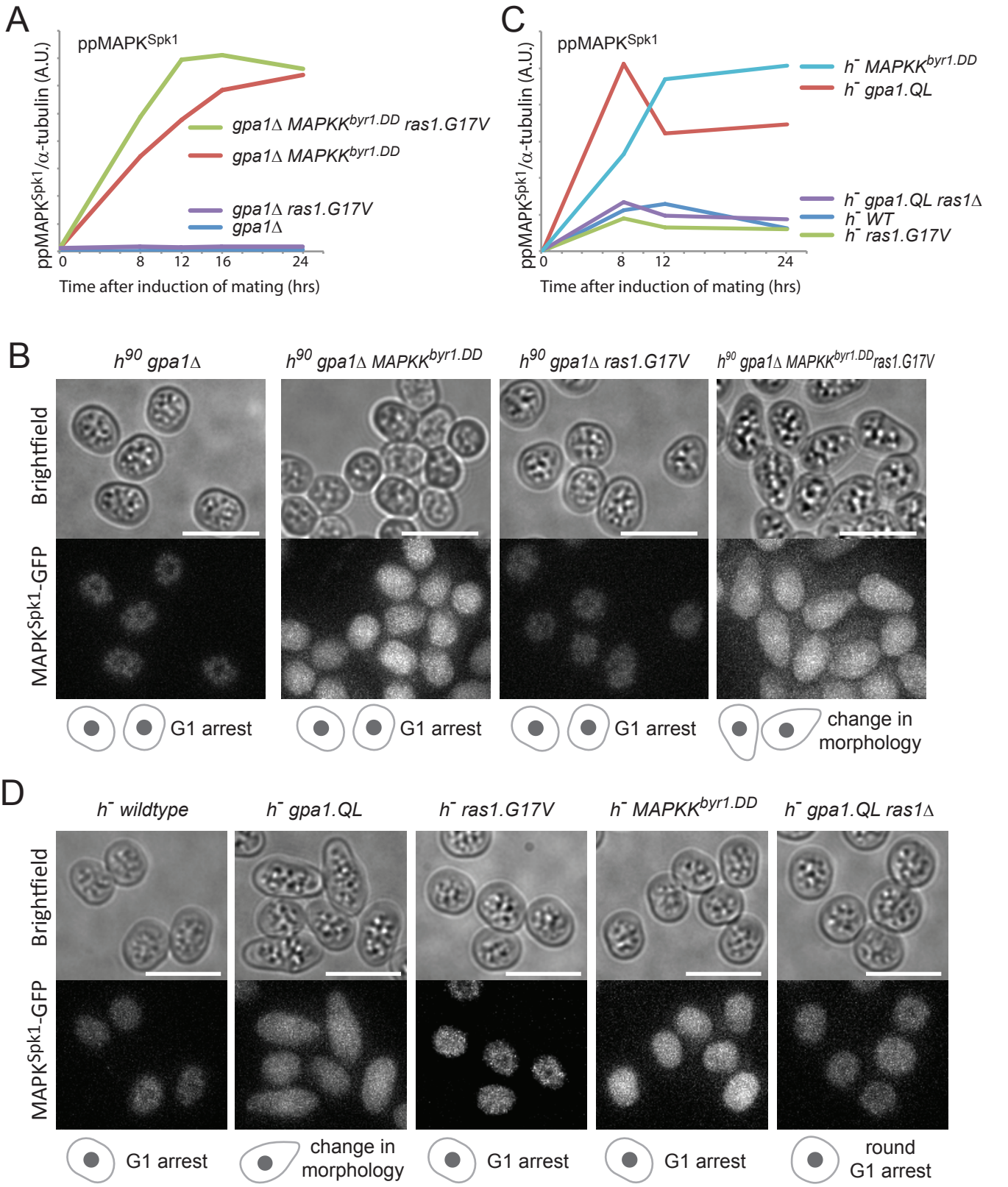

Fig. 6. Gpa1 transduces the pheromone signalling by activating MAPK^{Spk1} and Ras1 pathways.
(A) MAPK^{Spk1} phosphorylation status in homothallic *gpa1Δ* (KT4335), *gpa1Δ ras1.G17V* (KT5023), *gpa1Δ MAPKK$^{byr1.DD}$* (KT4353) and *gpa1Δ ras1.val17 MAPKK$^{byr1.DD}$* (KT5035) at times-points 0, 8 ,12, 16 and 24 hours after mating induction. Original Western membrane is presented in Fig. S4A. (B) Cell images of the above mentioned strains at 16 hours after mating induction. All the cell images were taken and processed as in Figure 1. Scale bar is 10 µm. (C) MAPK^{Spk1} phosphorylation status in *h⁻* WT (KT4190), *h⁻ gpa1.QL* (KT5059), *h⁻ ras1.G17V* (KT4233), *h⁻ gpa1.QL ras1Δ* (KT5070) and *h⁻ MAPKK$^{byr1.DD}$* (KT4194) at times-points 0, 8 ,12 and 24 after mating induction. Note that while the activation induced in the gpa1.QL mutant was down-regulated, *MAPKK$^{byr1.DD}$* induced a constitutive activation. Original Western membrane is presented in Fig. S4B. (D) Cell images of the above strains at 12 h after induction of mating. All the cell images were taken and processed as in Figure 1. Scale bar is 10 µm.

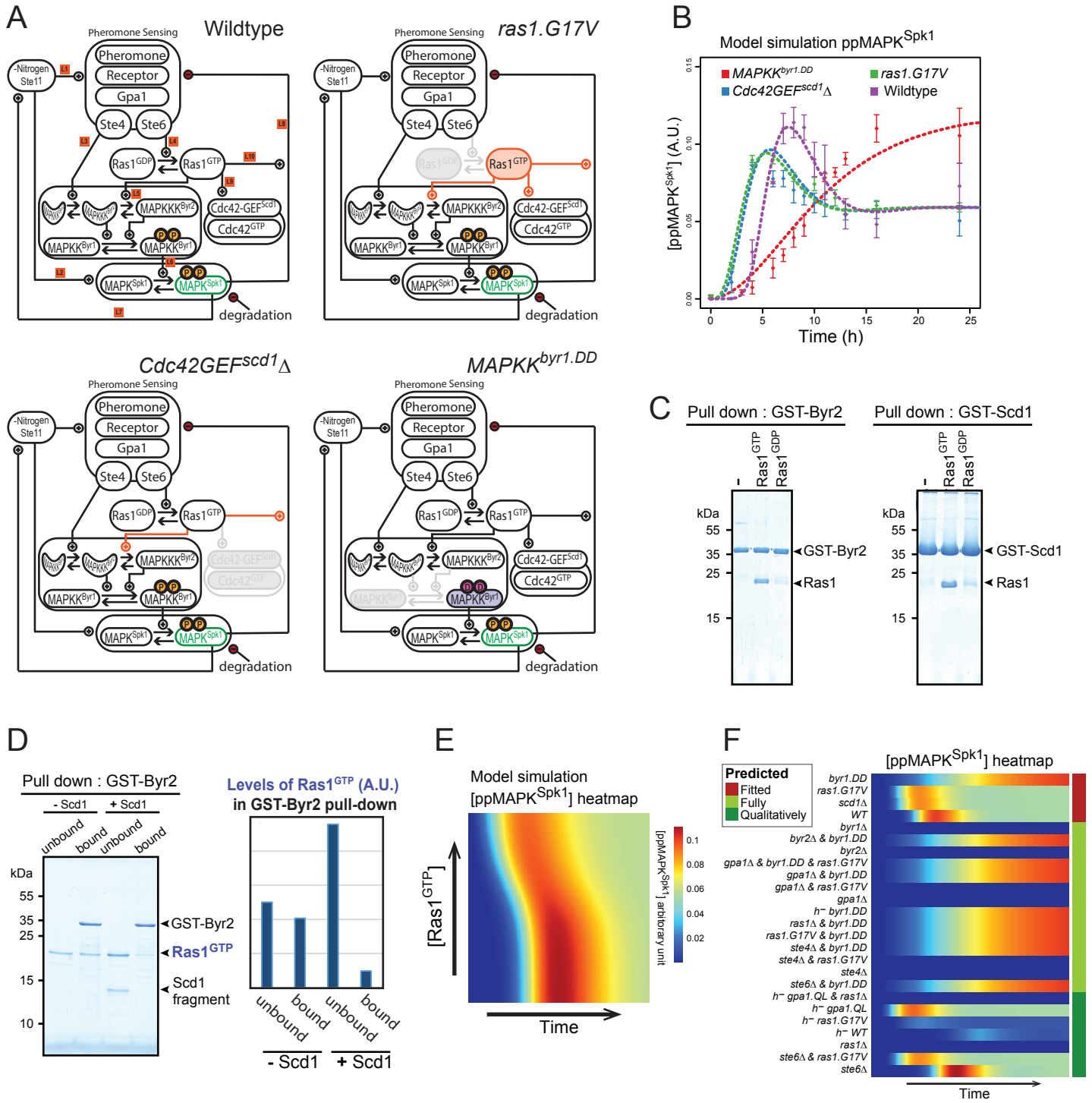

Fig. 7. Mathematical modelling of the fission yeast pheromone pathway dynamics.
(A) Components and frameworks of the mathematical model in wildtype and signalling mutants: *ras1.G17V, Cdc42GEF^{scd1}Δ*, and *MAPKK$^{byr1.DD}$*. Changes corresponding to each mutant are indicated as follows: Grey: removed components or interactions, orange: increased level of activity. For the exact implementation of the mutants, see Materials and Method. The measured component, **pp**MAPK^{Spk1}, is highlighted in green. (B) Measured and simulated **pp**MAPK^{Spk1} activation profiles in wildtype, *ras1.G17V, Cdc42GEF^{scd1}Δ* and *MAPKK$^{byr1.DD}$* mutants. Dashed lines: model simulations. Diamonds: experimental data presented in Fig. 1C, E, G, and Fig. 3B; error bars: SEM. (C) GTP-loaded Ras1.G17V (1-172) directly binds to Byr2 (65-180) and Scd1 (760-872). *In vitro* GST pull-down assays of bacterially expressed Ras1.G17V (1-172), GST-Byr2 (65-180) and GST-Scd1 (760-872) were conducted as described in materials and methods. GTP-loaded Ras1.G17V (1-172) was found to bind to both GST-Byr2 (65-180) and GST-Scd1 (760-872). (D) Two Ras1 effectors, Byr2 and Scd1, compete for GTP-loaded Ras1.G17V (1-172). *In vitro* GST pull-down assays of bacterially expressed Ras1.G17V (1-172) and GST-Byr2 (65-180) were conducted as in (A). Addition of Scd1 (760-872) fragment interfered with Ras1-Byr2 binding (the 4th lane). Quantitated signal intensities of the Ras1.G17V (1-172) band in the gel are shown in the right panel. (E) Simulated **pp**MAPK^{Spk1} dynamics in the wildtype model at increasing concentrations of Ras1-GTP added *in silico* to the system. Increased Ras1-GTP concentration causes advanced and reduced **pp**MAPK^{Spk1} peak intensities. (F) The model fitted to the 4 strains (as above, in red) correctly predicts **pp**MAPK^{Spk1} dynamics in the additional 21 signalling mutant strains (in light and dark green) measured in this study.

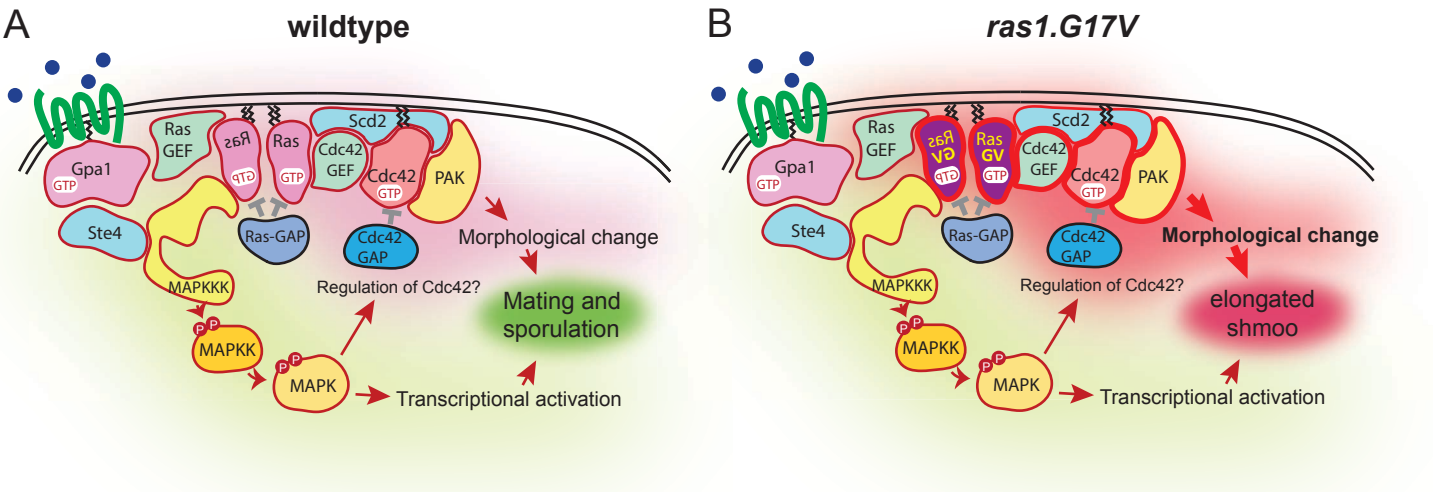

Fig. 8. Schematic diagram of the fission yeast pheromone signalling pathway
(A) Wildtype fission yeast pheromone signalling pathway, highlighting the branched pheromone sensing, and that both branches are necessary for mating. (B) Because of the robust regulatory mechanism implemented for the MAPK pathway and the competition between the effectors, the constitutively active *ras1.G17V* mutation yields a biased overactivation of Cdc42.

Fig. S1

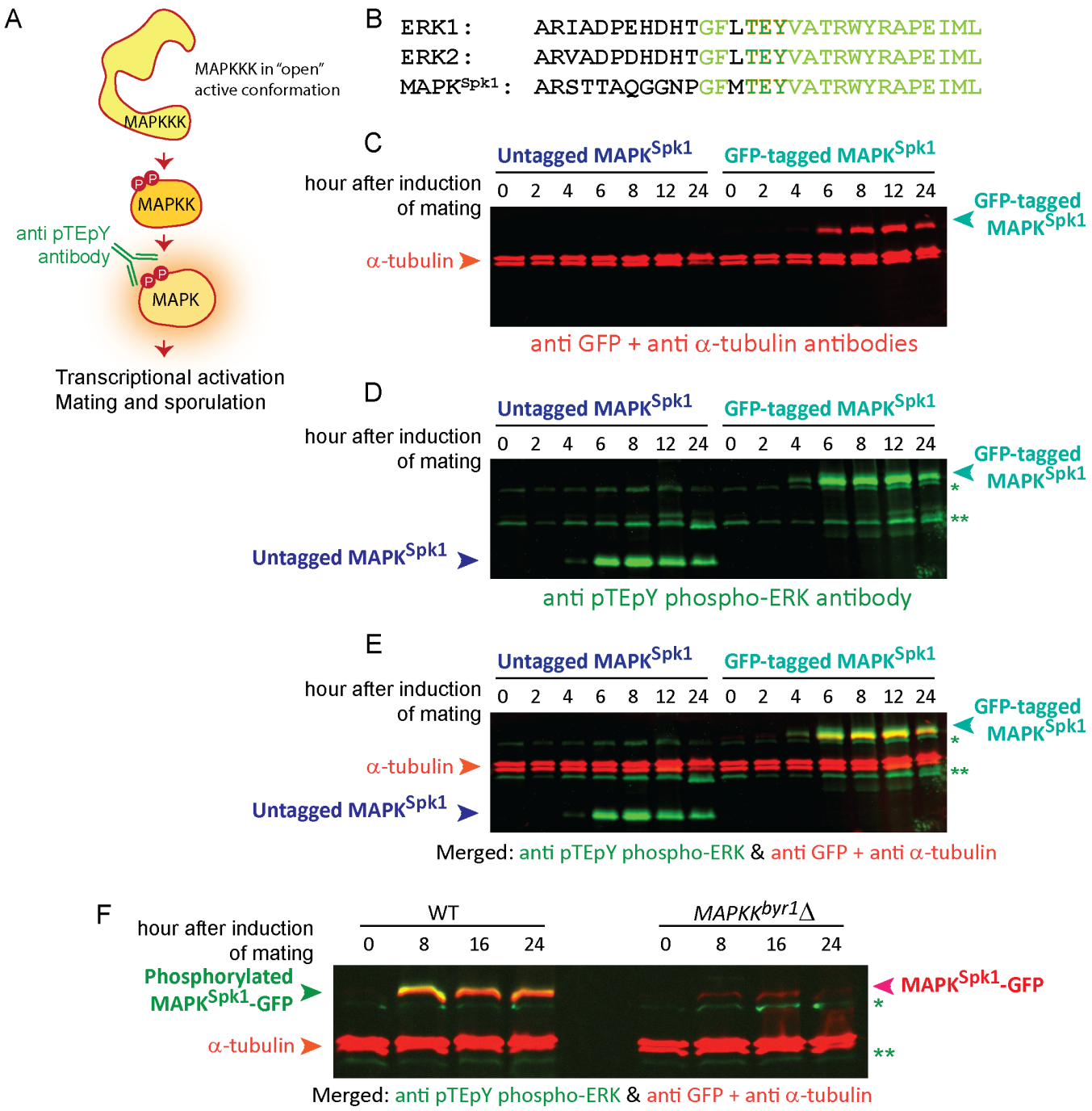

Supplementary Figure S1. Validation of the use of a commercially available anti-GFP and anti- phospho-MAPK specific antibody. (A) Schematic outlining of the principal of a phospho-specific MAPK antibody, which specifically recognize the phosphorylated TEY motif (pTEpY) of MAPK. (B) Sequence alignment between mammalian ERK1, ERK2 and *S.pombe* MAPK^{Spk1} at the region of the dual phosphorylation required for activation and surrounding residues. Conserved residues are in light green and TEY is highlighted with orange-green. (C)-(E) A Western blot of a time-course of a WT (KT301) and a MAPK^{Spk1}-GFP strain (KT3082) over 24 hours, incubated with anti GFP, anti-pTEpY phospho-ERK and anti α-tubulin antibodies. Li-cor Odyssey system was used to detect the signals. (C) The signals obtained by the 700 nm wavelength scan to detect signals from a primary monoclonal mouse anti-GFP antibody ((0.4mg/ml), Roche Cat No 11814460001. Used at a 1:2000 dilution) and the primary anti α-tubulin antibody TAT1 (generous gift from Keith Gull, 1:3000), followed by the IRDye 680LT secondary antibody (goat anti-mouse antibody, Li-cor 926-32211(1.0 mg/ml), 1:16,000 dilution). α-tubulin was used as an internal loading control. (D)The exact same blot as in (C) but showing the 800 nm wavelength scan to detect signals from an anti pTEpY phospho-ERK antibody (#4370 Cell Signaling technology. Used at 1:2000 dilution) visualised by the IRDye 800CW goat anti-rabbit secondary antibody (Li-cor 926-68020 (1.0 mg/ml), 1:16000 dilution). The band indicated by a single asterisk (*) was concluded to be irrelevant to MAPK^{Spk1}-GFP because although this band runs very close to MAPK^{Spk1}-GFP, it does not exactly overlap with the MAPK^{Spk1}-GFP signal (in red) in (E) and (F). Furthermore, the band exists in non-tagged MAPK^{Spk1} strain seen in (D) and in *mapkk^{byr1}Δ* strains in (F), further supporting that the band is irrelevant to phospho-MAPK^{Spk1}-GFP. A double asterisk indicates a band which was also concluded not to be relevant to phospho-MAPK^{Spk1} because of the same reason. Considering the molecular weight, this double asterisk band may correspond to another MAPK, MAPK^{Pmk1}. (E) An overlay of the 700 and 800 nm channels presented in (C) and (D). (F) The phospho-ERK antibody is phospho-specific. Cell extracts were prepared from the time-course of MAPK^{Spk1}-GFP tagged WT (KT3082) and *mapkk^{byr1}Δ* strains (KT4300) and MAPK^{Spk1}-GFP was detected by anti-GFP (red) while phospho-MAPK^{Spk1} was detected by anti-pTEpY phosphor ERK antibody (green). In the *mapkk^{byr1}Δ* strain, phosphorylated MAPK^{Spk1}-GFP signal is missing although MAPK^{Spk1}-GFP was detectable at 8, 16 and 24 hours after induction of mating. The same background bands seen in (D) and (E) are indicated in the same way using a single (*) and double (**) asterisk.

Fig. S2

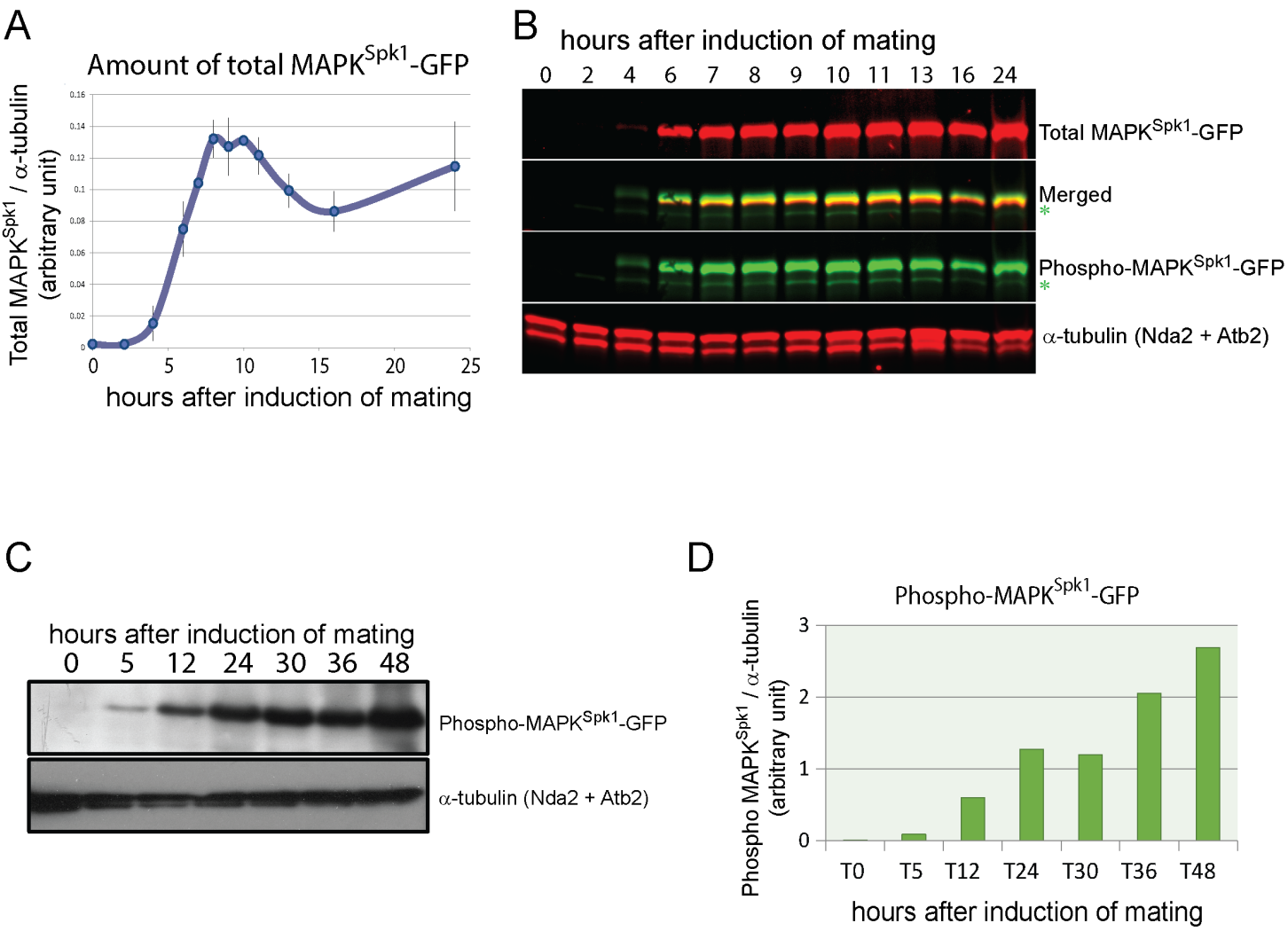

Supplementary Figure S2.

(A) and (B): Quantitation of total MAPK^{Spk1}-GFP during the mating process.

The total MAPK^{Spk1}-GFP protein level was detected using the anti-GFP antibody ((0.4mg/ml), Roche Cat No 11814460001. Used at a 1:2000 dilution). MAPK^{Spk1}-GFP Cells (KT3082) were induced for sexual differentiation by the plate mating assay system as described in the materials and methods. (A) Three biological replicates were used for quantitation to obtain the mean value (error bars are ±SEM). α-tubulin was used as a loading control and quantitation was carried out using the Image Studio ver2.1 software (Licor Odyssey CLx Scanner). (B) A typical example of Western blotting used for quantitation is shown. The green asterisk indicates the background band recognized by anti-phospho-ERK antibody (#4370 Cell Signaling technology. Used at 1:2000 dilution) as seen in the supplementary Figure S1.

(C) and (D): *MAPKK$^{byr1.DD}$* mutation causes constitutive activation of MAPK^{Spk1}.

Cells carrying *MAPKK$^{byr1.DD}$* mutation (KT3435) were induced for sexual differentiation by the plate mating assay system as described in the Materials and Methods. Western blotting of phospho-MAPK^{Spk1} and α-tubulin was conducted using ECL system (GE healthcare). (A) The results were visualized by exposing the signals to a X-ray film. (B) The bands were scanned and quantitated using ImageJ software (https://imagej.nih.gov/ij/). The α -tubulin signals were used as an internal control to estimate relative **pp**MAPK^{Spk1} levels.

A

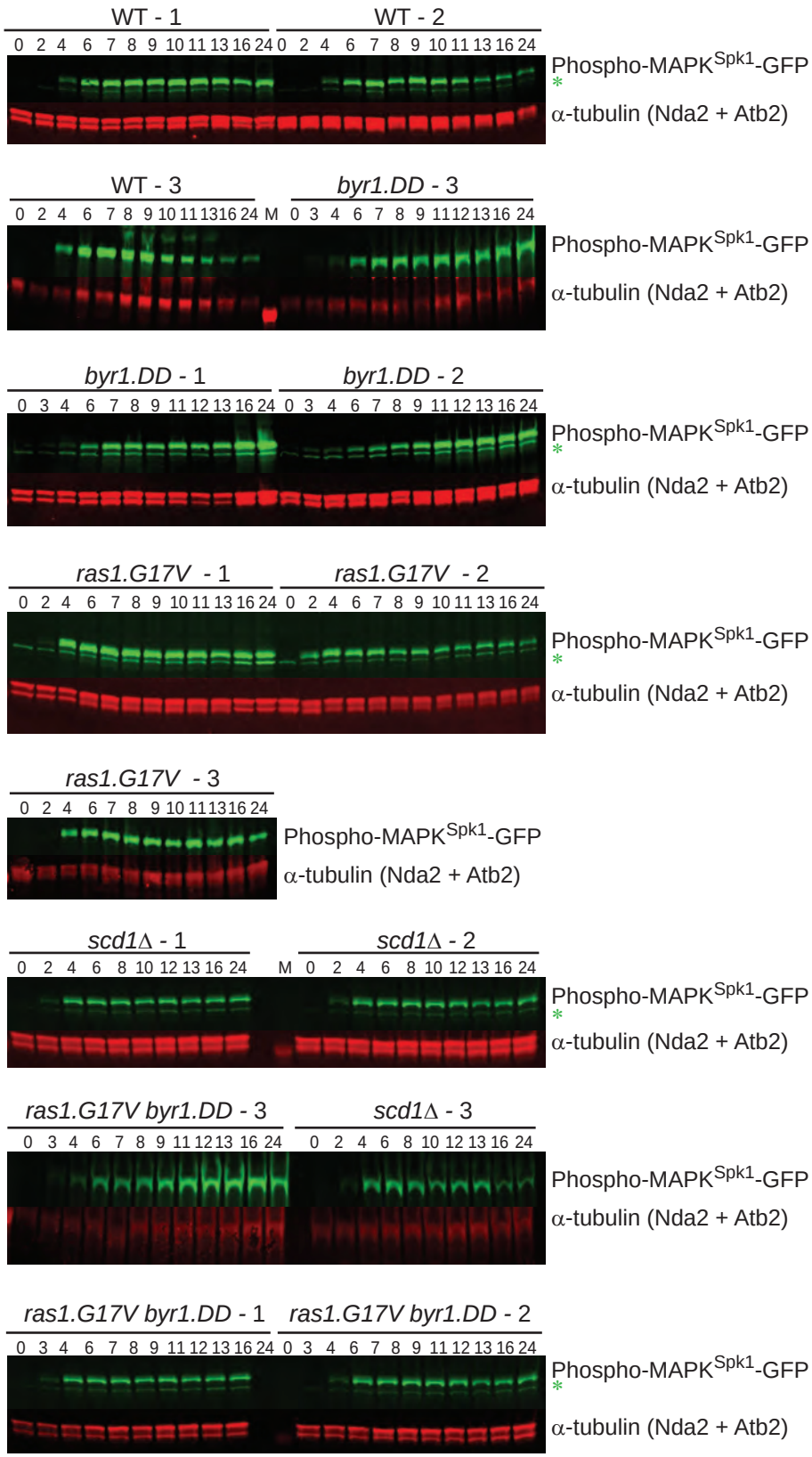

B

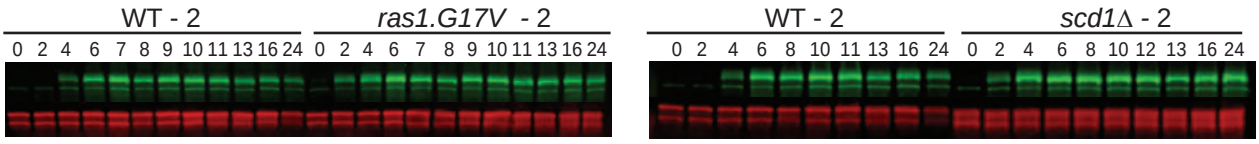

Supplementary Figure S3. Original Western blotting images of WT, *ras1.G17V*, *byr1.DD*, *ras1.GV byr1.DD* and *scd1*Δ mutants used to quantitate ppMAPK^{Spk1}-GFP during the mating process in Fig. 1, 2 and 3.
MAPK^{Spk1}-GFP Cells were induced for sexual differentiation by the plate mating assay system as described in the materials and methods. (A) Three biological replicates presented were used for quantitation to obtain the mean value and SEM. α-tubulin was used as a loading control and quantitation was carried out using the Image Studio ver2.1 software (Licor Odyssey CLx Scanner). ppMAPK^{Spk1}-GFP was detected by anti-phospho-ERK antibody (#4370 Cell Signaling technology. Used at 1:2000 dilution). The green asterisk indicates the background band as seen in the supplementary Figure S1. Numbers indicate hours after induction of mating. (B) Extracts of WT -2 and *ras1.G17V* -2 (left panel) and WT-2 and *scd1*Δ -2 (right panel) were re-run as technical replicates. These membranes were used to estimate relative intensities of ppMAPK^{Spk1}-GFP between WT, *scd1*Δ and *ras1.G17V* strains.

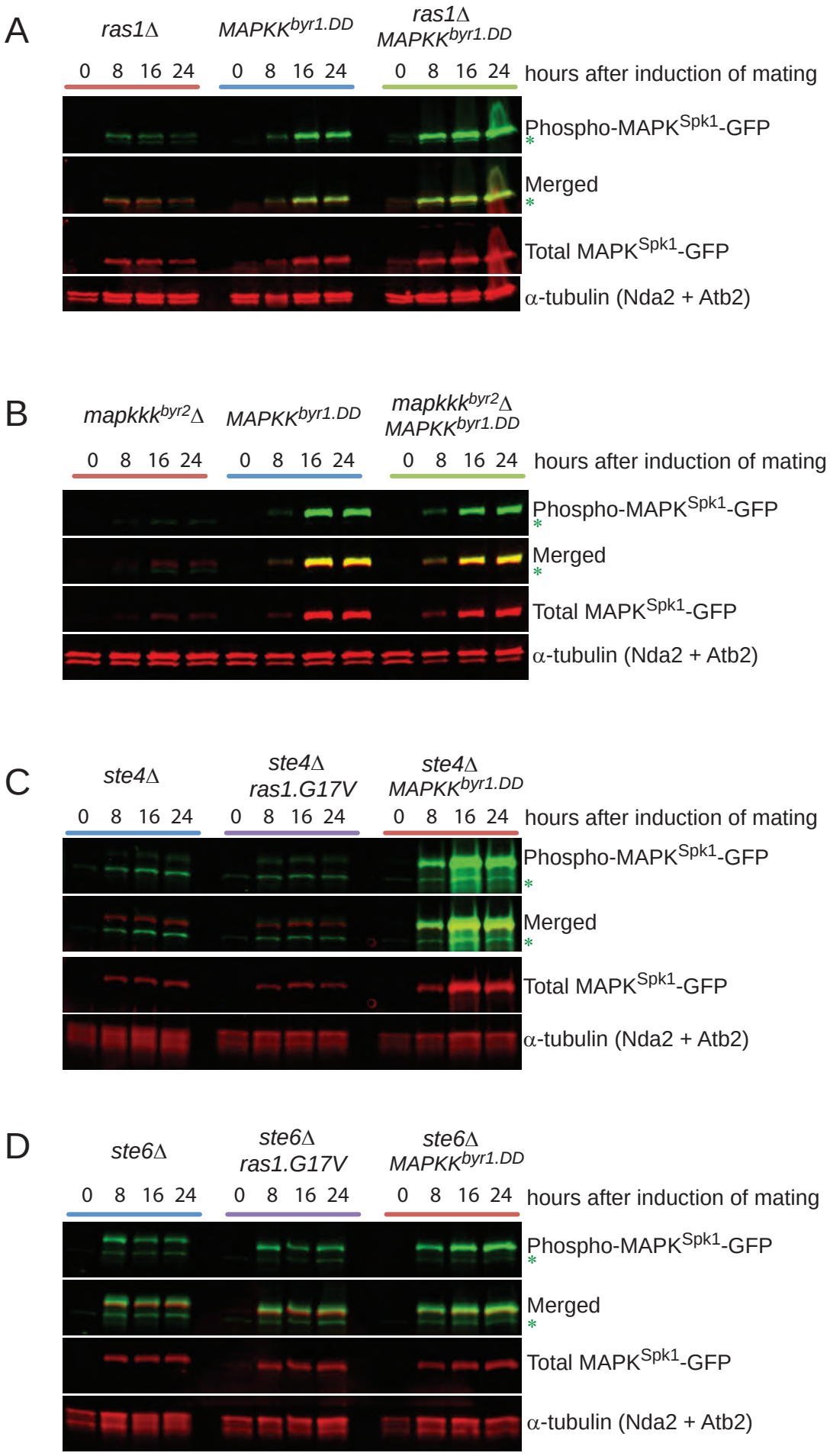

Supplementary Figure S4. Oribinal Western blotting membranes used in Fig. 3 and 5.
(A) Original Western blotting membrane used to quantitate phospho-MAPK^{Spk1}-GFP to generate the graph presented in Figure 3 (D). Strains used were; *ras1Δ* (KT4323), *MAPKK$^{byr1.DD}$* (KT3435) and *ras1Δ MAPKK$^{byr1.DD}$* (KT4359) (B) Original Western blotting membrane used to quantitate phospho-MAPK^{Spk1}-GFP to generate the graph presented in Figure 3 (E).

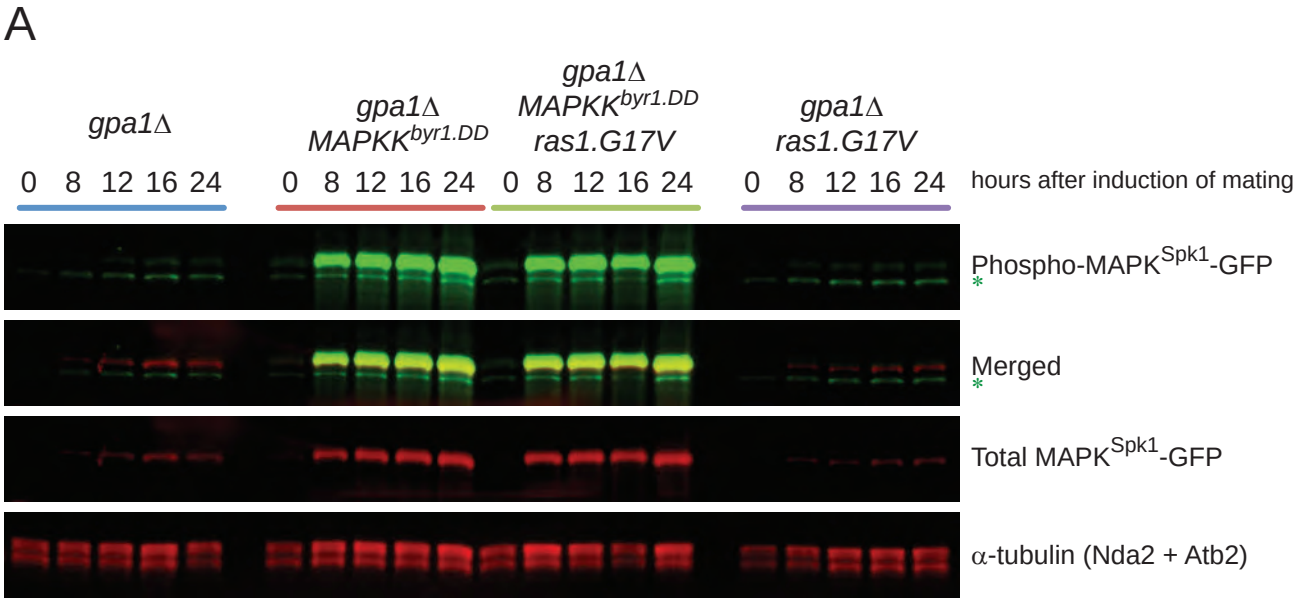

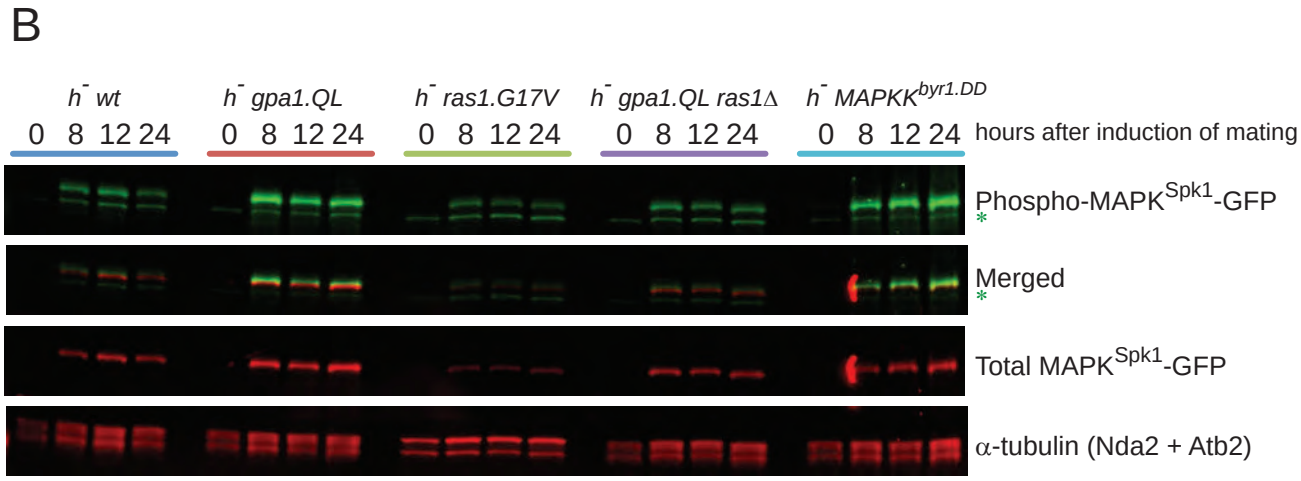

Supplementary Figure S5. Original Western blotting membranes used in Fig. 6.
(A) Original Western blotting membranes used to quantitate phospho-MAPK^{Spk1}-GFP to generate the graph in Figure 6 (A) Strains used were; *gpa1Δ* (KT4335), *gpa1Δ ras1.G17V* (KT5023), *gpa1Δ MAPKK$^{byr1.DD}$* (KT4353) and *gpa1Δ ras1.val17 MAPKK$^{byr1.DD}$*.(KT5035). (B) Original Western blotting membrane used to quantitate phospho-MAPK^{Spk1}-GFP to generate the graph in Figure 6 (C). Strains used were; *h⁻* WT (KT4190), *h⁻ gpa1.QL* (KT5059), *h⁻ ras1.G17V* (KT4233), *h⁻ gpa1.QL ras1Δ* (KT5070), *h⁻ MAPKK$^{byr1.DD}$* (KT4194). The green asterisk indicates a background band recognized by anti-phospho-ERK antibody (#4370 Cell Signaling technology. Used at 1:2000 dilution). α-tubulin was used as a loading control and quantitation was carried out using the Image Studio ver2.1 software (Licor Odyssey CLx Scanner).

Fig. S6

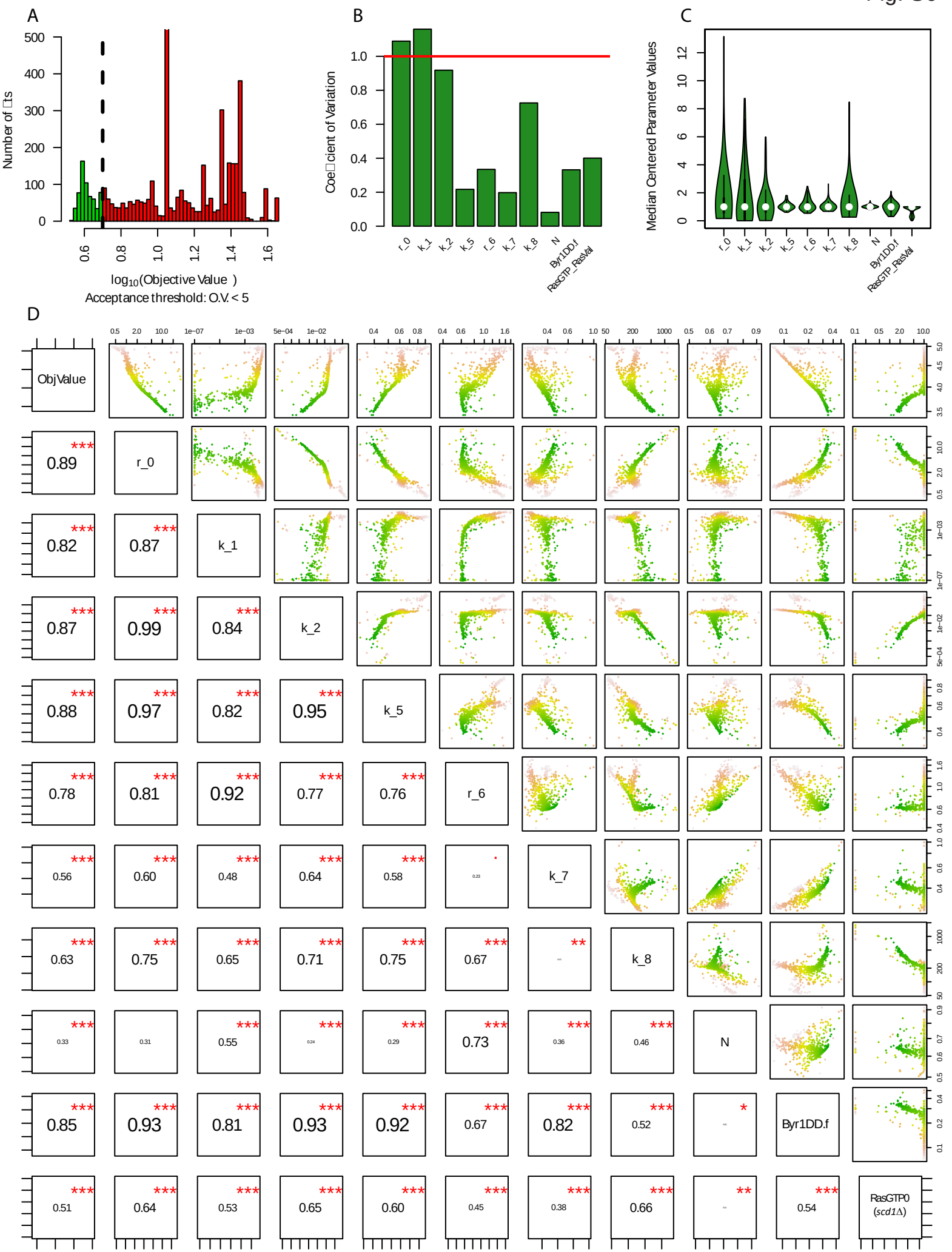

Supplementary Figure S6. Parameter distributions and relationships in multiplexed global parameter fitting.

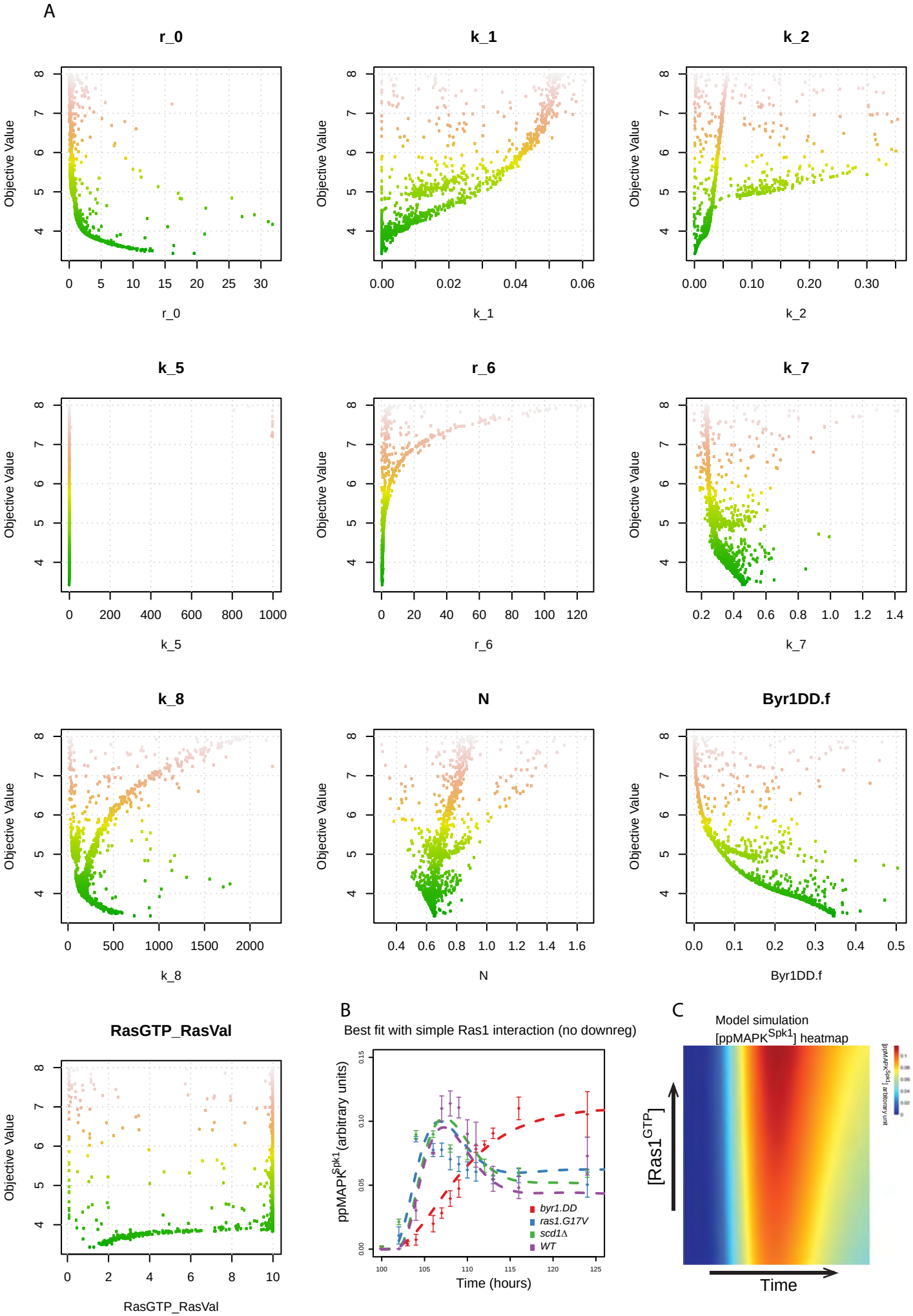

Supplementary Figure S7. Convergence of parameters in linear scale, over an extended range

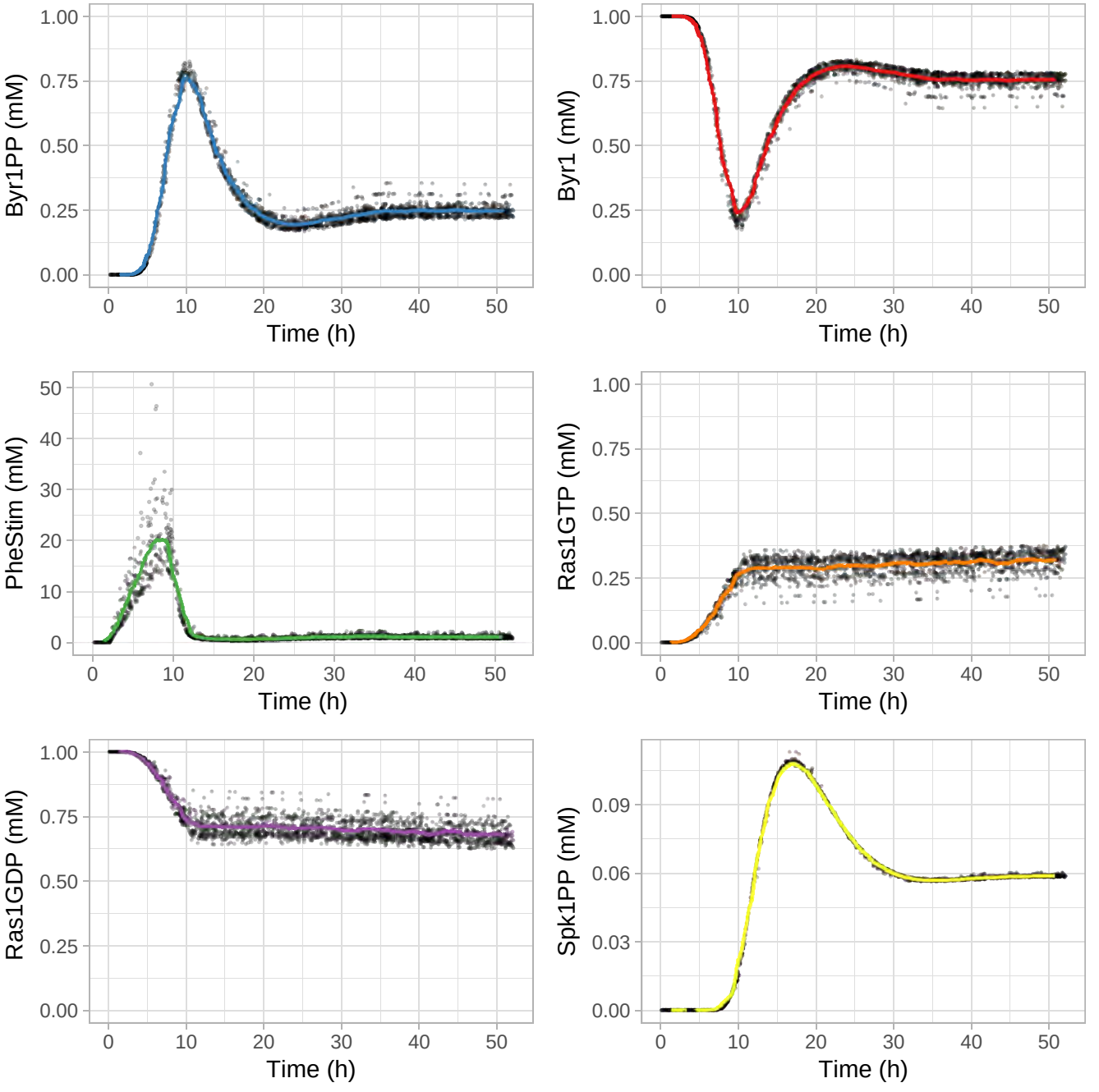

Supplementary Figure S8. Ensemble modeling shows that the dynamics of protein concentration are robustly predicted regardless of certain parameters' unidentifiability.
Time course simulation of the 100 best-fitted wild type models for all 6 variables. Rolling averages (window of 100) are displayed in color, and ten thousand randomly sampled simulation points (in grey) for each experiment show a narrow distribution of predicted concentration dynamics.

Supplementary Information

Supplementary Figures

Supplementary Figure S1. Validation of the use of a commercially available anti-GFP and anti- phospho-MAPK specific antibody.

(A) Schematic outlining of the principal of a phospho-specific MAPK antibody, which specifically recognize the phosphorylated TEY motif (pTEpY) of MAPK. (B) Sequence alignment between mammalian ERK1, ERK2 and *S.pombe* $MAPK^{Spk1}$ at the region of the dual phosphorylation required for activation and surrounding residues. Conserved residues are in light green and TEY is highlighted with orange-green. (C)-(E) A Western blot of a time-course of a WT (KT301) and a $MAPK^{Spk1}$-GFP strain (KT3082) over 24 hours, incubated with anti GFP, anti-pTEpY phospho-ERK and anti α-tubulin antibodies. Li-cor Odyssey system was used to detect the signals. (C) The signals obtained by the 700 nm wavelength scan to detect signals from a primary monoclonal mouse anti-GFP antibody ((0.4mg/ml), Roche Cat No 11814460001. Used at a 1:2000 dilution) and the primary anti α-tubulin antibody TAT1 (generous gift from Keith Gull, 1:3000), followed by the IRDye 680LT secondary antibody (goat anti-mouse antibody, Li-cor 926-32211(1.0 mg/ml), 1:16,000 dilution). α-tubulin was used as an internal loading control. (D)The exact same blot as in (C) but showing the 800 nm wavelength scan to detect signals from an anti pTEpY phospho-ERK antibody (#4370 Cell Signaling technology. Used at 1:2000 dilution) visualised by the IRDye 800CW goat anti-rabbit secondary antibody (Li-cor 926-68020 (1.0 mg/ml), 1:16000 dilution). The band indicated by a single asterisk (*) was concluded to be irrelevant to $MAPK^{Spk1}$-GFP because although this band runs very close to $MAPK^{Spk1}$-GFP, it does not exactly overlap with the $MAPK^{Spk1}$-GFP signal (in red) in (E) and (F). Furthermore, the band exists in non-tagged $MAPK^{Spk1}$ strain seen in (D) and in *mapkk*^{byr1}*Δ* strains in (F), further supporting that the band is irrelevant to phospho-$MAPK^{Spk1}$-GFP. A double asterisk indicates a band which was also concluded not to be relevant to phospho-$MAPK^{Spk1}$ because of the same reason. Considering the molecular weight, this double asterisk band may correspond to another MAPK, $MAPK^{Pmk1}$. (E) An overlay of the 700 and 800 nm channels presented in (C) and (D). (F) The phospho-ERK antibody is phospho-specific. Cell extracts were prepared from the time-course of $MAPK^{Spk1}$-GFP tagged WT (KT3082) and *mapkk*^{byr1}*Δ* strains (KT4300) and $MAPK^{Spk1}$-

31 GFP was detected by anti-GFP (red) while phospho-MAPK^{Spk1} was detected by anti-pTEpY
32 phosphor ERK antibody (green). In the *mapkk^{byr1}Δ* strain, phosphorylated MAPK^{Spk1}-GFP
33 signal is missing although MAPK^{Spk1}-GFP was detectable at 8, 16 and 24 hours after
34 induction of mating. The same background bands seen in (D) and (E) are indicated in the
35 same way using a single (*) and double (**) asterisk.

36

37 **Supplementary Figure S2.**

38 **(A) and (B): Quantitation of total MAPK^{Spk1}-GFP during the mating process.**

39 The total MAPK^{Spk1}-GFP protein level was detected using the anti-GFP antibody ((0.4mg/ml),
40 Roche Cat No 11814460001. Used at a 1:2000 dilution). MAPK^{Spk1}-GFP Cells (KT3082) were
41 induced for sexual differentiation by the plate mating assay system as described in the
42 materials and methods. (A) Three biological replicates were used for quantitation to obtain
43 the mean value (error bars are ±SEM). α-tubulin was used as a loading control and
44 quantitation was carried out using the Image Studio ver2.1 software (Licor Odyssey CLx
45 Scanner). (B) A typical example of Western blotting used for quantitation is shown. The
46 green asterisk indicates the background band recognized by anti-phospho-ERK antibody
47 (#4370 Cell Signaling technology. Used at 1:2000 dilution) as seen in the supplementary
48 Figure S1.

49 **(C) and (D): *MAPKK$^{byr1.DD}$* mutation causes constitutive activation of MAPK^{Spk1}.**

50 Cells carrying *MAPKK$^{byr1.DD}$* mutation (KT3435) were induced for sexual differentiation by the
51 plate mating assay system as described in the Materials and Methods. Western blotting of
52 phospho-MAPK^{Spk1} and α-tubulin was conducted using ECL system (GE healthcare). (A) The
53 results were visualized by exposing the signals to a X-ray film. (B) The bands were scanned
54 and quantitated using ImageJ software (https://imagej.nih.gov/ij/). The α -tubulin signals
55 were used as an internal control to estimate relative ppMAPK^{Spk1} levels.

56

57 **Supplementary Figure S3.**

58 **Original Western blotting images of WT, *ras1.G17V*, *byr1.DD*, *ras1.GV byr1.DD* and *scd1Δ***
59 **mutants used to quantitate ppMAPK^{Spk1}-GFP during the mating process in Fig. 1, 2 and 3.**

60 MAPK^{Spk1}-GFP Cells were induced for sexual differentiation by the plate mating assay system
61 as described in the materials and methods. (A) Three biological replicates presented were
62 used for quantitation to obtain the mean value and SEM. α-tubulin was used as a loading
63 control and quantitation was carried out using the Image Studio ver2.1 software (Licor
64 Odyssey CLx Scanner). **pp**MAPK^{Spk1}-GFP was detected by anti-phospho-ERK antibody (#4370
65 Cell Signaling technology. Used at 1:2000 dilution). The green asterisk indicates the
66 background band as seen in the supplementary Figure S1. Numbers indicate hours after
67 induction of mating. M: Marker lane. (B) Extracts of WT -2 and *ras1.G17V* -2 (left panel) and
68 WT-2 and *scd1Δ* -2 (right panel) were re-run as technical replicates. These membranes were
69 used to estimate relative **pp**MAPK^{Spk1} intensities between WT, *scd1Δ* and *ras1.G17V* strains.

70

71 **Supplementary Figure S4. Original Western blotting membranes used in Fig. 3 and 5.**

72 (A) Original Western blotting membrane used to quantitate phospho-MAPK^{Spk1}-GFP to
73 generate the graph presented in Figure 3 (D). Strains used were; *ras1Δ* (KT4323),
74 *MAPKK$^{byr1.DD}$* (KT3435) and *ras1Δ MAPKK$^{byr1.DD}$* (KT4359) (B) Original Western blotting
75 membrane used to quantitate phospho-MAPK^{Spk1}-GFP to generate the graph presented in
76 Figure 3 (E). Strains used were; in *mapkkk^{byr2}Δ* (KT3763), *MAPKK$^{byr1.DD}$* (KT3435) and
77 *mapkkk^{byr2}Δ MAPKK$^{byr1.DD}$* (KT4010). (C) Original Western blotting membrane used to
78 quantitate phospho-MAPK^{Spk1}-GFP to generate the graph in Figure 5 (A). Strains used were;
79 *ste4Δ* (KT4376), *ste4Δ ras1.G17V* (KT5143) and *ste4Δ MAPKK$^{byr1.DD}$* (KT5136). (D) Original
80 Western blotting membrane used to quantitate phospho-MAPK^{Spk1}-GFP to generate the
81 graph in Figure 5 (C). Strains used were; *ste6Δ* (KT4333), *ste6Δ ras1.G17V* (KT4998) and
82 *ste6Δ MAPKK$^{byr1.DD}$* (KT5139). Indicated mutant cells were induced for mating by the plate
83 mating assay system as described in the Materials and Methods. Western blotting of
84 phospho-MAPK^{Spk1} and α-tubulin was conducted in the same way as Supplementary Figure
85 S1. The green asterisks indicate the same background band recognized by anti-phospho-ERK
86 antibody (#4370 Cell Signaling technology. Used at 1:2000 dilution) seen in the
87 Supplementary Figure S1 and do not overlap with the red signals that represent the "Total
88 MAPK^{Spk1}-GFP" in the "Merged" panel. α-tubulin was used as a loading control and
89 quantitation was carried out using the Image Studio ver2.1 software (Licor Odyssey CLx
90 Scanner).

91

92 **Supplementary Figure S5. Original Western blotting membranes used in Fig. 6.**

93 (A) Original Western blotting membranes used to quantitate phospho-MAPK^{Spk1}-GFP to
94 generate the graph in Figure 6 (A) Strains used were; *gpa1Δ* (KT4335), *gpa1Δ ras1.G17V*
95 (KT5023), *gpa1Δ MAPKK$^{byr1.DD}$* (KT4353) and *gpa1Δ ras1.val17 MAPKK$^{byr1.DD}$*.(KT5035). (B)
96 Original Western blotting membrane used to quantitate phospho-MAPK^{Spk1}-GFP to generate
97 the graph in Figure 6. (C) Strains used were; *h$^-$* WT (KT4190), *h$^-$ gpa1.QL* (KT5059), *h$^-$*
98 *ras1.G17V* (KT4233), *h$^-$ gpa1.QL ras1Δ* (KT5070), h$^-$ *MAPKK$^{byr1.DD}$* (KT4194). The green
99 asterisk indicates a background band recognized by anti-phospho-ERK antibody (#4370 Cell
100 Signaling technology. Used at 1:2000 dilution). α-tubulin was used as a loading control and
101 quantitation was carried out using the Image Studio ver2.1 software (Licor Odyssey CLx
102 Scanner).

103

104 **Supplementary Figure S6. Parameter distributions and relationships in multiplexed global**
105 **parameter fitting**

106 (A) Distribution of objective values after 5000 parallel parameter estimations by the global
107 optimization algorithm "particle swarm" with randomized starting values within +- 4
108 magnitudes around the previously achieved best fit. Fits with an objective value < 5 are
109 accepted for further analysis (green). Simulations with +- 5 magnitudes resulted in the same
110 best fits, but much smaller convergence (See Materials and Methods).

111 (B-C) Coefficient of variation and distribution of parameters within the 578 the accepted fits
112 show unimodal distributions for all parameters, and most of them are narrowly distributed,
113 suggesting a unique optimum. In (C), the only bimodal distribution is that of RasGTP0
114 (Scd1Δ) among fits below O.V.<5. In (D, top right corner) however it is shown that this
115 parameter also converges to a single optima, below O.V. of 3.

116 (D) Pairwise scatterplots and Spearman correlation coefficients among all parameters and
117 the objective value (log scale axes). In this figure, every dot is an independently fitted model
118 (obj. value <5); and every panel shows a pairwise correlation between a fitted parameter
119 and the objective value (top row), or between two fitted parameters (other rows). Green to

120 brown denotes the objective values between 3.4 and 5. The top row shows that with better
121 fits, all parameters (but k_1) converge to a single optimum (bottom most points, in green).

122

123 **Supplementary Figure S7. Convergence of parameters in linear scale, over an extended**
124 **range**

125 (A) Alternative representation of the top row of Fig.S6D. Parameter values are displayed on
126 a linear scale (X-axis) and fits below and objective value (O.V.) of 8 (instead of below 5) are
127 displayed.

128 (B) Simulated time course of $MAPK^{Spk1}$ in the best fit of a simplified model variant shows no
129 advanced peaking in the *ras1.G17V* and *scd1Δ* mutant strains. This model is simplified from
130 the original model (Fig.7 A) by removing [L10], and models the scenario where Ras has no
131 complex interactions, it has only activating roles [L5, L9].

132 (C) Simulated $ppMAPK^{Spk1}$ dynamics in the simplified model (B) at increasing concentrations
133 of $Ras1^{GTP}$ added *in silico* to the system. Increased $Ras1^{GTP}$ concentration causes advanced
134 and reduced **pp**$MAPK^{Spk1}$ peak intensities.

135

136 **Supplementary Figure S8. Ensemble modeling shows that the dynamics of protein**
137 **concentration are robustly predicted regardless of certain parameters' unidentifiability.**

138 Time course simulation of the 100 best-fitted wild type models for all 6 variables. Rolling
139 averages (window of 100) are displayed in color, and ten thousand randomly sampled
140 simulation points (in grey) for each experiment show a narrow distribution of predicted
141 concentration dynamics.

142

Supplementary Table S1 : Strains used in this study

Figure 1

C, D

KT3082 *h^{90} ade6.M216 leu1.32 spk1-GFP-2xFLAG::Kan^R*

E, F

KT3435 *h^{90} ade6-M216 leu1.32 byr1.DD::Hyg^R spk1-GFP-2xFLAG::Kan^R*

G, H

KT3084 *h^{90} ade6.M210 leu1.32 ras1.G17V::$LEU2^+$ spk1-GFP-2xFLAG::Kan^R*

Figure 2

A, B

KT3439 *h^{90} ade6.M210 leu1.32 ras1.G17V::$LEU2^+$ byr1.DD::Hyg^R spk1-GFP-2xFLAG::Kan^R*

C

KT4300 *h^{90} ade6.M216 leu1.32 byr1::$ClonNAT^R$ spk1-GFP-2xFLAG::Kan^R*

KT5215 *h^{90} ade6.M210 leu1.32 ras1.G17V::$LEU2^+$ byr1::$ClonNAT^R$ spk1-GFP-2xFLAG::Kan^R*

Figure 3

A

KT3082 *h^{90} ade6.M216 leu1.32 spk1-GFP-2xFLAG::Kan^R*

KT4061 *h^{90} ade6.M216 leu1.32 scd1::$ClonNAT^R$ spk1-GFP-2xFLAG::Kan^R*

KT4056 *h^{90} ade6.M210 leu1.32 ras1.G17V::$LEU2^+$ scd1::$ClonNAT^R$ spk1-GFP-2xFLAG::Kan^R*

B

KT3082 *h^{90} ade6.M216 leu1.32 spk1-GFP-2xFLAG::Kan^R*

KT4061 *h^{90} ade6.M216 leu1.32 scd1::$ClonNAT^R$ spk1-GFP-2xFLAG::Kan^R*

C

KT4047 *h^{90} ade6.M216 leu1.32 byr1.DD::Hyg^R scd1::$ClonNAT^R$ spk1-GFP-2xFLAG::Kan^R*

D

KT4323 *h^{90} ade6.M216 leu1.32 ras1::$ClonNAT^R$ spk1-GFP-2xFLAG::Kan^R*

KT3435 *h^{90} ade6-M216 leu1.32 byr1.DD::Hyg^R spk1-GFP-2xFLAG::Kan^R*

KT4359 *h^{90} ade6.M216 leu1.32 byr1.DD::Hyg^R ras1::$ClonNAT^R$ spk1-GFP-2xFLAG::Kan^R*

E

KT3763 *h^{90} ade6.M216 leu1.32 byr2::$ClonNAT^R$ spk1-GFP-2xFLAG::Kan^R*

KT3435 *h^{90} ade6-M216 leu1.32 byr1.DD::Hyg^R spk1-GFP-2xFLAG::Kan^R*

KT4010 *h^{90} ade6-M216 leu1.32 byr1.DD::Hyg^R byr2::$ClonNAT^R$ spk1-GFP-2xFLAG::Kan^R*

F

KT4323 *h^{90} ade6.M216 leu1.32 ras1::ClonNAT^R spk1-GFP-2xFLAG::Kan^R*

KT4359 *h^{90} ade6.M216 leu1.32 byr1.DD::Hyg^R ras1::ClonNAT^R spk1-GFP-2xFLAG::Kan^R*

KT3763 *h^{90} ade6.M216 leu1.32 byr2::ClonNAT^R spk1-GFP-2xFLAG::Kan^R*

KT4010 *h^{90} ade6-M216 leu1.32 byr1.DD::Hyg^R byr2::ClonNAT^R spk1-GFP-2xFLAG::Kan^R*

Fig. 4

A, B

KT5077 *h^{90} ade6.M210 leu1.32 ura4.294::[Pshk1:ScGIC2 CRIB:GFP3:ura4$^+$]*

KT5082 *h^{90} ade6.M216 leu1.32 ras1.G17V::LEU2$^+$ ura4.294::[Pshk1:ScGIC2 CRIB:GFP3:ura4$^+$]*

C, D

KT5107 *h^{90} ade6.M210 leu1.32 ras1::ClonNAT^R ura4.294::[Pshk1:ScGIC2 CRIB:GFP3:ura4$^+$]*

KT5077 *h^{90} ade6.M210 leu1.32 ura4.294::[Pshk1:ScGIC2 CRIB:GFP3:ura4$^+$]*

KT5082 *h^{90} ade6.M216 leu1.32 ras1.G17V::LEU2$^+$ ura4.294::[Pshk1:ScGIC2 CRIB:GFP3:ura4$^+$]*

KT5551 *h^{90} ade6.M210 leu1.32 rga4::Hyg^R ura4.294::[Pshk1:ScGIC2 CRIB:GFP3:ura4$^+$]*

KT5554 *h^{90} ade6.M216 leu1.32 ras1.G17V::LEU2$^+$ rga4::Hyg^R ura4.294::[Pshk1:ScGIC2 CRIB:GFP3:ura4$^+$]*

Fig. 5

A, B

KT4376 *h^{90} ade6.M216 leu1.32 ste4::ClonNAT^R spk1-GFP-2xFLAG::Kan^R*

KT5143 *h^{90} ade6.M210 leu1.32 ste4::ClonNAT^R ras1.G17V::LEU2$^+$ spk1-GFP-2xFLAG::Kan^R*

KT5136 *h^{90} ade6-M216 leu1.32 ste4::ClonNAT^R byr1.DD::Hyg^R spk1-GFP-2xFLAG::Kan^R*

C, D

KT4333 *h^{90} ade6.M216 leu1.32 ste6::ClonNAT^R spk1-GFP-2xFLAG::Kan^R*

KT4998 *h^{90} ade6.M210 leu1.32 ste6::Hyg^R ras1.G17V::LEU2$^+$ spk1-GFP-2xFLAG::Kan^R*

KT5139 *h^{90} ade6-M216 leu1.32 ste6::ClonNAT^R byr1.DD::Hyg^R spk1-GFP-2xFLAG::Kan^R*

Fig. 6

A, B

KT4335 *h^{90} ade6.M216 leu1.32 gpa1::ClonNAT^R spk1-GFP-2xFLAG::Kan^R*

KT5023 *h^{90} ade6.M210 leu1.32 gpa1::ClonNAT^R ras1.G17V::LEU2$^+$ spk1-GFP-2xFLAG::Kan^R*

KT4353 *h^{90} ade6-M216 leu1.32 gpa1::ClonNAT^R byr1.DD::Hyg^R spk1-GFP-2xFLAG::Kan^R*

KT5035 *h^{90} ade6.M210 leu1.32 gpa1::ClonNAT^R ras1.G17V::LEU2$^+$ byr1.DD::Hyg^R spk1-GFP-2xFLAG::Kan^R*

C, D

KT4190 *h^- ade6.M216 leu1.32 spk1-GFP-2xFLAG::Kan^R*

KT5059 *h^- ade6.M216 leu1.32 ura4.d18 gpa1.QL::ura4$^+$ spk1-GFP-2xFLAG::Kan^R*

KT4233 *h^- ade6.M216 leu1.32 ras1.G17V::LEU2$^+$ spk1-GFP-2xFLAG::Kan^R*

KT5070 *h^- ade6.M216 leu1.32 ura4.d18 ras1::ClonNAT^R gpa1.QL::ura4$^+$ spk1-GFP-2xFLAG::Kan^R*

KT4194 *h^- ade6.M216 leu1.32 byr1.DD::Hyg^R spk1-GFP-2xFLAG::Kan^R*

Supplementary Figure S1

C, D and E

KT301 *h^{90} ade6-M216 leu1.32*

KT3082 *h^{90} ade6.M216 leu1.32 spk1-GFP-2xFLAG::Kan^R*

F

KT3082 *h^{90} ade6.M216 leu1.32 spk1-GFP-2xFLAG::Kan^R*

KT4300 *h^{90} ade6.M216 leu1.32 byr1::ClonNAT^R spk1-GFP-2xFLAG::Kan^R*

Supplementary Figure S2

A and B

KT3082 *h^{90} ade6.M216 leu1.32 spk1-GFP-2xFLAG::Kan^R*

C and D

KT3435 *h^{90} ade6-M216 leu1.32 byr1.DD::Hyg^R spk1-GFP-2xFLAG::Kan^R*

Supplementary Figure S3

KT3082 *h^{90} ade6.M216 leu1.32 spk1-GFP-2xFLAG::Kan^R*

KT3435 *h^{90} ade6-M216 leu1.32 byr1.DD::Hyg^R spk1-GFP-2xFLAG::Kan^R*

KT3084 *h^{90} ade6.M210 leu1.32 ras1.G17V::LEU2$^+$ spk1-GFP-2xFLAG::Kan^R*

KT3439 *h^{90} ade6.M210 leu1.32 ras1.G17V::LEU2$^+$ byr1.DD::Hyg^R spk1-GFP-2xFLAG::Kan^R*

KT4061 *h^{90} ade6.M216 leu1.32 scd1::ClonNAT^R spk1-GFP-2xFLAG::Kan^R*

Supplementary Figure S4

A

KT4323 *h^{90} ade6.M216 leu1.32 ras1::ClonNAT^R spk1-GFP-2xFLAG::Kan^R*

KT3435 *h^{90} ade6-M216 leu1.32 byr1.DD::Hyg^R spk1-GFP-2xFLAG::Kan^R*

KT4359 *h^{90} ade6.M216 leu1.32 byr1.DD::Hyg^R ras1::ClonNAT^R spk1-GFP-2xFLAG::Kan^R*

B

KT3763 *h^{90} ade6.M216 leu1.32 byr2::ClonNAT^R spk1-GFP-2xFLAG::Kan^R*

KT3435 *h^{90} ade6-M216 leu1.32 byr1.DD::Hyg^R spk1-GFP-2xFLAG::Kan^R*

KT4010 *h^{90} ade6-M216 leu1.32 byr1.DD::Hyg^R byr2::ClonNAT^R spk1-GFP-2xFLAG::Kan^R*

C

KT4376 *h^{90} ade6.M216 leu1.32 ste4::ClonNAT^R spk1-GFP-2xFLAG::Kan^R*

KT5143 *h^{90} ade6.M210 leu1.32 ste4::ClonNAT^R ras1.G17V::LEU2$^+$ spk1-GFP-2xFLAG::Kan^R*

KT5136 *h^{90} ade6-M216 leu1.32 ste4::ClonNAT^R byr1.DD::Hyg^R spk1-GFP-2xFLAG::Kan^R*

D

KT4333 *h^{90} ade6.M216 leu1.32 ste6::ClonNAT^R spk1-GFP-2xFLAG::Kan^R*

KT4998 *h^{90} ade6.M210 leu1.32 ste6::Hyg^R ras1.G17V::LEU2$^+$ spk1-GFP-2xFLAG::Kan^R*

KT5139 *h^{90} ade6-M216 leu1.32 ste6::ClonNAT^R byr1.DD::Hyg^R spk1-GFP-2xFLAG::Kan^R*

Supplementary Figure S5

A

KT4335 *h^{90} ade6.M216 leu1.32 gpa1::ClonNAT^R spk1-GFP-2xFLAG::Kan^R*

KT5023 *h^{90} ade6.M210 leu1.32 gpa1::ClonNAT^R ras1.G17V::LEU2$^+$ spk1-GFP-2xFLAG::Kan^R*

KT4353 *h^{90} ade6-M216 leu1.32 gpa1::ClonNAT^R byr1.DD::Hyg^R spk1-GFP-2xFLAG::Kan^R*

KT5035 *h^{90} ade6.M210 leu1.32 gpa1::ClonNAT^R ras1.G17V::LEU2$^+$ byr1.DD::Hyg^R spk1-GFP-2xFLAG::Kan^R*

B

KT4190 *h^- ade6.M216 leu1.32 spk1-GFP-2xFLAG::Kan^R*

KT5059 *h^- ade6.M216 leu1.32 ura4.d18 gpa1.QL::ura4$^+$ spk1-GFP-2xFLAG::Kan^R*

KT4233 *h^- ade6.M216 leu1.32 ras1.G17V::LEU2$^+$ spk1-GFP-2xFLAG::Kan^R*

KT5070 *h^- ade6.M216 leu1.32 ura4.d18 ras1::ClonNAT^R gpa1.QL::ura4$^+$ spk1-GFP-2xFLAG::Kan^R*

KT4194 *h^- ade6.M216 leu1.32 byr1.DD::Hyg^R spk1-GFP-2xFLAG::Kan^R*